Doctor thesis

Structural and functional analysis of the filament and bushing of flagellar motor

生体超分子べん毛モーターの繊維および軸受の機能・構造解析

Tomoko Yamaguchi

March 2022

Graduate School of Frontier Biosciences

Osaka University

Table of Contents

Abstract

The bacterial flagellum is a motility organelle for bacteria to swim in liquid environments. The flagellum is composed of the basal body as a rotary motor, the filament as a helical propeller and the hook as a universal joint connecting them. It consists of about 30 different proteins, and these component proteins self-assemble in a highly regulated manner. The motor converts the electrochemical potential difference of cations across the cell membrane to mechanical work with almost 100% efficiency. The rotational speed of the flagellar motor is as high as 1,700 revolution per second, which is much faster than that of the Formula One racing car engine.

Salmonella enterica serovar Typhimurium (here after *Salmonella*) is a pathogenic bacterium and has two distinct flagellar filament component proteins (flagellin), FliC and FljB. FliC and FljB are antigenically different, and this is thought to help *Salmonella* to escape from host immune systems. Even though both flagellins contribute to bacterial motility and infection, FljB was less studied, and its structure remained unrevealed. To clarify structural and functional differences between FliC and FljB, I carried out structural and functional analyses. *Salmonella* cells producing only the FljB filament showed higher motility than those producing only the FliC filament under highly viscose conditions. To examine the reason of this functional difference, the FljB filament structure was analyzed at 3.6 Å resolution by electron cryomicroscopy single particle image analysis and was compared with the FliC filament. These two structures were nearly identical but the position and orientation of the outermost domain D3 of flagellin were distinctly different. Domain D3 of FljB was much flexible and mobile than that of FliC, suggesting that it plays an important role in optimizing the motility function in viscous environments as well as changing the antigenicity.

The LP ring complex is a part of the flagellar basal body and acts as a bushing of the motor. It is very stable against various chemical treatment such as acid and urea, and supports high speed rotation of the flagellar motor. The rod is a drive shaft that transmits the rotational force to the hook and filament. The LP ring spans the outer membrane (by the L ring) and the peptidoglycan (PG) layer (by the P ring) and surrounds the rod to support its rapid and stable rotation without much friction. Because the surface

of the rod is highly negatively charged, it has been thought that the inner surface of the LP ring is negatively charged to produce electric repulsive force to minimize the frictional force between the rod and the LP ring. However, this raises another question of how the LP ring assembles around the rod against the repulsive force. To clarify how the LP ring assembles around the rod and acts as a bushing to support its high-speed rotation, the LP ring structure within the basal body and the P ring structure around the polyrod were analyzed by electron cryomicroscopy single particle image analysis at 3.5 Å and 2.5 Å resolution. The LP ring structure showed 26-fold rotational symmetry, and the L ring showed intricate intersubunit interactions of each subunit with up to six partners that explains the structural stability. The inner surface of the LP ring is charged both positively and negatively, and positive charges on the P ring and flexible residues of FlgI and FlgG presumably play important roles in the initial assembly process of the P ring around the rod. Therefore, the LP ring structure is optimized for both self-assembly and bushing function.

General introduction

Salmonella (Figure 1) infection is one of the four major causes of disease involving diarrheas in the world. It has a wide range of hosts, such as mouse, humans and even plants[1]. The infection occurs mainly via oral intake, and flagellar motility plays an important role in infection. A bacterial flagellum is a motility organelle responsible for rapid movement of bacterial cells towards more desirable environments. It enables bacteria to move through viscous environments such as mucosa, search for the host cell surface, and adhere to the cell membrane for infection[2,3].

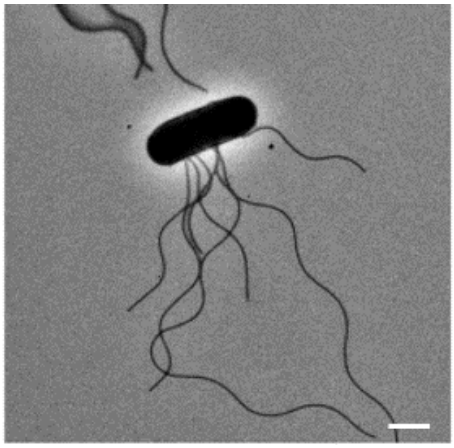

Figure 1 Negative stained *Salmonella enterica* serovar Typhimurium. The picture was taken by 100 kV transmission electron microscopy (TEM). The scale bar is 1 μm. One cell has six to eight flagellar filaments.

The flagellum is mainly composed of three parts: the basal body, which works as a rotary motor; the filament, which functions as a screw propeller; and the hook as a universal joint connecting the filament to the motor[4] (Figure 2). The flagellar motor converts the electrochemical potential difference of cations across the cell membrane to mechanical work required for high-speed rotation with almost 100% efficiency[4], and the maximum rotation speed has been measured to be 1,700 revolutions per second (rps) (Ref.[5]), which is much faster than that of the Formula One racing car engine. The motor is powerful enough to rotate the filaments that is 10 times as long as the cell length. The motor can rotate both clockwise (CW) and counterclockwise (CCW) without changing the direction of ion flow, and the switching frequency of rotational direction is controlled by the chemotactic signal transduction networks. When all motors rotate in the CCW direction, all the flagellar filaments together form a flagellar bundle behind the cell body to push the cell forward. When one or more motors changes their direction of rotation to the CW direction, the flagellar bundle is disrupted, and so the cell tumbles and change the swimming direction[6].

More than 60 genes are involved in the flagellum-driven motility and chemotaxis. There are two *mot* gens, six *che* gens and about same number of its receptor genes, and 40 *fla* genes encoding structural subunit proteins, transcriptional regulatory proteins, export apparatus proteins and scaffolding proteins for flagellar assembly[7]. Those genes' names are derived from their null phenotypes; Fla^- (divided into three loci, *flg*, *flh* or *fli*) mutants make incomplete flagellar structure; Mot^- mutants make completed flagella but do not rotate; Che^- mutants make complete flagellar structure and able to rotate but show inadequate chemotaxis.

The basal body consists of the C ring, MS ring, LP ring and rod (Figure 2). The MS-C ring acts as the rotor of the flagellar motor. The MS ring is composed of a transmembrane protein, FliF, and is the core of the rotor and the initial template for flagellar assembly. The C ring consists of three cytoplasmic proteins, FliG, FliM, and FliN, is attached to the cytoplasmic face of the MS ring, and is essential for torque generation and switching regulation of the motor. The stator proteins, MotA and MotB, form a proton (H^+) channel in the cytoplasmic membrane to couple H^+ influx through the

channel to torque generation. The cytoplasmic domain of MotA interacts with FliG located on top of the C ring to generate motor torque while the periplasmic domain of MotB binds to the PG layer via its PG binding motif for the stator unit to be anchored[8]. The rod is a rigid and straight cylindrical structure directly connected with the MS ring and acts as a drive shaft that transmits the motor torque to the filament[9,10]. The rod is divided into two structural parts: the proximal rod composed of FliE, FlgB, FlgC and FlgF; and the distal rod formed by FlgG. The hook composed of FlgE is a highly-curved, flexible structure that connects the distal rod and filaments. The filament composed of FliC or FljB (more detail in later) acts as a screw of the flagellar motor. The LP ring is a bushing supporting the distal rod for its rapid and stable rotation without much friction and is composed of a lipoprotein, FlgH, and a periplasmic protein, FlgI. The L and P rings are embedded within the outer membrane and the PG layer, respectively[11,12].

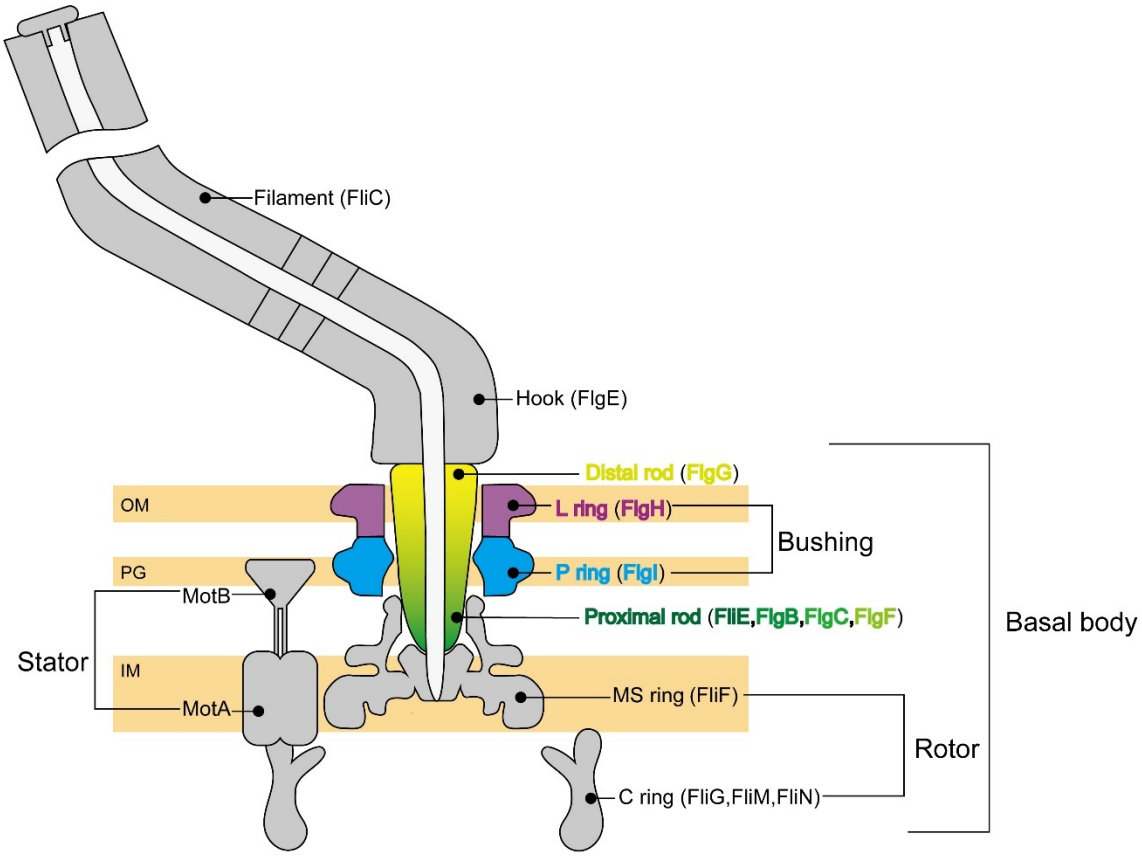

Figure 2 Schematic diagram of *Salmonella* flagellum. The figure shows the central slice of the flagellum mostly in gray with only the rod and LP ring colored to highlight them. Component proteins forming each structural unit are written in brackets. The MS ring and C ring work as a rotor. The MotA/B complex acts as a stator, converting the energy of H^+ influx into motor rotation. The distal (yellow) and proximal (green) rod works a drive shaft transmitting motor torque to the hook and filament. The L ring (purple) and P ring (cyan) together act as a bushing and support the high-speed rotation of the flagellar motor. OM, PG, and IM are the outer membrane, the PG layer and the inter membrane, respectively.

Chapter A

Structural and functional differences between the FljB and FliC flagellar filaments

Introduction

Polymorphic form of the flagellar filament

Salmonella has several peritrichous flagella, and the length of the filament is 10 to 15 μm long. The helical arrays of subunits making up the filament are traced as four different helical lines of 1-, 5-, 6-, and 11-start. Each start number represents the number of helical strands, and the next subunit along the n-start helical line corresponds to the n-th subunit from the one at the origin (subunit 0) along the 1-start helical line. The 11-start helices are called protofilaments[13]. One filament is composed of 11 protofilaments, and each protofilament is in either of the L (left-handed) and R (right-handed) state. The filament can form 12 different supercoils depending on the ratio of the protofilaments in the L and R states, and this is called polymorphism[14] (Figure 3). When the cell swims forward, the motors rotate CCW, and the normally left-handed supercoiled filaments form a bundle behind the cell to produce thrust. When the motors switch their rotation to the CW direction, the filaments change its form to a right-handed supercoil and cause the bundle to fall apart so that the cell can tumble and change the swimming direction[6] (Figure 4). If all the protofilaments are either of the L and R states, the filament becomes straight, and they are called either L-type or R-type straight filament.

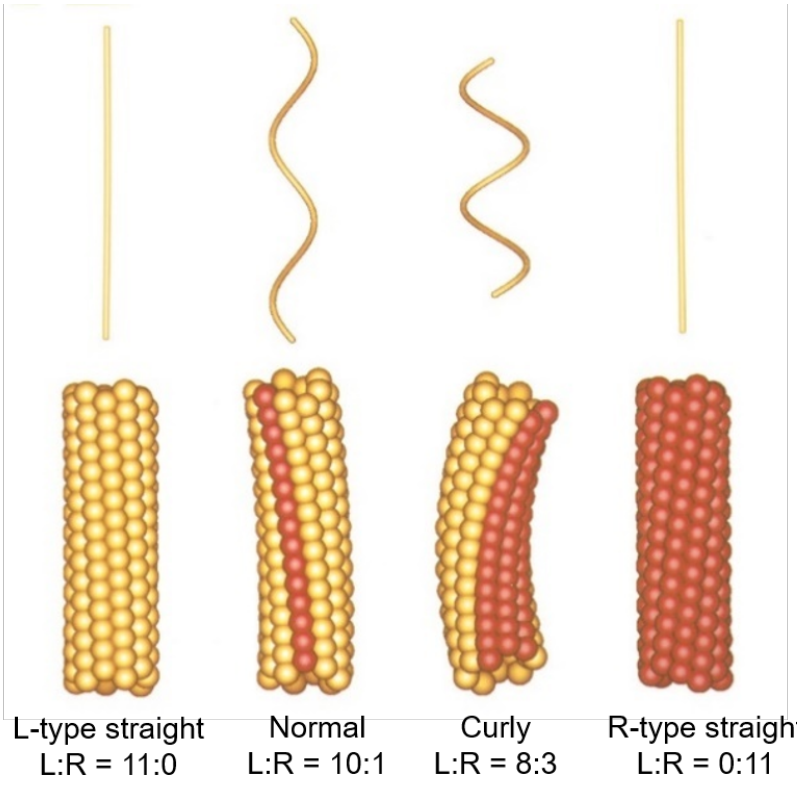

Figure 3 Model of polymorphic form of the flagellar filament. The upper and lower panel shows the filament shape and the arrangement of the subunit packing. The two distinct states are colored yellow (L state) or orange (R state). The ratio of the L and R state is displayed under the lower panel (modified from Namba *et al*., 2001, Fig. 3)

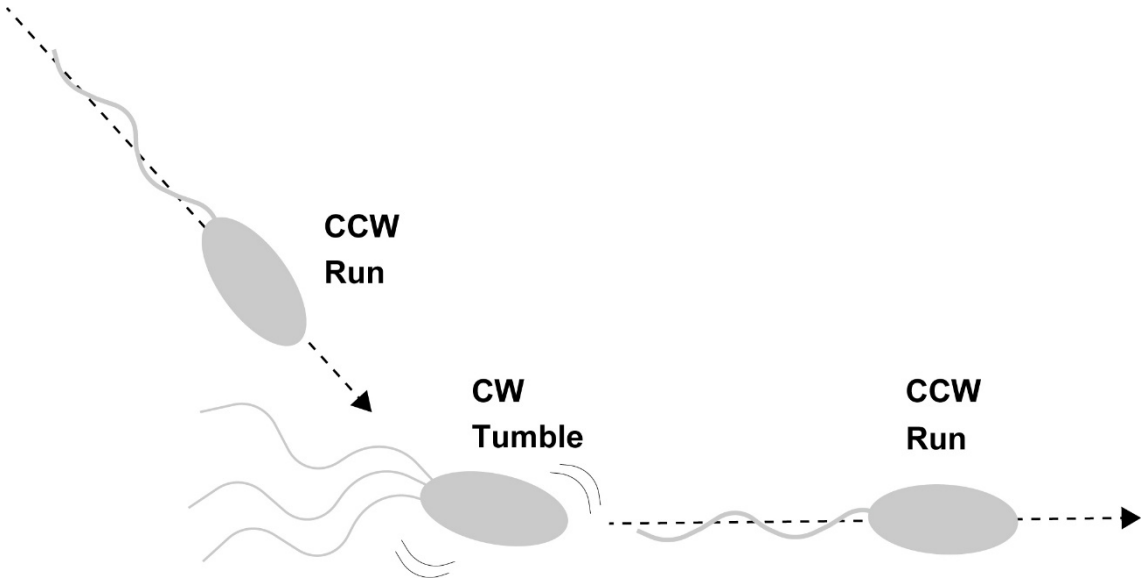

Figure 4 Swimming and tumbling of the bacterium with peritrichous flagella. When the bacterium is in a "run" state, the motors rotate counterclockwise (CCW) and the filaments form a bundle behind a cell body. When the bacterium is in a "tumble" state, the motors rotate clockwise (CW) and the bundle are fall apart so that the bacterium can change the swimming direction. The bacteria reach their desire point by combining those two states.

Phase variation of the flagellar filament

The proteins make up the filament are called flagellin. *Salmonella* has two antigenically different flagellin genes, *fljB* and *fliC*, and their expression are autonomously regulated to produce either FljB or FliC for filament formation at a frequency of 10^{-3} to 10^{-5} per cell per generation[15]. This is called phase variation[16], and it is thought to be a mechanism that enable the cell to escape from the host immune systems by changing flagellar antigenicity.

Usually, only one type of flagellin is expressed in one cell (Figure 5a). The 996 bp DNA fragment called H-segment, which is a *fljBA* promotor that depends on σ28 factor, controls whether *fliC* or *fljB* to express[17–20]. The H segment is flanked by inverted repetitious sequences, *hixL* and *hixR*, and the Hin recombinase namely Fis and HU mediate site-specific recombination at those sites, leading the inversion of H segment containing the *fljBA* promotor. When the H-segment is "ON", both *fljB* and *fljA* are transcribed, and the expression of *fliC* is suppressed by FljA. When the H segment is "OFF" by its inversion, the *fljBA* genes are no longer transcribed and FliC synthesis starts[18,20–23] (Figure 5b).

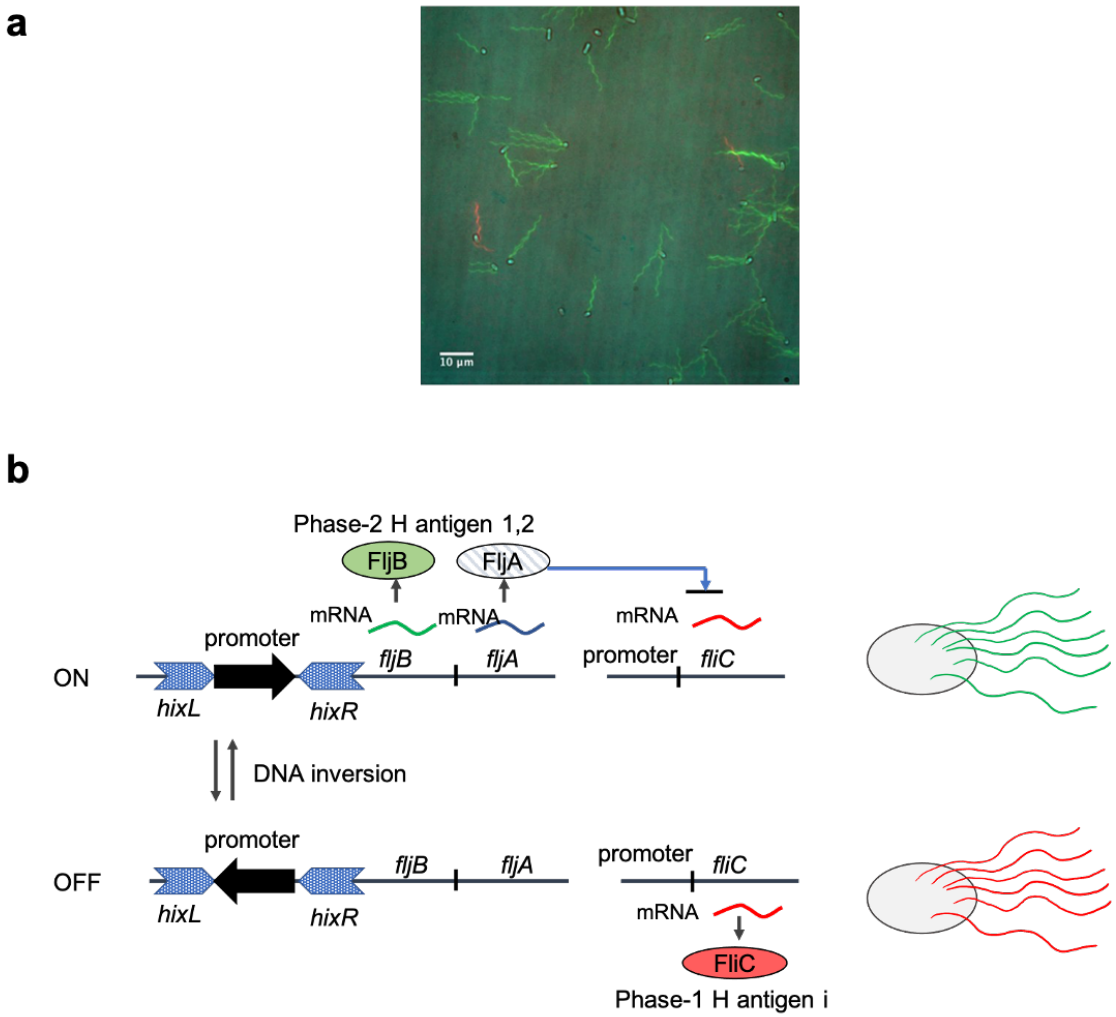

Figure 5 Phase variation of *Salmonella* flagellum. a, Immunofluorescent staining image of LT2 (wild type) strain of *Salmonella*. This strain has both *fljB* and *fliC* genes on the genome. The FljB and FliC flagellar filaments were stained and showed with green and red, respectably. The cells were cultured in 5 mL of LB at 37°C overnight with shaking. **b,** The H segment containing the *fljBA* promotor (bold black arrow) is flanked by inverted repetitious sequences, *hixL* (blue arrow left to the promoter) and *hixR* (blue arrow right to the promoter). The upper panel shows an "ON" state of the H segment, that allows both *fljB* and *fljA* to be transcribed, and the expression of *fliC* is suppressed by FljA. The lower panel shows a "OFF" state of the H segment by its inversion, prohibits the *fljBA* genes to be transcribed and allows FliC synthesis.

Functional difference between the FljB and FliC filaments

It has been reported that the FliC-expressing cells display a significant advantage for invasion of most epithelial cell lines of murine and human origin compared to the FljB-expressing cells. The FliC-expressing cells show a higher invasion rate to the MODE-K murine epithetical cells[24] and a stronger growth rate in blood, spleen, small intestine, cecum, colon, and mesenteric lymph nodes of mouse than the FljB-expressing cell[25,26]. Ikeda *et al.*[25] have explained that the FliC-expressing cells have the advantage of growing and/or surviving after reaching the mice spleens but not so much in the intestinal stage of infection. Differences in the swimming behaviors near the surfaces of the epithelial cells have also been observed, and the FliC-expressing cells more frequently "stop"[26]. It seems that the difference in virulence between FljB and FliC is not related to the swimming ability but somehow related to the ability of surviving inside the host cell, although the detail of the mechanism is still elusive. In order to understand the differences in their antigenicity and motility function, structural and functional characterizations are necessary. However, structural information was available only for the FliC filament[27–29].

Structure of the FliC filament

The three-dimensional (3D) structures of a FliC fragment lacking domain D0 and the FliC filament have been studied by X-ray crystallography and electron cryomicroscopy (cryoEM) helical image analysis, respectively[27–29] (Figure 6). *Salmonella* FliC from a wild-type strain, SJW1103, which is used for motility and chemotaxis studies, consists of 494 amino acid residues, and the molecular mass is about 50 kDa. This FliC molecule consists of four domains, D0, D1, D2, and D3, which are arranged from the inner core to the outer surface of the filament. Domains D0 and D1 form the inner core of the filament and are made of α-helical coiled coils. These domains play a critical role in forming the supercoiled structure of the filament as a helical propeller. In addition, a β-hairpin structure in domain D1 is considered to be important for switching the conformation of flagellin subunits between the two states L and R to produce various types of supercoiled filaments for swimming and tumbling[27–29]. Domains D2 and D3 are found in the outer part of the filament structure. These two domains increase the stability of the filament structure as well as the drag force of the filament as a propeller by increasing the

diameter[27,30]. The outermost domain, D3, is thought to contain epitopes for antibodies, determining the antigenicity of the flagella.

Purpose of this study

To understand the differences in the functions between the FljB and FliC filaments, structural information of the FljB filaments is necessary. Functional characterization of cell motility is also necessary to investigate the potentially different physiological roles played by these two types of filaments, if any. The present study is carried out to investigate the differences between the FljB and FliC filament structures and their motility functions.

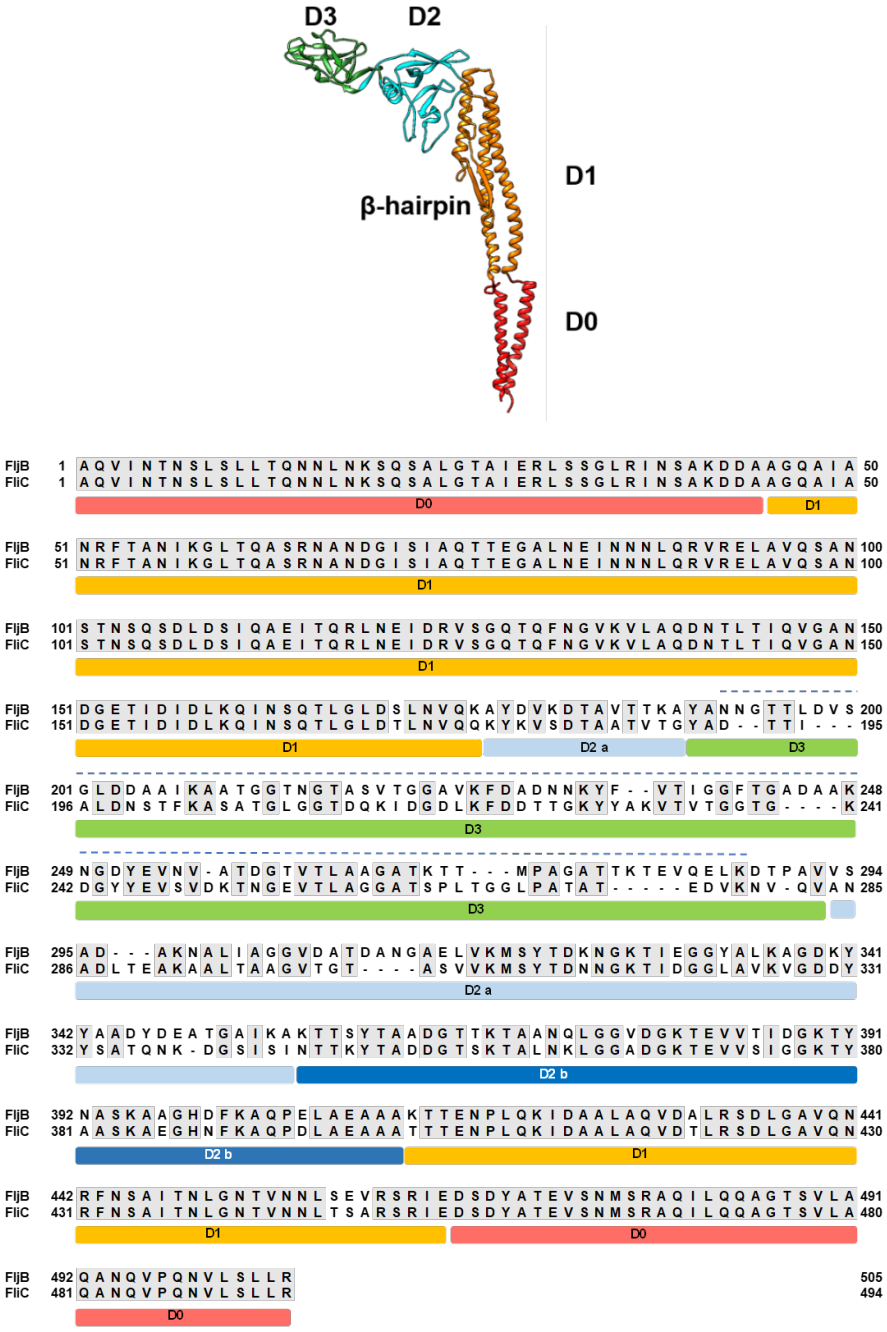

Figure 6 Atomic model of FliC and amino acid sequence alignment of FljB and FliC. The atomic model of FliC (PDB ID: 1UCU, upper panel) and sequence alignment of FliC and FljB (lower panel). The amino acid sequence of FljB and FliC shows 76% identity and 1.4×10^{-66} *E*-value. Conserved residues are shaded in gray in the lower panel. Each domain is indicated by labels in the atomic model or bars on top of the sequence alignment in different colors.

Materials and Methods

Salmonella strains, plasmids, and media

Bacterial strains of *Salmonella enterica* serovar Typhimurium and plasmids used in this study are listed in Table 1. For the filaments analyses, four strains were used: SJW1103, SJW1103ΔC, SJW1103B and SJW590. SJW1103 lacks the *fljB* operon so expresses only the FliC flagellin, while SJW1103B express only the FljB flagellin. SJW1103ΔC lacks weather *fliC* and *fljB* and show no flagella filament. For cryoEM structural analyses, the strain expressing the FljB flagellar filament of the R-type straight form (the right-handed helical symmetry) was used.

Luria–Bertani broth (LB) were used as a culture media containing 1% (w/v) tryptone, 0.5% (w/v) yeast extract, 0.5% (w/v) NaCl. The 0.75% (w/v) and 0.35% of Bacto agarose was added to LB for LB plates and soft agar plates, respectively. If needed, 100 μg/mL ampicillin was added to those media. The motility buffer was used for swimming assay containing 10 mM potassium phosphate pH 7.0, 0.1 mM EDTA, 10 mM sodium D-lactate.

Table 1 Strains and plasmids used in chapter A

***Salmonella* strains**	**Relevant Characteristics**	**Source or Reference**
SJW1103	FliC wild-type Δ*hin-fljB-fljA*	Ref.[31]
SJW1103ΔC	SJW1103 Δ*fliC*::*tetRA*	Ref.[32]
SJW1103B	FljB wild-type Δ*fliC*::*fljB*	
SJW590	FljB_R-type straight filament *fljB(A461V)*, Δ*fliC*	

DNA manipulation

In order to delete FliC gene from SJW1103 and replace it with *tetRA*, the λ Red homologous recombination system[33] was used. A pKD46 plasmid has ampicillin resistance, and it is a temperature-sensitive replicon so that removed from the cell at 42°C. The SJW1103 competent cells were mixed with 1 μL of pKD46 and transformed by using 0.1 cm cuvettes at 1.8 kV. 1 mL of LB was added to those cells, cultured at 30°C for one hour for recovery, and plated on LB plate with ampicillin at 30°C overnight. A single colony was cultured in 5 mL of LB with 0.2% arabinose and 50 μL ampicillin at 30°C until OD_{600} reached 0.5. The cells were washed three times and resuspended in 100 μL of Mili-Q water. For recombination of *fliC* with *tetRA* to make SJW1103*ΔfliC::tetRA*, purified PCR products of *tetRA* DNA were electroporated to the competent cells of SJW1103 carrying pKD46. Transformation was done as described above. 1 mL of LB was added to the cells, incubated at 37°C, and then plated on LB plate with tetracycline at 42ºC overnight to remove pKD46. Colonies were picked up and the constructs were confirmed by DNA sequencing. For recombination of *tetRA* with *fljB* for making SJW1103B (Δ*fliC*::*fljB*), PCR products of *fljB* DNA were electroporated to the cell of SJW1103*ΔfliC::tetRA* carrying pKD46. Transformation was done as described above, except that cells were plated on soft ager with arabinose and motile cells were selected[34,35].

Swimming assay

Salmonella strains were pre-cultured in 5 mL of LB overnight with shaking at 37°C. Bacterial growth was measured via optical density at 600 nm (OD_{600}). For swimming motility assay of SJW1103B (only expressing FljB) and SJW1103 (only expressing FliC), a 5 μL measure of the culture medium was inoculated into 5 mL of fresh LB, and it was incubated for 6 hours at 37°C with shaking. The cells were diluted in the motility buffer [10 mM potassium phosphate pH 7.0, 0.1 mM EDTA, 10 mM sodium D-lactate]. The viscosity of the motility buffer was adjusted by adding Ficoll PM400 (GE healthcare, Chicago, IL, USA) to a final concentration of 5%, 10%, or 15%. Swimming motility was observed using a bright-field microscope, CX-41 (Olympus, Tokyo, Japan) with a 40× objective (PlanC N 40× NA 0.65 Olympus) and a 1.25× variable magnification lens (U-CA 1.5 × Olympus) and recorded using a high-speed camera (GEV-B0620M-TC000 IMPREX, Boca Raton, FL, USA). The swimming speed was calculated using the software Move-tr2/2D (Library Co., Tokyo, Japan).

Fluorescence labeling of flagellin antibodies

IgG antibodies against FliC and FljB were purified from rabbit serum using a Melon™ Gel IgG Spin Purification Kit (Thermo Fisher Scientific, Waltham, MA, USA). The buffer was changed to a phosphate-buffered salt solution (pH 7.4) simultaneously with concentration of IgG by using a YM-50 Centriprep centrifugal filter (Merck, Darmstadt, Germany). After adjusting the concentration of IgG to 1 mg/mL, the antibodies were labelled with an Alexa Fluor™ 594 Antibody Labeling Kit (Thermo Fisher Scientific) for the FliC antibody and with an Alexa Fluor™ 488 Antibody Labeling Kit (Thermo Fisher Scientific) for the FljB antibody.

Measuring the number and length of flagellar filaments

Four measuring the number and the length of FljB and FliC filaments, SJW1103B and SJW1103 were pre-cultured in 5 mL of LB at 37°C overnight with shaking. Bacterial growth was measured via OD_{600}, and a 5 μL measure of the culture medium was inoculated into 5 mL of fresh LB, and it was incubated for 6 hours at 37°C with shaking. The culture was diluted 50 to 100 times with the motility buffer. To label the flagellar filaments, the cells were first attached to the surface of a slide glass coated with polylysine by filling the culture medium under a cover slip for 5 min. The culture medium was then replaced with a 20 μL solution of fluorescently labeled antibodies at 25 μg/mL, and it was left for 5 to 10 min. The excess antibody dye was washed by gently flowing 40 μL of the motility buffer twice, and the filaments were then observed by fluorescence microscopy. These observations were performed under an IX-83 optical microscope with a UPlan-SApo 100× 1.4 NA objective lens (Olympus). For each of the mutant strains, the number of filaments and their length per cell were counted for 50 cells manually. The number of the flagellar filaments per cell was measured using ImageJ (National Institutes of Health, Bethesda, MD, USA).

Statistical analysis

Statistical analyses were done using Excel 2016 (Microsoft). Comparisons between two datasets were performed using two-tailed Student's *t*-test. A P value of < 0.05 was considered to be statistically significant difference. Figures were drawn by Excel 2016 (Microsoft).

CryoEM sample purification

For FljB R-type straight flagellar filaments purification, SJW590 was pre-cultured in 30 mL LB with shaking overnight at 37°C, and 15 mL of the culture was then inoculated into 1 L of fresh LB. The cells were grown until the optical density had reached an OD_{600} of about 1.0. The culture was collected by centrifugation and resuspended in 10% sucrose buffer [10% (w/v) sucrose, 0.1 M Tris-HCl pH 8.0]. EDTA (pH adjusted by HCl to 7.8) and lysozyme were added to final concentrations of 10 mM and 0.1 mg/mL, respectively. The suspension was stirred on ice for 1 hour at 4°C, and 0.1 M $MgSO_4$ and 10% (w/v) Triton X-100 were then added to final concentrations of 10 mM and 1% (w/v), respectively. After stirring for 1 hour at 4°C, 6 mL of 0.1 M EDTA (pH adjusted by NaOH to 11.0) was added. The solution was centrifuged at 15,000 × *g*, and the supernatant was collected. The pH was adjusted to 10.9 with 5 N NaOH, and the sample solution was re-centrifuged at 15,000 × *g* to remove undissolved membrane fractions. The supernatant was centrifuged at 67,000 × *g* to collect the flagellar filament with the hook basal body attached (the filament) as a pellet. The sample was resuspended in 1 mL of Buffer C [10 mM Tris-HCl pH 7.8, 5 mM EDTA, 1% (w/v) Triton X-100] and was centrifuged at 7300 × *g*, and the supernatant was collected. The filament was purified by a sucrose density-gradient centrifugation method with a gradient of sucrose from 20% to 50%. The fraction containing the filament was collected and checked by SDS-PAGE. The fraction was 2-fold diluted by Buffer A [20 mM Tris-HCl pH 7.8, 150 mM NaCl, 1 mM $MgCl_2$], and the sucrose was removed by centrifugation of the filament at 104,300 × *g*. Finally, the filament was resuspended with 10–50 µL of Buffer A, and the sample solution was stored at 4°C.

Negative staining and EM observation

The condition and concentration of purified samples were checked before making cryoEM sample grid. A 5 µL aliquot of the flagellar filament sample in solution was mixed with 2% PTA on Palafilm (Bemis Flexible Packaging) and was placed on a thin carbon-coated, copper grid with 24 seconds glow-discharged. The extra solution was removed from the grid by blotting. The sample grids were dried for 1 hour at room temperature and checked using a transmission electron microscope, JEM-1011 (JEOL, Akishima, Japan) with an accelerating voltage of 100 kV.

Electron cryomicroscopy and image processing

A 3 µL aliquot of the sample solution was applied to a Quantifoil holey carbon grid R1.2/1.3 Mo 200 mesh (Quantifoil Micro Tools GmbH, Großlöbichau, Germany) with pretreatment by glow discharge (both side of grid). The grids were blotted and plunged into liquid ethane at the temperature of liquid nitrogen for rapid freezing[36] with Vitrobot Mark IV (Thermo Fisher Scientific) with a blotting time of 3 seconds at 4°C and 100% humidity (Table 2). Grids were then transferred into electron cryomicroscope with a cryostage cooled by liquid nitrogen.

The data collection of the FljB filament were operated on a Titan Krios electron cryomicroscope (Thermo Fisher Scientific) equipped with a field-emission electron gun operated at an accelerating voltage of 300 kV. Dose-fractionated movie images were recorded using a direct electron detector camera, Falcon Π (Thermo Fisher Scientific) and were automatically collected using EPU software (Thermo Fisher Scientific). Using a

minimum dose system, all movies were taken with a total exposure of 2 seconds, an electron dose of 10.3 electron/Å^2 per frame, a defocus range of 0.2 to 1.9 µm, and a nominal magnification of 75,000×, corresponding to an image pixel size of 1.06 Å. All seven frames of the movie image were recorded with a frame rate of 0.1 s/frame, and the middle five frames from the 2nd to the 6th were used for image analysis. The defocus range was estimated by Gctf[37] after motion correction by RELION-3.0-β2[38]. The filament images were segmented and extracted in square boxes of 400 pixels with 90% overlap by using RELION-3.0-β2. Finally, FljB filament with applying helical parameters (twist 65.8 degrees and rise 4.8 Å) was reconstructed at 3.6 Å resolution from about 1.1 million segment images obtained from 2,319 cryoEM movie images (Figure 7). The overall resolution was estimated by Fourier Shell Correlation (FSC) = 0.143 (Figure 7d). The summary of cryoEM data collection and statistics is shown in Table 3.

Model building

To build the atomic model of the FljB filament, a homology model was first generated from the atomic model of the FliC filament[28] (PDB ID: 1UCU, Figure 6) using MODELLER[39], then fitted into the 3D density map and refined using UCSF Chimera[40] and Coot[41]. For further refinement, the densities around 4 Å from the Cα atoms were extracted from the density map, and the model was automatically refined by PHENIX real-space refinement[42] and manually fixed by Coot[41]. In order to consider the interactions between adjacent molecules, nine FljB molecules were used for further refinement, and the central models of FljB was extracted to be the final model. The entire FljB model was made by UCSF Chimera[40] using the helical symmetry. The multi sequence alignment (conservation) was done by Clustal Omega[43]. All the figures of 3D maps and atomic models used in this paper were prepared by UCSF Chimera[40].

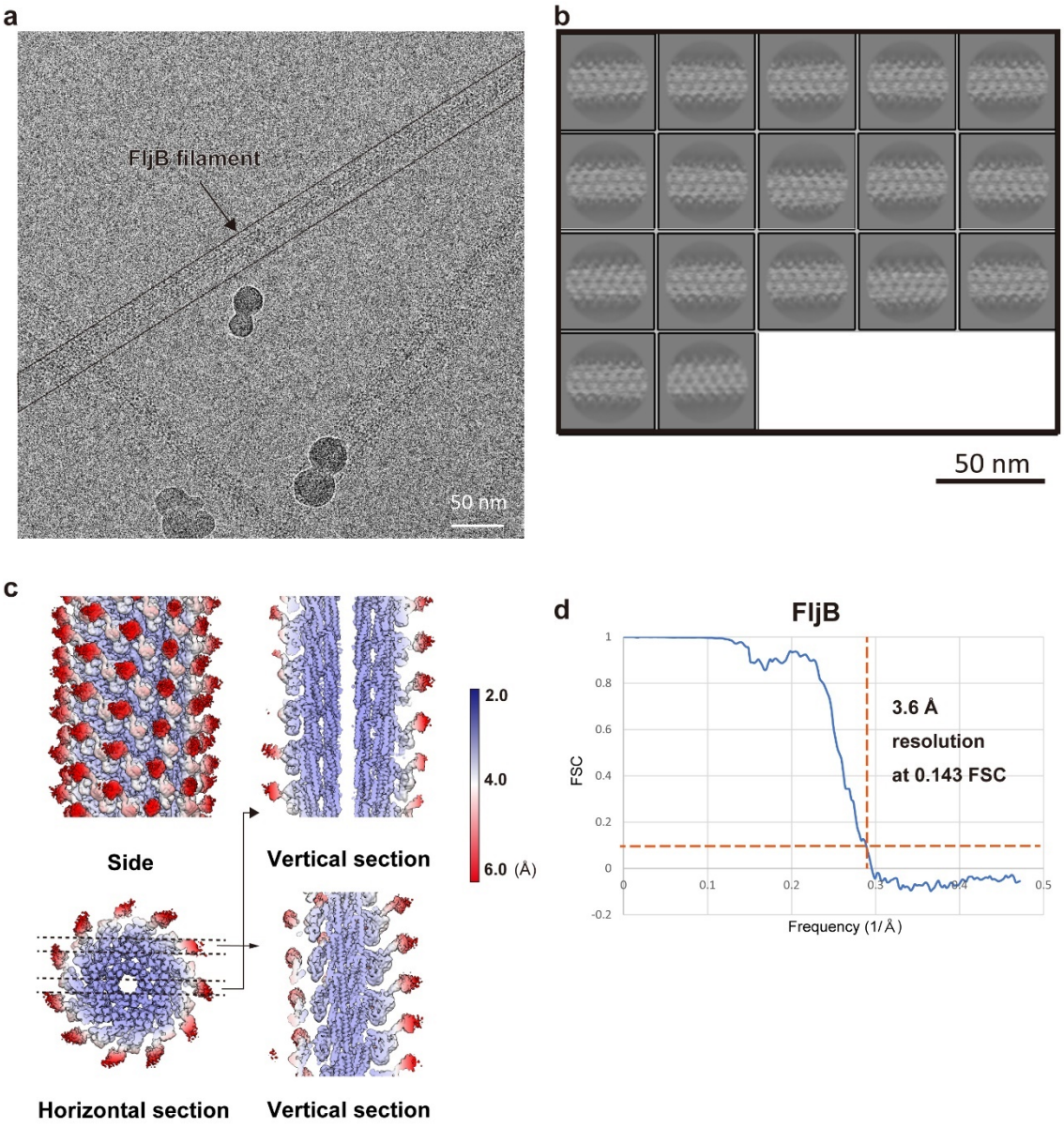

Figure 7 CryoEM single particle image analysis of the FljB filament. **a**, Representative micrograph of the FljB R-type straight flagellar filament. **b**, Selected 2D class averages used for 3D reconstruction of the FljB filament. **c**, The local resolution of the final FljB filament density maps colored from red (6.0 Å) to blue (2.0 Å) calculated by RELION 3.1.1(Ref.[38]). **d**, FSC of the final density map of the FljB filament reconstructed with helical parameters (twist 65.8 degrees and rise 4.7 Å).

Table 2 Conditions of cryoEM grid

Sample	**FljB filament**
Grid	Quantifoil holey carbon grid R1.2/1.3 Mo 200 mesh
Glow discharge (s)	24 s, both sides of grid
Buffer	20 mM Tris-HCl, pH 8.0, 150 mM NaCl, 1 mM $MgCl_2$
Vitrobot Mark IV	
Humidity (%)	100
Temperature (°C)	4
Amount of sample solution	1.5 μL for both sides of grid
Blotting time (s)	3

Table 3 Summary of cryoEM data collection and image analysis for FljB filament

Data collection and processing	
CryoTEM	Titan Krios
Voltage (kV)	300
Camera	Falcon II
Magnification	75,000
Pixel size (Å / pix)	1.06
Total exposure time (sec)	2
No. of frames	7
Frame rate (sec / frame)	0.1
Dose rate par frames (e^- / Å)	10.3
Defocus range (μm)	0.2–1.9
No. of micrographs	2,319
No. of final particle images	197,442 (90% overlap)
No. of final segments	114,110
Symmetry	helical
Resolution (Å)	3.6
FSC threshold	0.143
Validation	
MolProbity score	2.93
Clashscore	68.79
Poor rotamers (%)	1.86
Ramachandran plot	
Favored (%)	93.61
Allowed (%)	5.47
Disallowed (%)	0.92

Results

Motility difference between cells with the FljB and FliC filaments

In order to investigate whether the two different types of flagellar filaments affected swimming motility, first the swimming speed and the population of motile cells were measured for cells with the FljB and FliC filaments in motility buffer solutions of different viscosities adjusted by adding Ficoll. Optical microscopy was used for this observation. The wild-type *Salmonella* LT2 strain has two distinct flagellin genes, *fliC* and *fljB,* on the chromosome, and their expressions are switched autonomously (see Introduction of Chapter A). Therefore, the two LT2-derived strains, SJW1103 expressing only FliC and SJW1103B expressing only FljB, were used to examine functional differences between these two flagellar filaments. These strains both showed similar rates of growth (Figure 8). The swimming speed of SJW1103 markedly decreased as the Ficoll concentration increased. When Ficoll was added to a final concentration of 10%, the average swimming speed decreased to 44% of that measured in the motility buffer without Ficoll. In contrast, the swimming speed of SJW1103B decreased only to 73% in the motility buffer with 10% Ficoll (Figure 9a). In addition, the decrease in the motile cell population of SJW1103B was much less than that of SJW1103. In the presence of 15% Ficoll in the motility buffer, 72% of SJW1103B cells were swimming while the motile fraction of SJW1103 cells was only 32% (Figure 9b). To examine the morphology (the length and number of flagellar filaments per cell), the filaments were stained by immunofluorescence staining after 6 hours of culture in LB and were observed by fluorescence microscopy. On average, most of the cells had three to five filaments, and their lengths were about 10 μm regardless of the strain, and no statistical difference was observed between the two strains ($p > 0.05$) (Figure 9cd).

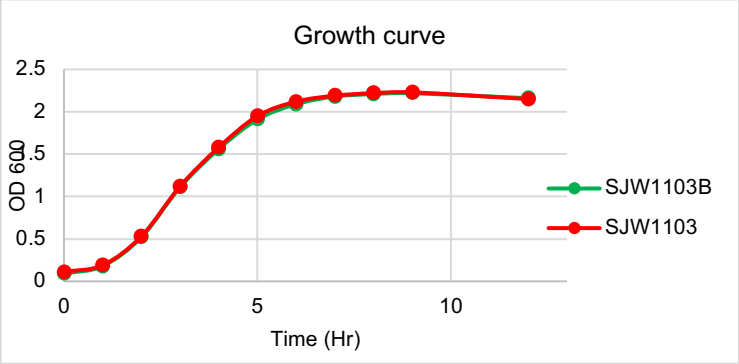

Figure 8 Growth curves of *Salmonella* strains SJW1103 and SJW1103B. Each circle dot is the actual data point measured by optical density weave length of 600 nm (OD_{600}). There was no difference between two strains.

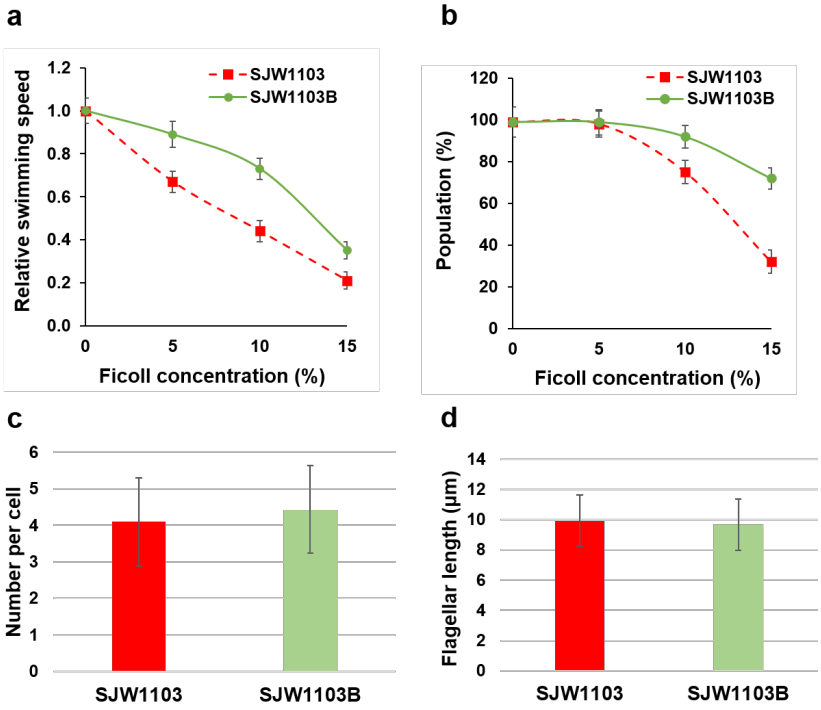

Figure 9 Motility and filament characteristics of *Salmonella* strains SJW1103 and SJW1103B. a, Changes in the swimming speed and **b**, changes in the swimming cell population under different viscosity conditions created by adding Ficoll to the motility buffer. **c**,**d**, Number per cell and length of the flagellar filaments. Comparisons between datasets were performed using a two-tailed Student's *t*-test. A *P* value of < 0.05 was statistically significant difference and no statistical difference was observed under either condition.

Structures of the FljB and FliC filaments

The FljB filament was purified from the *Salmonella* SJW590 cells (see Methods of Chapter A) that forms the filament of R-type straight form (Figure 3), and cryoEM images of the filaments were collected and analyzed by single particle image analysis using RELION 3.0-β2 (Ref.[38]; Table 3 and Figure 7). The R-type straight form was used to utilize the helical symmetry for image analysis as well as to compare the structure with the R-type straight filament formed by FliC. The 3D image of the FljB filament was reconstructed at 3.6 Å resolution from about 1.1 million segment images obtained from 2,319 cryoEM movie images (Figure 7 and 10, Table 3). It showed a tubular structure formed by a helical assembly of subunit proteins with an outer diameter of 230 Å and an inner diameter of 20 Å and with a similar helical parameter to the R-type straight filament formed by FliC (Table 4). The 11 protofilaments could also be recognized as in the FliC filament structure[27–29,44]. As revealed previously[27–29,44], the subunit consisted of four domains, D0, D1, D2 and D3, arranged from the inner to the outer part of the tube. Domains D0 and D1 formed the inner tubes while domains D2 and D3 formed the outer part, with domain D3 exposed on the surface of the filament. The sequence regions forming these four domains are indicated in Figure 6, in which the high sequence homology between FljB and FliC is also presented (FljB/FliC sequence alignment shows 76% identity and 1.4×10^{-66} *E*-value; Figure 6). The helical parameters of the FljB filament determined in this study were also identical to those of the R-type FliC filament[29] (Table 4), which is reasonable considering the high sequence homology between these two flagellins in the N- and C-terminal regions that form the core of the filament tube.

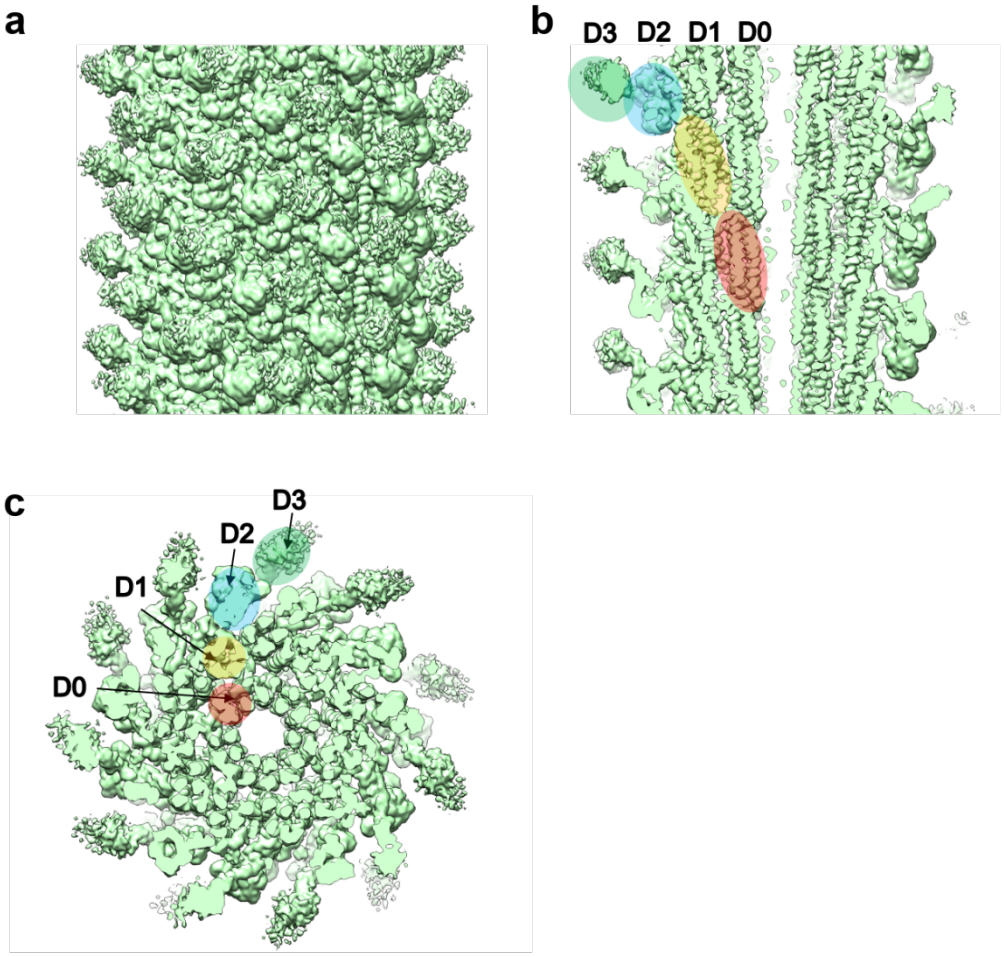

Figure 10 The 3D density map of the FljB filament resolved by cryoEM image analysis. a, Side view of the filament surface. **b**, The longitudinal section along the filament axis. **c**, The cross section viewed from the distal end. The four domains of FljB, D0, D1, D2, and D3, are labeled in different colors in (**b**,**c**).

Table 4 The helical parameters of the FljB and FliC R-type straight flagellar filaments

	Rotation (degrees)	Axial Rise (Å)
FljB	65.81	4.69
FliC	65.84	4.71

To build the atomic model of the FljB filament, a homology model was first generated from the atomic model of the FliC filament[28] (PDB ID: 1UCU; Figure 6 and 11a) using MODELLER[39], then fitted into the 3D density map and refined using UCSF Chimera[40], Coot[41], and Phenix[45] (Figure 11b). The model of FljB (PDB ID: 6JY0) in the filament structure contained 81% of whole residues; 1–192 and 288–505, which covered domains D0, D1, and D2 (Figure 6). The missing residues 193–287, corresponding to domain D3, were not built because the resolution of the 3D map was too low to trace the chain (Figure 11b). In addition, the density level of domain D3 was much lower than other domains of FljB (Figure 11c), indicating that domain D3 is more mobile than other domains of FljB. This indicates that the two-chain hinge connection between domains D2 and D3 is relatively flexible, making domain D3 mobile. The structures of domains D0 and D1 were nearly identical between FljB and FliC, with the root mean square deviation of Cα atoms being 2.8 Å (Figure 11de). Domain D2 is composed of two subdomains, D2a and D2b, and while the D2b domain (residues 356–412 for FljB and 345–401 for FliC) was nearly identical between the two flagellins, the D2a domain (residues177–189, 294–355 for FljB and 177–189 and 284–344 for FliC) showed a small difference in their conformations due to a four-residue insertion in FljB (Asp 310–Gly 314) (Figure 6, 11e and 12).

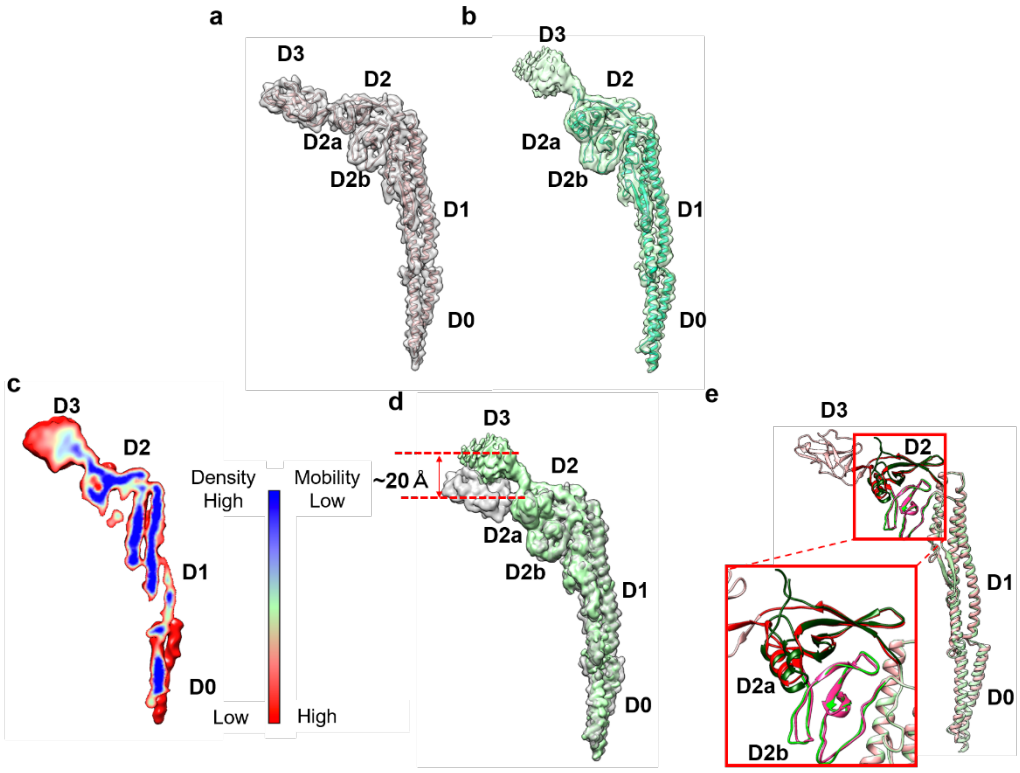

Figure 11 Comparison of subunit structures of the FliC and FljB filaments. The 3D map and Cα ribbon model of **a**,**b**, FliC (PDB ID: 1UCU) and FljB (PDB ID: 6JY0). The map of FljB was obtained by cryoEM image analysis, while that of FliC was generated from the atomic model. The Cα ribbon model of domain D3 is not shown for FljB because the resolution of this domain was too low to trace the chain. **c**, The color-coded density distribution of FljB in a longitudinal section of the molecule. The relatively low density of domain D3 indicated a high mobility of this domain. **d**, Superposition of the two maps with FljB in light green and FliC in gray. **e**, The Cα ribbon model of FljB in light green is superimposed on that of FliC in light pink. The structures of FljB and FliC were nearly identical for domains D0, D1, and D2b, but the folding of part of domain D2a connecting to domain D3 was distinct between the two, which was responsible for the tilt of domain D3 of FljB, making its position higher than that of FliC by about 20 Å.

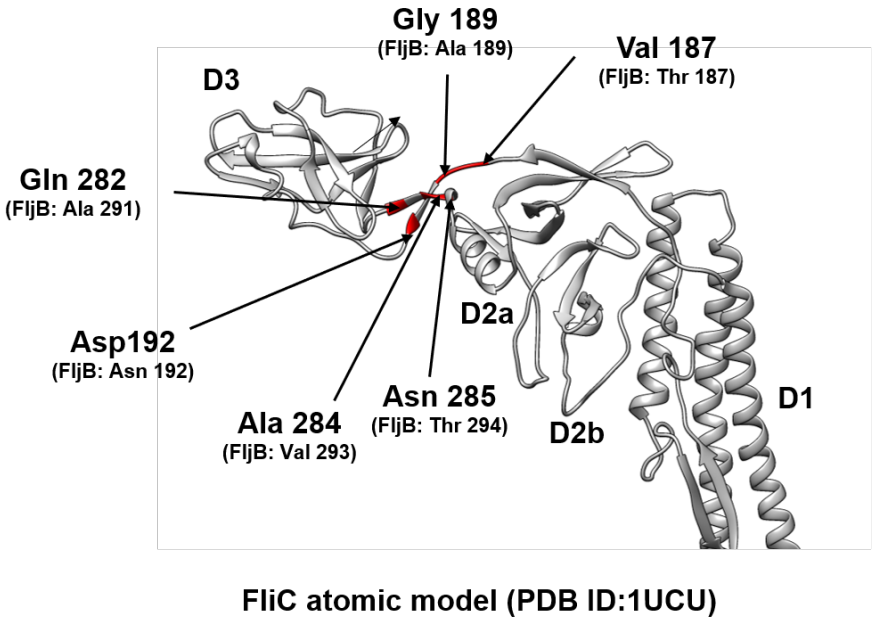

Figure 12 Differences in residue numbers and types between FliC and FljB mapped on the FliC model. Differences are shown for residues 187–192 and 282–285 of FliC and residues 187–192 and 291–294 of FljB. The FliC chain is colored red for those residues that are different from FljB.

Difference in the position and orientation of domain D3

The distinct difference in the two filament structures was the position and orientation of domain D3 relative to D2. When domains D0, D1, and D2 were superimposed between FljB and FliC, domain D3 of FljB was tilted from that of FliC by about 30°, making its position nearly 20 Å higher than that of FliC (Figure 11de). The two antiparallel chains connecting domains D2 and D3 were highly tilted in FljB to generate this difference (Figure 11e). Near this two-chain domain connection, FliC had close contacts between Ala-191, Val-283 and Asp-339, with a Cα distance of 4.9 Å between Ala-191 and Asp-339, making the conformation of this two-chain domain connection stable (Figure 13a). Unlike FliC, FljB did not have these contacts, with the corresponding Cα distance between Ala-191 and Thr-350 being 18.4 Å (Figure 13b), possibly making the two-chain domain connection less stable and domain D3 oriented differently than FliC. As a result, domain D3 of FljB was more mobile than that of FliC, and the FljB and FliC filaments had different lateral intermolecular interactions of the D2 and D3 domains between neighboring protofilaments.

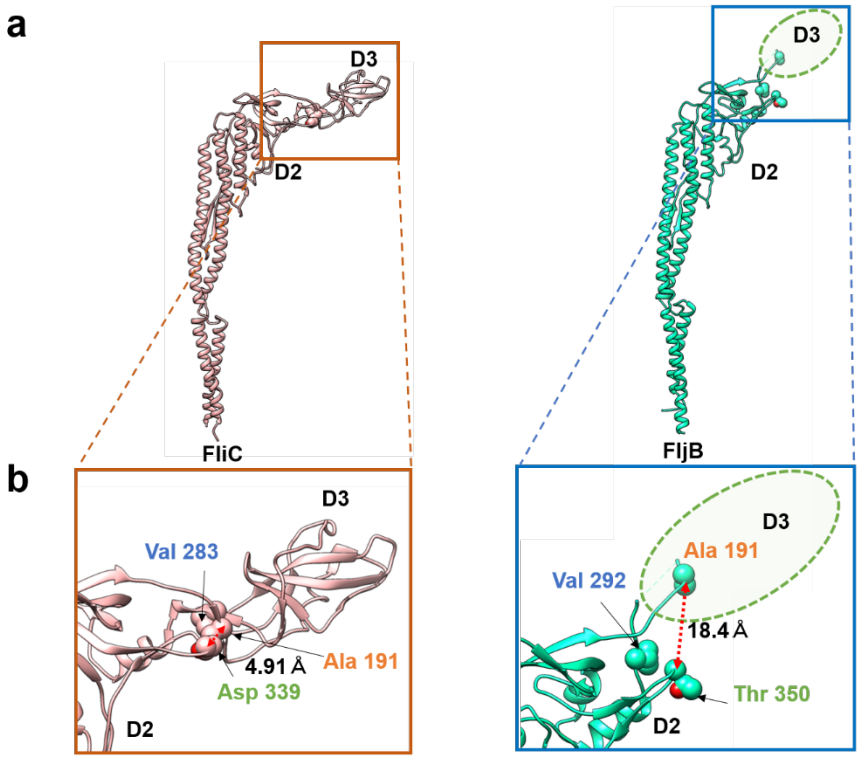

Figure 13 Interactions of residues stabilizing the position and orientation of domain D3 in FliC. a, The Cα ribbon models of FliC (left) and FljB (right) with three residues important for stabilizing the position and orientation of domain D3 in space-filling representation. **b**, Magnified view of the parts indicated by the boxes in panel **a**. The ellipse in dashed line in the lower panel indicates the position of domain D3 of FljB. The corresponding residues of FliC and FljB are labeled in the same colors, orange (FliC Ala 191 and FljB Ala 191), blue (FliC Val-283 and FljB Val-292), and green (FliC Asp-339 and FljB Thr-350). In FliC, the three residues were closely packed each other by hydrophobic interactions, stabilizing the position and orientation of domain D3, while they were far apart in FljB, as indicated by the distances.

Axial intermolecular interaction along the 11 start protofilaments

N- and C-terminal residues of flagellin molecule are disordered in solution but form three-dimensional structure upon polymerization and play an important role for filament stabilization. Deletion of the N-terminal residues reduced the filament stability more strongly than deletion of the C-terminal residues, suggesting that the N-terminal residues region is more important for the filament stability[46]. In the FljB filament structure, I newly identified an interesting axial intermolecular interaction between the D0 domains that contributes to the filament assembly and stability. Along each of the 11 protofilaments, the N-terminal five residues of subunit 1 above (on the distal side of the filament) extends perpendicular to the filament axis before forming the N-terminal α-helix and forms an antiparallel β-strand with the extended C-terminal chain connecting domains D0 and D1 of subunit 2 below (on the proximal side of the filament) (Figure 14). Residue Gln-2 of subunit 1 and Tyr-469 of subunit 2 form a hydrogen bond between the main chains (Figure 14c). This explains why the N-terminal residues are more important than the C-terminal residues for the filament stability[46] .

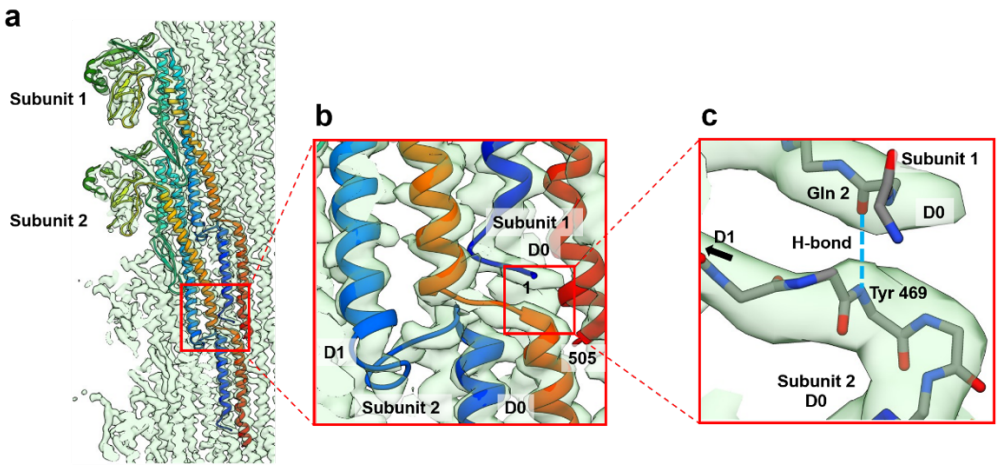

Figure 14 The folding and intersubunit interaction of the five N-terminal residues of FljB contributing to the assembly and stabilization of the filament structure. a, The Cα ribbon models of two neighboring FljB subunits along the protofilament are shown in rainbow colors from the N-terminus in blue to the C-terminus in red. **b**, The five N-terminal residues are extended, lying flat on the short extended chain connecting the C-terminal α-helices of domains D0 and D1 of a subunit below along the protofilament, forming an antiparallel β-strand to stabilize the axial intersubunit interactions. **c**, The residue Gln 2 of subunit 1 and Tyr 469 of subunit 2 forms a hydrogen bond between the main chains (dashed line in right blue). In panel **c**, only main chain backbone atoms are shown (nitrogen and oxygen atoms are colored blue and red, respectively).

Discussion

To investigate the potentially different physiological roles played by the two types of flagellar filaments formed by FljB and FliC, motility assays of the two strains expressing either FljB or FliC and structural analysis of the FljB filament were carried out for comparison with the FliC filament.

There were no significant differences between the strain SJW1103B producing the FljB filament and SJW1103 forming the FliC filament, either in the number of filaments per cell, their filament length, or their swimming speed in the motility buffer. However, their swimming speeds were clearly different under high-viscosity conditions, with a markedly smaller reduction in the swimming speed of SJW1103B than that of SJW1103 when the viscosity was increased by the addition of Ficoll in the motility buffer. These results indicate that the differences in the structure and dynamics of their flagellar filaments must be responsible for the difference in their motility.

I therefore examined the structure of the FljB filament by cryoEM single-particle image analysis in one of the two mutant straight forms called the R-type to utilize the helical symmetry. The overall structure was very similar to that of the FliC filament except for the position and orientation of the outermost domain D3 exposed on the surface of the filament. Recently, the FljB structure with domain D3 has been revealed by X-ray crystallography[24], and the overall structure of domain D3 of FljB has been shown to be similar to that of FliC. However, the orientation of domain D3 relative to domain D2 in the filament structure was different between the FljB and FliC filaments. Therefore, the positional and orientational difference of domain D3 between FljB and FliC seem to result from the sequence connecting domain D2 and D3. Domain D3 of FljB showed a higher flexibility and mobility than that of FliC in the filament structure. These differences suggest that domain D3 plays an important role not only in changing antigenicity but also in optimizing the motility function of the filament as a propeller under different conditions of solvent viscosity.

The differences in the relative position and dynamics of domain D3 are well correlated with the differences in amino acid sequence between FljB and FliC, which are found in regions Val-187 to Gly-189 and Ala-284 to Asn-285 and residues Asp-192 and Gln-282 of FliC, which form the two antiparallel chains connecting domains D2 and D3

(Figure 6 and 12). In FliC, the position and orientation of domain D3 is stabilized by hydrophobic interactions between Ala-191, Val-283 and Asp-339. On the other hand, the distances between corresponding residues in FljB, Ala-191, Val-292, and Thr-350, are much longer than those of FliC, making the stabilizing hydrophobic interactions impossible (Figure 13). As a result, the D3 domain of FljB is more mobile than that of FliC.

How the differences in the structure and dynamics of the D3 domains on the surface of the FljB and FliC filaments contribute to their different motility functions as a propeller is difficult to answer without examining the role of domain D3 via fluid dynamic simulations. A previous result that deletion of domain D3 does not change the motility but reduce the invasion rate to MODE-K cells[24] suggests that the domain D3 increases the filament surface and help the cells anchor to the target site. If so, the more rigid domain D3 of FliC may be more easily "captured" in the viscous environment than the flexible domain D3 of FljB. Anyway, there must be some advantages of a higher mobility of surface domains for the helical propeller in generating higher thrust under high-viscosity conditions, such as in mucosa, which pathogenic bacteria have to swim through to reach host cells. The higher mobility domain D3 of FljB may also be advantageous to swim inside biofilms consisting of extracellular polymeric substances (EPS). Since the nutrient inside the biofilm do not diffuse naturally because of its high viscosity, a few % of motile cells are required to deliver nutrition to other cells in biofilms[47,48]. The cells with the FljB filaments may have an important role in keeping the biofilm in desired conditions, and the amino acid sequence of FljB may have been optimized for such purpose by evolution.

Chapter B

Structure and functions of the bushing of the flagellar motor

Introduction

Characteristics of the LP ring as a molecular bushing

The LP ring acts as a bushing of the flagellar motor in Gram-negative bacteria such as *Salmonella* and *Vibrio*. The Gram-positive bacteria do not have the LP ring, suggesting that the thicker PG layer acts as a bushing of the flagellar motor[49]. The flagellar motor of *Salmonella* can rotates at a speed around 300 rps[4], as fast as Formular one race car engines. The motor of *Vibrio alginolyticus* can rotate at a speed up to 1,7000 rps , which is five to six times faster than that of *Salmonella*[5]. These suggest that the inner surface of the LP ring must be very smooth to sustain such high-speed rotation of the rod as a drive shaft. The L and P ring tightly interacts with each other and are observed mostly as the LP ring complex, which is very stable against various chemical treatment such as acid and urea[50,51] and remains in the cell envelope with its central pore sealed even after the ejection of the flagellar axial structure containing the rod, hook and filament from the cell body[52–56]. The detailed information of the LP ring structure was not available because it is difficult to crystallize it for X-ray crystal structural analysis. CryoEM structural analysis was difficult because of a preferred orientation of purified LP ring in the amorphous ice film of cryogrid.

Assembly mechanism of the LP ring around the distal rod

The genes expressions of the flagellar motor component proteins are arranged in a hierarchical manner, and the protein assembly proceeds from the cytoplasm to the outside the cell (Figure 15). First, the MS ring is formed within the cytoplasmic membrane, and the C ring is assembled on the cytoplasmic face of the MS ring. FliE is secreted via a flagellum-specific type III export apparatus and assembles into the most proximal part of the rod at the tip of the export apparatus. Then, FlgB, FlgC, FlgF and FlgG assemble into the rod in this order[57]. The rod complex penetrates the peptidoglycan layer with the help of the flagellum-specific muramidase FlgJ[4,58]. The LP ring complex is assembled around the distal rod to act as a busing. L ring formation facilitates the removal of the FlgJ cap from the rod tip, followed by the assembly of FlgD into the hook cap at the distal end of

the rod[59]. The L ring forms a pore in the outer membrane and allows the elongation of the hook and filament in the cell exterior.

Unlike the other flagellar components that are exported through the flagellum-specific transporter of the flagellar motor complex, FlgH and FlgI are synthesized in the cytoplasm as precursor proteins with a cleavable N-terminal signal peptide, and they are translocated to the periplasm by the Sec translocon[60]. The N-terminal signal peptides are cleaved during the translocation across the cell membrane[61,62]. FlgI molecules assemble around the distal rod with the help of FlgA chaperone, which is also secreted via the Sec-translocon, to form the P ring[63,64]. FlgI requires a help of DsbA and DsbB to form a intramolecular disulfide bond that is not essential but helpful for its efficient assembly to form the P ring around the rod[65]. The P ring tightly associates with the PG layer, allowing the LP ring to act as a molecular bushing. Before the L ring assembly, the P ring tightly attach to the rod. Certain point mutations in the distal rod protein FlgG not only produce abnormally elongated rods called the polyrod but also allow many P rings to be formed around them, suggesting that the well-regulated P ring formation involves interactions of specific amino acid residues of FlgG and FlgI[59,66]. The N-terminal domain of FlgI consisting of residues 1–120 is critical not only for the stabilization of the FlgI structure but also for the formation of the P ring complex[67].

After secretion of FlgH into the periplasm by the Sec-dependent pathway, FlgH is subjected to the outer membrane sorting system Lol[68] and modified for outer-membrane localization. The N-terminus of FlgH has a canonical cysteine residue that is acylated with palmitate or other available long-chain fatty acids, thereby anchoring the L ring to the outer membrane[69]. From previous biochemical studies, the L ring and P ring were thought to be composed of 26 copies of FlgH and FlgI proteins, respectively[70,71]. Because the L ring is not formed in *flgI* null mutants, FlgH assembly around the rod presumably requires prior assembly of FlgI into the P ring[52,57]. The C-terminal chain of FlgH is supposed to be responsible for its binding to the P ring[69], and the FlgH binding to the P ring may induce some conformational changes in the P ring to make it dissociate from the rod and enable the LP-ring to act as a bushing. However, the detailed mechanism of LP ring formation remains elusive due to the lack of structural information.

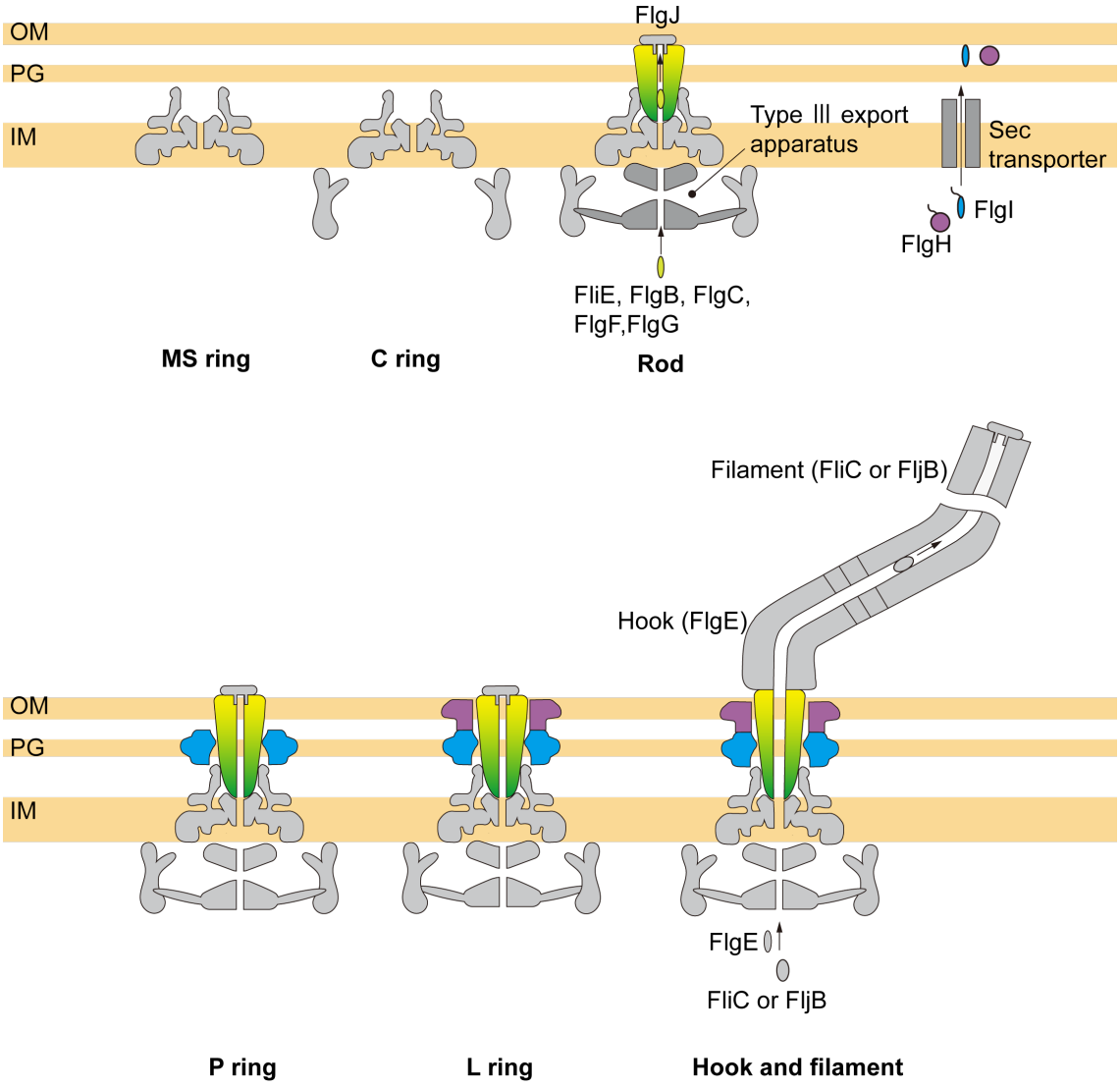

Figure 15 Assembly order of flagella. First, the MS ring and C ring were assembled. The rod component proteins (FliE, FlgB, FlgC, FlgF, FlgG; yellow) and flagellum specific muramidase (FlgJ; grey) were secreted via type III export apparatus while the LP ring component proteins, FlgH (purple) and FlgI (cyan) are secreted via Sec transporter. After P ring assembled around the rod, the L ring assembles on it. The FlgE and FliC/FljB are then exported to the outside via type III export apparatus and form the hook and the filament. OM, PG, IM are referring to outer membrane, PG layer, inner membrane, respectably.

Structure and characteristics of the rod

The rod is composed of the proximal and distal rods. The proximal rod consists of 6 FliE, 5 FlgB, 6 FlgC and 5 FlgF subunits, and the distal rod consists of 24 FlgG subunits. They are arranged from inside to outside the cell[72]. FlgE (the hook protein) and FlgG are identical in the N- and C-terminal regions (39% homology in amino acid sequence) although the rod and hook have different mechanical and physical properties. Such differences come from the tip portion of a long β-hairpin structure called "L-stretch" of FlgG, which makes the rod rigid and straight[73]. Although there were high-resolution structure of the distal rod reveled by cryoEM structural analysis of the polyrod formed by a *flgG* mutant and of the wild type rod formed by FlgG and FlgF and there were also the atomic model of a FlgG core fragment by X-ray crystallography, the structure of the tip of the L-stretch was not available due to a limited resolution of the cryoEM structure and the terminal truncations of FlgG for crystallization[9,10,72,74].

High-resolution structure of the rod shows that its outer surface is smooth and highly negatively charged[9,10,72,74], leading to a plausible hypothesis that the inner surface of the LP ring may also be smooth and negatively charged to generate electrostatic repulsive force to keep the rod rotating at the center of the LP ring with a minimal friction between them. However, how FlgI and FlgH assemble around the rod to form the LP ring against the repulsive force remains unclear.

Purpose of this study

Due to the lack of structural information, it remains elusive why the LP ring is so stable and how the LP ring assembles around the rod against the repulsive force, as well as how the LP ring and rod interact with each other during motor rotation. To clarify the interactions between the LP ring and rod as well as the assembly mechanism of the LP ring, I carried out cryoEM structural analysis of the LP ring in the flagellar basal body from S*almonella* and genetic, biochemical and physiological experiments.

Materials and Methods

Salmonella strains, plasmids, and media

Bacterial strains and primers of *Salmonella enterica* serovar Typhimurium and plasmids used in this study are listed in Table 5 and Table 6. For cryoEM structural analyses of hook-basal body and LP ring, a strain expressing only the hook-basal body and not the filament (HK1002) was used. For P ring on polyrod analysis, a strain expressing polyrod (*flgG* G65V) with multiple P ring was used (HK26292). For analyzing the function of FlgI, SJW203 that lost *flgH* and *flgI* allele was used as host cell and pTY03 plasmid encoding *flgH* and *flgI* with mutations in *flgI* were used.

Luria–Bertani broth (LB) were used as a culture media containing 1% (w/v) tryptone, 0.5% (w/v) yeast extract, 0.5% (w/v) NaCl. The 0.75% (w/v) and 0.35% of Bacto agarose was added to LB for LB plates and soft agar plates, respectively. If needed, 100 μg/mL ampicillin was added to those media.

DNA manipulation

All primers used in this study were listed in Table 6. The *flgHI* genes were amplified by TaKaRa Ex Taq® DNA polymerase (TaKaRa Bio) using the chromosomal DNA of the *Salmonella* wild-type strain SJW1103 as a template and primers, FlgHI_NdeI_Fw_2 and FlgHI_BamHI_Rv_3. The PCR products were digested with NdeI and BamHI and cloned into the NdeI and BamHI sites of the pET22b vector (Novagen) to generate a plasmid, pTY03. In order to clarify whether the positively charged Lys-63 and Lys-95 of FlgI is important for forming the P ring upon interacting with negatively charged surface of FlgG, each or both Lys-63 and Lys-95 were replaced by Ala or Asp residue. Site-directed mutagenesis was carried out using primer STAR® MAX DNA polymerase (TaKaRa Bio). The mutated genes were amplified by PCR using pTY03 as a template and pairs of complementary primers containing a mutagenized codon listed in Table 6, and then the plasmids were introduced to *E. coli* NovaBlue cells (Novagen) for transformation.

Swarming assay

For swarming assay, *Salmonella* SJW203 cells (Δ*flgH-flgI*) were transformed with a pET22b-based plasmid encoding FlgH and FlgI (pTY03) (Table 5) or its mutant variants. Fresh transformants were inoculated onto soft agar plates with 100 μg/mL ampicillin and incubated at 30°C for 8.5 hours or 24 hours. Five to eight independent measurements were performed.

Measuring the number of flagellar filaments

Salmonella SJW203 cells (Δ*flgH-flgI*) harboring a pET22b-based plasmid encoding FlgH and FlgI (pTY03) (Table 5) or its mutant variants were grown overnight in 5 mL LB with gentle shaking at 30ºC overnight. A 1 mL of the culture media was centrifuged, and cells were collected as pellet. Those cells ware gently washed and re-suspended by Milli-Q water, and stained by 0.2% phosphotungstic acid (PTA) on a thin carbon-coated, 20 seconds glow-discharged copper grid and observed by a JEM-1011 transmission electron microscope (JEOL, Akishima, Japan) operated at an accelerating voltage of 100 kV. For each of the mutant strains, the number of filaments per cell was counted for 100 cells manually.

Secretion assay

Salmonella SJW203 cells (Δ*flgH-flgI*) harboring a pET22b-based plasmid encoding FlgH and FlgI (pTY03) (Table 5) or its mutant variants were grown overnight in 5 mL LB with gentle shaking at 30ºC. A 50 μL of each overnight culture was inoculated into 5 mL LB and incubated at 30ºC with shaking until the cell density had reached OD_{600} of 1.4–1.6. Cultures were centrifuged to obtain cell pellets and culture supernatants. The cell pellets were resuspended in a sample buffer solution [62.5 mM Tris-HCl, pH 6.8, 2% sodium dodecyl sulfate (SDS), 10% glycerol, 0.001% bromophenol blue] containing 1 μL of 2-mercaptoethanol. Proteins in the culture supernatants were precipitated by 10% trichloroacetic acid and suspended in a Tris/SDS loading buffer[75] (one volume of 1 M Tris, nine volumes of sample buffer solution) containing 1 μL of 2-mercaptoethanol. Both whole cellular proteins and culture supernatants were normalized to a cell density of each culture to give a constant cell number. After boiling proteins in both whole cellular and culture supernatant fractions at 95ºC for 3 min, these protein samples were separated by SDS–polyacrylamide gel (normally 12.5% acrylamide) electrophoresis (SDS–PAGE) and transferred to nitrocellulose membranes (Bio-Rad) using a transblotting apparatus (Hoefer). Then, immunoblotting with polyclonal anti-FlgE, anti-FliC, anti-FlgH or anti-FlgI antibody (Medical & Biological Laboratories Co., LTD.) with 400-fold dilution was carried out using iBand Flex Western Device (Thermo Fisher Scientific) as described in the manufacturer's instructions. Anti-Rabbit IgG, HRP-Linked Whole Ab Donkey (GE Healthcare, Cat#SE250-10A-.75) with 1,000-fold dilution was used as secondary antibody. Detection was performed with Amersham ECL Prime western blotting detection reagent (Cytiva). Chemiluminescence signals were captured by a Luminoimage analyzer LAS-3000 (GE Healthcare). The band intensity of each blot was analyzed using an image analysis software, CS Analyzer 4 (ATTO, Tokyo, Japan). All image data were processed with Photoshop software (Adobe).

Table 5 Strains and plasmids used in chapter B

Strains and plasmid	Relevant Characteristics	Source or Reference
***Salmonella* strains**		
HK1002	Not forming the filament Δ*flgK*, Δ*cliP*::Cm^r	Ref.[76]
SJW203	LP ring deletion mutant Δ*flgH-flgI*	Shigeru Yamaguchi & Ref.[77]
HK26292	Polyrod with multiple P rings *flg*G(G65V) *flh*D8070 *flh*C8092 *fli*A5225 Δ*fliB*-T7771 Δ*rfl*M8403 *fljBenx* vh2 Δ*fliK*	Kelly T. Hughes
Plasmids		
pET22b	Expression vector	Novagen
pTY03	pET22b/FlgH+FlgI	Ref.[78]
pTY03(K63A)	pET22b/FlgH+FlgI(K63A)	
pTY03(K63D)	pET22b/FlgH+FlgI(K63D)	
pTY03(K95A)	pET22b/FlgH+FlgI(K95A)	
pTY03(K95D)	pET22b/FlgH+FlgI(K95D)	
pTY03(K63A/K95A)	pET22b/FlgH+FlgI(K63A/K95A)	
pTY03(K63A/K95D)	pET22b/FlgH+FlgI(K63A/K95D)	
pTY03(K63D/K95A)	pET22b/FlgH+FlgI(K63D/K95A)	
pTY03(K63D/K95D)	pET22b/FlgH+FlgI(K63D/K95D)	

Table 6 Primers used in chapter B

Mutated residue	Primer	Sequence (5'–3')
	FlgHI_NdeI_Fw-2	CATATGCAAAAATACGCGCTTCACGC
	FlgHI_BamHI_Rv-3	CTCGGATCCTCAGATGATTTCCAGTTTGGCGCG
K63A	FlgI_K63A_Fw	CAGTTGGCAAACGTGGCGGCGGTGATGGTGACG
	FlgI_K63A_Rv	CACGTTTGCCAACTGCATATTGGTGCCGGTGGG
K63D	FlgI_K63D_Fw	CAGTTGGATAACGTGGCGGCGGTGATGGTGACG
	FlgI_K63D_Rv	CACGTTATCCAACTGCATATTGGTGCCGGTGGG
K95A	FlgI_K95A_Fw	AACGCTGCAAGTCTGCGTGGCGGGACGTTATTA
	FlgI_K95A_Rv	CAGACTTGCAGCGTTCCCCATTGAGGAAACAAC
K95D	FlgI_K95D_Fw	AACGCTGATAGTCTGCGTGGCGGGACGTTATTA
	FlgI_K95D_Rv	CAGACTATCAGCGTTCCCCATTGAGGAAACAACGAC
K63A/ K95A	FlgI_K63A_Fw	CAGTTGGCAAACGTGGCGGCGGTGATGGTGACG
	FlgI_K63A_Rv	CACGTTTGCCAACTGCATATTGGTGCCGGTGGG
	FlgI_K95A_Fw	AACGCTGCAAGTCTGCGTGGCGGGACGTTATTA
	FlgI_K95A_Rv	CAGACTTGCAGCGTTCCCCATTGAGGAAACAAC
K63A/K95D	FlgI_K63A_Fw	CAGTTGGCAAACGTGGCGGCGGTGATGGTGACG
	FlgI_K63A_Rv	CACGTTTGCCAACTGCATATTGGTGCCGGTGGG
	FlgI_K95D_Fw	AACGCTGATAGTCTGCGTGGCGGGACGTTATTA
	FlgI_K95D_Rv	CAGACTATCAGCGTTCCCCATTGAGGAAACAACGAC
K63D/K95A	FlgI_K63D_Fw	CAGTTGGATAACGTGGCGGCGGTGATGGTGACG
	FlgI_K63D_Rv	CACGTTATCCAACTGCATATTGGTGCCGGTGGG
	FlgI_K95A_Fw	AACGCTGCAAGTCTGCGTGGCGGGACGTTATTA
	FlgI_K95A_Rv	CAGACTTGCAGCGTTCCCCATTGAGGAAACAAC
K63D/K95D	FlgI_K63D_Fw	CAGTTGGATAACGTGGCGGCGGTGATGGTGACG
	FlgI_K63D_Rv	CACGTTATCCAACTGCATATTGGTGCCGGTGGG
	FlgI_K95D_Fw	AACGCTGATAGTCTGCGTGGCGGGACGTTATTA
	FlgI_K95D_Rv	CAGACTATCAGCGTTCCCCATTGAGGAAACAACGAC

Statistical analysis
Statistical analyses were done using Kaleida Graph (Synergy Software) or Excel 2016 (Microsoft). Comparisons between datasets were performed using a two-tailed Student's *t*-test. A P value of < 0.05 was considered to be statistically significant difference. Figures were drawn by Excel 2016 or in-house program written by python 2.7 (libraries; NumPy, pandas, matplotlib, seaborn).

CryoEM sample purification
For purifying hook basal body (HBB) for LP ring analysis, a strain expressing only the hook-basal body and not the filament (HK1002) was used. The *Salmonella* HK1002 cells were pre-cultured in 30 mL LB overnight with shaking at 37°C and inoculated into a 2.6 L of fresh LB. The cells were grown until the optical density had reached an OD_{600} of about 1.0. The cells were collected by centrifugation and resuspend in 10% sucrose buffer [10% (w/v) sucrose, 0.1 M Tris-HCl, pH 8.0]. EDTA (pH 8.0) and lysozyme were added to final concentrations of 10 mM and 1.0 mg/mL, respectively. The cell lysates were stirred on ice for 1 hour at 4°C, and 0.1 M $MgSO_4$ and 10% (w/v) Triton X-100 were added to final concentrations of 10 mM and 1% (w/v), respectively. After stirring for 1 hour at 4°C, 0.1 M EDTA (pH 11.0) was added to a final concentration of 10 mM. The solution was centrifuged at 15,000 × *g*, and the supernatant was collected. The pH was adjusted to 10.5 with 5 N NaOH and recentrifuged at 15,000 × *g* to remove undissolved membrane fractions. The supernatant was centrifuged at 67,000 × *g* to collect HBBs as a pellet. This pellet was resuspended in 1 mL of Buffer C [10 mM Tris-HCl, 5 mM EDTA, 1% (w/v) Triton X-100] and was centrifuged at 9,700 × *g*, and the supernatant was collected. HBBs were purified by a sucrose density-gradient centrifugation method with a gradient of sucrose from 20% to 50%. Fractions containing HBBs were collected and checked by SDS-PAGE with Coomassie Brilliant Blue staining. The fractions containing HBBs were two-fold diluted by a final buffer [20 mM Tris-HCl, pH 8.0, 150 mM NaCl, 0.05% (w/v) Triton X-100] and the sucrose was removed by centrifugation at 120,000 × *g*. Finally, HBBs were resuspended with 10-50 μL of the final buffer, and the sample solution was stored at 4°C.

For purifying the Polyrod-P ring complex (PRP) for analyzing the intermediate state of P ring assembling around the rod, a strain expressing the polyrod with multiple P ring (HK26292) was used. The *Salmonella* HK26292 cells were pre-cultured in 30 mL LB overnight with shaking at 30°C and inoculated into a 1.5 L of fresh LB. The cells were grown until the optical density had reached an OD_{600} of about 1.0. The cells were collected by centrifugation and resuspend in 10% sucrose buffer [10% (w/v) sucrose, 0.1 M Tris-HCl, pH 8.0] to final concentrations of 1mg/ml. EDTA (pH 8.0) and lysozyme were added to final concentrations of 1 mM and 0.1 mg/mL, respectively. The cell lysates were stirred for 5 min at 4°C and then for 1 hour at room temperature. 0.1 M $MgSO_4$, 10 mg/ml of DNase, and 10% (w/v) Triton X-100 were then added to final concentrations of 10 mM, 0.1 mg/ml and 1% (w/v), respectively. After stirring for 15 min at room temperature for digest DNA, additionally starring for 45 min at 4°C. 0.1 M EDTA (pH 11.0) was added to a final concentration of 10 mM. The solution was centrifuged at 15,000 × *g*, and the supernatant was collected. The pH was adjusted to 12.0 with 5 N NaOH and recentrifuged at 15,000 × *g* to remove undissolved membrane fractions. The supernatant was centrifuged at 67,000 × *g* to collect samples as a pellet. This pellet was

resuspended in 300 µL of TN50I_T [50 mM Tris-HCl, 50 mM NaCl, 25 mM of Imidazole, 0.1% (w/v) Triton X-100] and was centrifuged at 3,500 ×*g* for 10 min, and the supernatant was collected. PRPs were purified by a sucrose density-gradient centrifugation method with a gradient of sucrose from 30% to 60% by centrifugation at 68,000 × *g* for 14 hours. Fractions containing samples were collected and checked by SDS-PAGE with Coomassie Brilliant Blue staining, and were two-fold diluted by a final buffer [50 mM Tris-HCl, 50 mM NaCl, 25 mM Imidazole, 0.002% (w/v) LMNG, 0.05% (w/v) Triton X-100, pH 8.0], and the sucrose was removed by centrifugation at 120,000 ×*g*. Finally, samples were resuspended with 10-50 µL of the final buffer, and the sample solution was stored at 4°C.

Negative staining and EM observation

The condition and concentration of purified samples were checked before making cryoEM sample grid. A 3 µL aliquot of the sample solutions was placed on a thin carbon-coated, 20 seconds glow-discharged copper grid. The extra solution was removed from the grid by blotting, the filaments and cells were stained with 2% and 0.2% phosphotungstic acid (PTA), respectively, and the HBB and PRP were stained with 2% uranyl acetate. The sample grids were dried for 1 hour at room temperature and checked using a transmission electron microscope, JEM-1011 (JEOL, Akishima, Japan) with an accelerating voltage of 100 kV.

Electron cryomicroscopy and image processing

The hook-basal body and LP ring

A 3 µL aliquot of the sample solution was applied to a Quantifoil holey carbon grid R1.2/1.3 Mo 200 mesh (Quantifoil Micro Tools GmbH, Großlöbichau, Germany) with pretreatment by glow discharge (one side of grid). The grids were blotted and plunged into liquid ethane at the temperature of liquid nitrogen for rapid freezing[36] with Vitrobot Mark IV (Thermo Fisher Scientific) with a blotting time of 5 seconds at 4°C and 100% humidity (Table 7). Grids were then transferred into electron cryomicroscope with a cryostage cooled by liquid nitrogen.

The data collection of the HBB were operated on a prototype of CRYO ARM 200 (JEOL, Japan) equipped with a thermal field-emission electron gun operated accelerating voltage of 200 kV, an Ω-type energy filter with a 20 eV slit width and a K2 Summit direct electron detector camera (Gatan, USA). The 12,759 dose-fractionated movies were automatically collected using the JADAS software (JEOL). Using a minimum dose system, all movies were taken by a total exposure of 10 seconds, an electron dose of 0.9 electrons/Å^2 per frame; a defocus range of 0.2 to 2.0 µm, and a nominal magnification of 40,000×, corresponding to an image pixel size of 1.45 Å. All the 50 frames of the movie were recorded at a frame rate of 0.2 sec/frame. The defocus of each image was estimated by Gctf-v1.06 (Ref.[37]) after motion correction by RELION-3.0-β2 (Ref.[38]). The HBB particle images were automatically picked by an in-house python program (YOLOPick) that utilizes a convolutional neural network program, YOLOv2 (Ref.[79]). In total, 64,418 particles were extracted into a box of 340 × 340 pixels and used for 2D classification by RELION 3.0-β2. First, clear 2D classes were selected (1,515 particles), and the "ignoring CTF first-peak" option was applied for the remaining blur 2D classes (62,841 particles) to select additional 15,902 particles, and in total, 17,363 particles were selected. The 15,242 particles were selected from those 17,363 particles after re-centering their positions by in-house program named TK-center.py, then the

14,975 particles were selected after another 2D classification, and those particles were used for first 3D classification into two classes with C1 symmetry. A density map of better quality, reconstructed from 13,017 particles (87%), was then used as a reference for density subtraction to leave only the LP ring. The C26 symmetry was visible in the LP ring density map, but its cross-section image was transformed from the Cartesian to the polar coordinates, and its autocorrelation function was Fourier transformed to confirm the rotational symmetry to be 26-fold. This estimation was carried out by in-house program named Tksymassign.py. Then, the C26 symmetry was applied for further image analysis to obtain a higher resolution 3D map, which resulted in 3.5 Å resolution at a Fourier shell correlation (FSC) of 0.143 after 3D refinement and CTF refinement procedure from 10,802 particles (EMD-30398) (Figure 16 and 17). In order to obtain detailed information on the relative positioning of the rod and LP ring without any symmetry (C1), 14,975 HBB particle images were extracted with a lager box size from the same movie data sets described above and by using the 3.5 Å resolution LP ring map as a reference for refinement, 14,370 particles were selected after 3D classification and 3D refinement. Because the resolution was not improved by this 3D classification and 3D refinement, 2D classification and centering were also done to this data set. In order not to be affected by the hook density, the reference and mask without the hook density was used for next 3D classification and 3D refinement. A density map of 6.9 Å resolution (at the FSC of 0.143) was obtained with C1 symmetry after 3D refinement and CTF refinement procedure from 14,370 particles (EMD-30409). Although the global resolution of this map was same as the initial HBB map, the local resolution was improved. The summary of cryoEM data collection and statistics is shown in Table 8.

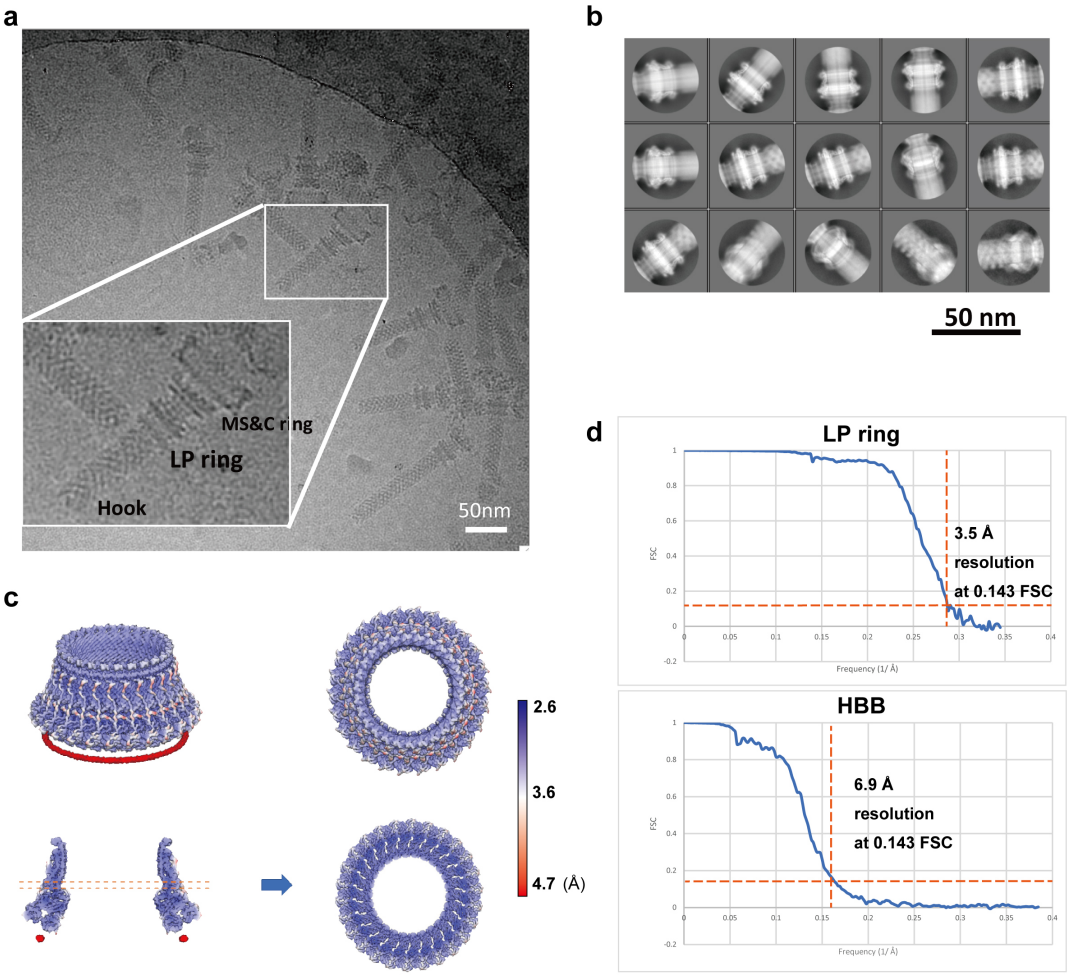

Figure 16 CryoEM single particle image analysis of the LP ring. **a**, Representative micrograph of the HBB complex. **b**, Selected 2D class averages used for 3D reconstruction of the LP ring with C26 symmetry. **c**, The local resolution of the final C26 LP ring density map colored from red (4.7 Å) to blue (2.6 Å). **d**, FSCs of the final density map of the LP ring reconstructed with C26 symmetry (upper) and the HBB complex with C1 symmetry (lower).

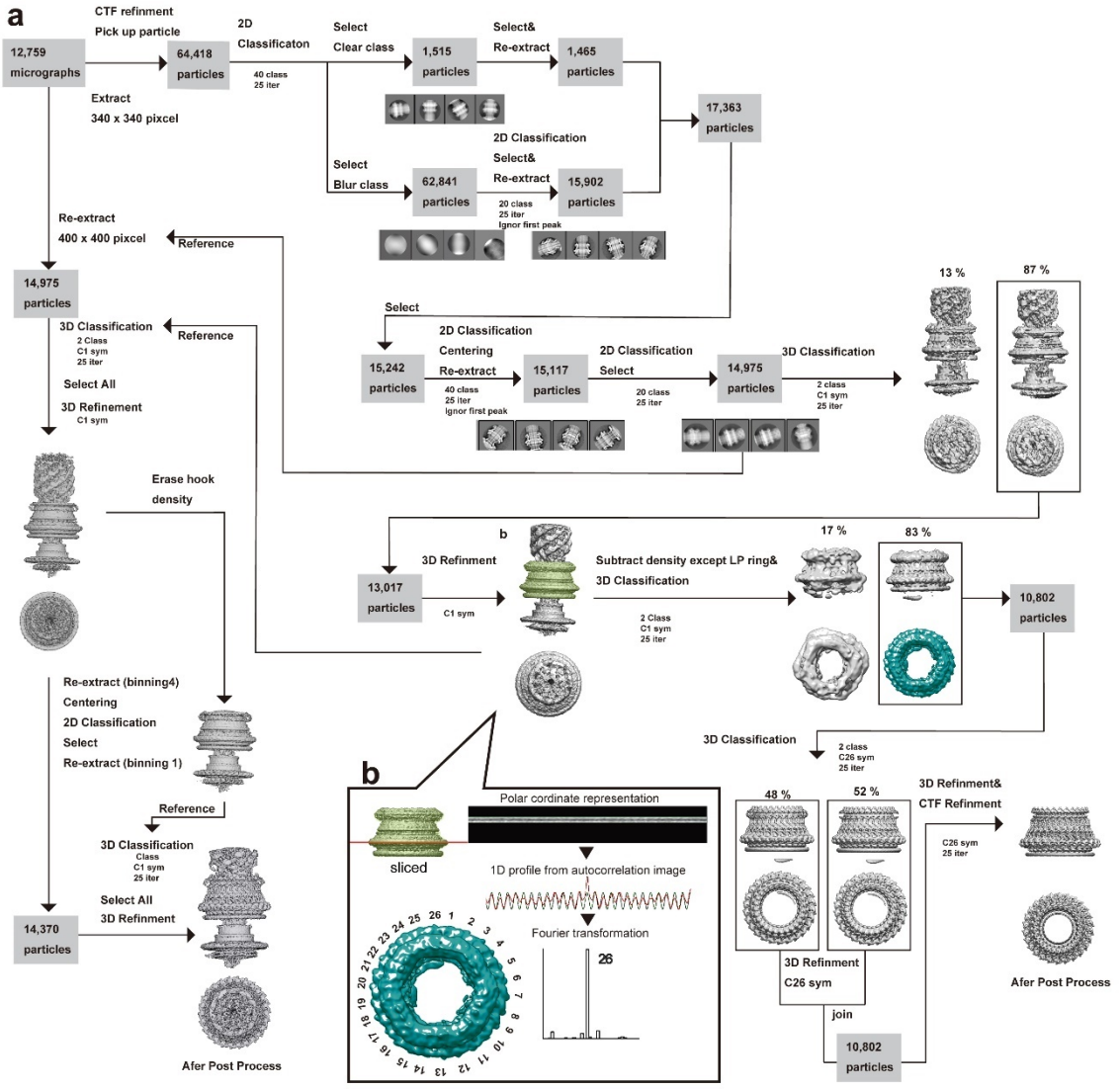

Figure 17 Work process of cryoEM 3D reconstruction of the HBB complex and LP ring. a, The work process of cryoEM single particle structural analysis of the HBB complex, in which 14,370 particles were used for final 3D classification and 3D refinement to produce a HBB density map at 6.9 Å resolution, and that of the LP ring alone, in which 10,802 particles were used to produce a density map at 3.5 Å resolution. **b**, The LP ring density colored light green was used to analyze its rotational symmetry. A horizontal slice of the LP ring density map at the red line was converted into the polar coordinate, and its auto-correlation was calculated and Fourier transformed to confirm the C26 symmetry indicated by visual inspection of the top view of the LP ring (green) extracted from the HBB complex reconstructed with C1 symmetry.

Table 7 Conditions of cryoEM grid

Sample	**HBB**
Grid	Quantifoil holey carbon grid R1.2/1.3 Mo 200 mesh
Glow discharge (s)	10 sec, one side of grid
Buffer	20 mM Tris-HCl, pH 8.0, 150 mM NaCl, 0.05% (w/v) Triton X-100
Vitrobot Mark IV	
Humidity (%)	100
Temperature (°C)	4
Amount of sample solution	3 μL for one side of grid
Blotting time (s)	5
Drain time (s)	1

Sample	**PRP**
Grid	Gold-coated holey carbon grid R1.2/1.3 Cu 200 mesh (Quantifoil)
Glow discharge (s)	5 sec, both sides of grid
Buffer	50 mM Tris-HCl, 50 mM NaCl, 25 mM Imidazole, 0.002% (w/v) LMNG, 0.05% (w/v) Triton X-100, pH 8.0
Vitrobot Mark IV	
Humidity (%)	100
Temperature (°C)	4
Amount of sample solution	3.0 μL for both side of grid (1.5 μL per one side)
Blotting time (s)	4
Drain time (s)	1

Table 8 Summary of cryoEM data collection and image analysis for LP ring and HBB

Data collection and processing		
	HBB (EMDB-30409)	LP ring (EMD-30398)
CryoTEM	CRYO ARM 200 (prototype)	CRYO ARM 200 (prototype)
Voltage (kV)	200	200
Camera	K2 Summit	K2 Summit
Magnification	40,000	140,000
Pixel size (Å / pix)	1.45	1.45
Total exposure time (sec)	10	10
No. of frames	50	50
Frame rate (sec / frame)	0.2	0.2
Dose rate par frames (e^- / Å)	0.9	0.9
Defocus range (μm)	0.2–2.0	0.2–2.0
No. of micrographs	12,759	12,759
No. of final particle images	14,370	10,802
Symmetry	C1	C26
Resolution (Å)	6.9	3.5
FSC threshold	0.143	0.143
Root-mean-square deviations		
Bond lengths (Å)	–	0.007
Bond angles (°)	–	1.027
Validation		
MolProbity score	–	1.17
Clashscore	–	3.35
Poor rotamers (%)	–	0.42
Ramachandran plot		
Favored (%)	–	97.82
Allowed (%)	–	2.18
Disallowed (%)	–	0.00

The polyrod-P ring complex and P ring

A 3 µL aliquot of the sample solution was applied to a gold coated holey carbon grid R1.2/1.3 Mo 200 mesh (Quantifoil Micro Tools GmbH, Großlöbichau, Germany) with pretreatment by glow discharge (both sides of grid). The samples were applied from both side of grid, and the grids were blotted and plunged into liquid ethane at the temperature of liquid nitrogen for rapid freezing[36] with Vitrobot Mark IV (Thermo Fisher Scientific) with a blotting time of 4 seconds at 4°C and 100% humidity with 1 seconds drain time (Table 7). Grids were then transferred into electron cryomicroscope with a cryostage cooled by liquid nitrogen.

The data collection of the PRP was operated on a prototype of CRYO ARM 300 (JEOL, Japan) equipped with a cold field-emission electron gun operated accelerating voltage of 300 kV, an Ω-type energy filter with a 20 eV slit width and a K3 direct electron detector camera (Gatan, USA). The 28,712 dose-fractionated movies were automatically collected using the SerialEM software[80] (Figure 18a). Using a minimum dose system, two data sets were taken by different conditions; One date set was taken by exposure of 6 seconds, a frame rate of 0.08 sec/frame, an electron dose of 1.0 electrons/Å^2 per frame. The other was taken by exposure of 2.5 seconds, a frame rate of 0.0625 sec/frame, an electron dose of 1.0 electrons/Å^2 per frame. All data were taken with defocus range of 0.2 to 2.0 µm, and a nominal magnification of 50,000×, corresponding to an image pixel size of 1.00 Å. All of the 75 or 40 frames of the movie were used for the further analysis. The motion correction and defocus of each image were estimated by cryoSPAC[81,82].In total, 386,473 particles were picked up by using cryoSPARC template-based Automatic Particle Picking program and extracted into a box of 400 × 400 pixels and used for 2D classification by cryoSPARC. For P ring analysis, the 88,969 particles were selected after 2D classification, and those particles were used for Homogeneous refinement with C26 symmetry for 3D reconstruction. The mask only covers P ring were used for the 3D reconstruction. In order to improve the map resolution, the reconstructed density map and segmented particle images analyzed by cryoSPARC were imported to RELION 3.1.1. For those imported particles, the CTF was estimated and 3D refinement was done by RELION 3.1.1. Finally, the 2.5 Å resolution map of P ring was reconstructed from 85,463 particles. For the analysis of the PRP complex, the 101,601 particles were selected after 2D classification by cryoSPARC, and those particles were used for 3D classification an 3D refinement by RELION 3.1.1 with C1 symmetry. After CTF estimation and 3D refinement, the 3.6 Å resolution map of PRP was reconstructed from 85,119 particles (Figure 19). The summary of cryoEM data collection and statistics is shown in Table 9.

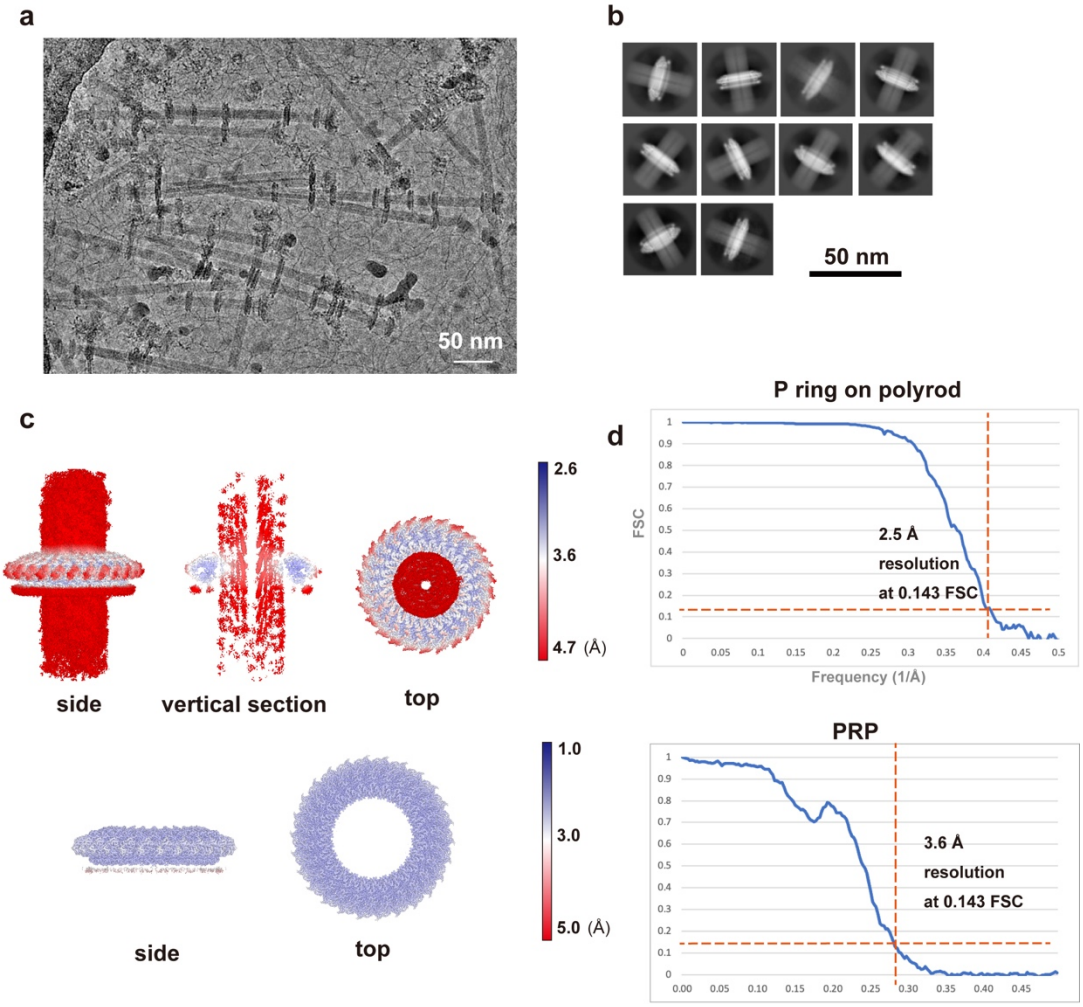

Figure 18 CryoEM single particle image analysis of the PRP and P ring. a, Representative micrograph of the PRP complex. **b**, Selected 2D class averages used for 3D reconstruction of the P ring with C26 symmetry. **c**, The local resolution of the final density map of PRP with C1 symmetry and P ring with C26 symmetry colored with red (4.7 or 5.0 Å) to blue (2.6 or 1.0 Å). **d**, FSCs of the final density map of the P ring reconstructed with C26 symmetry (upper) and the PRP complex with C1 symmetry (lower).

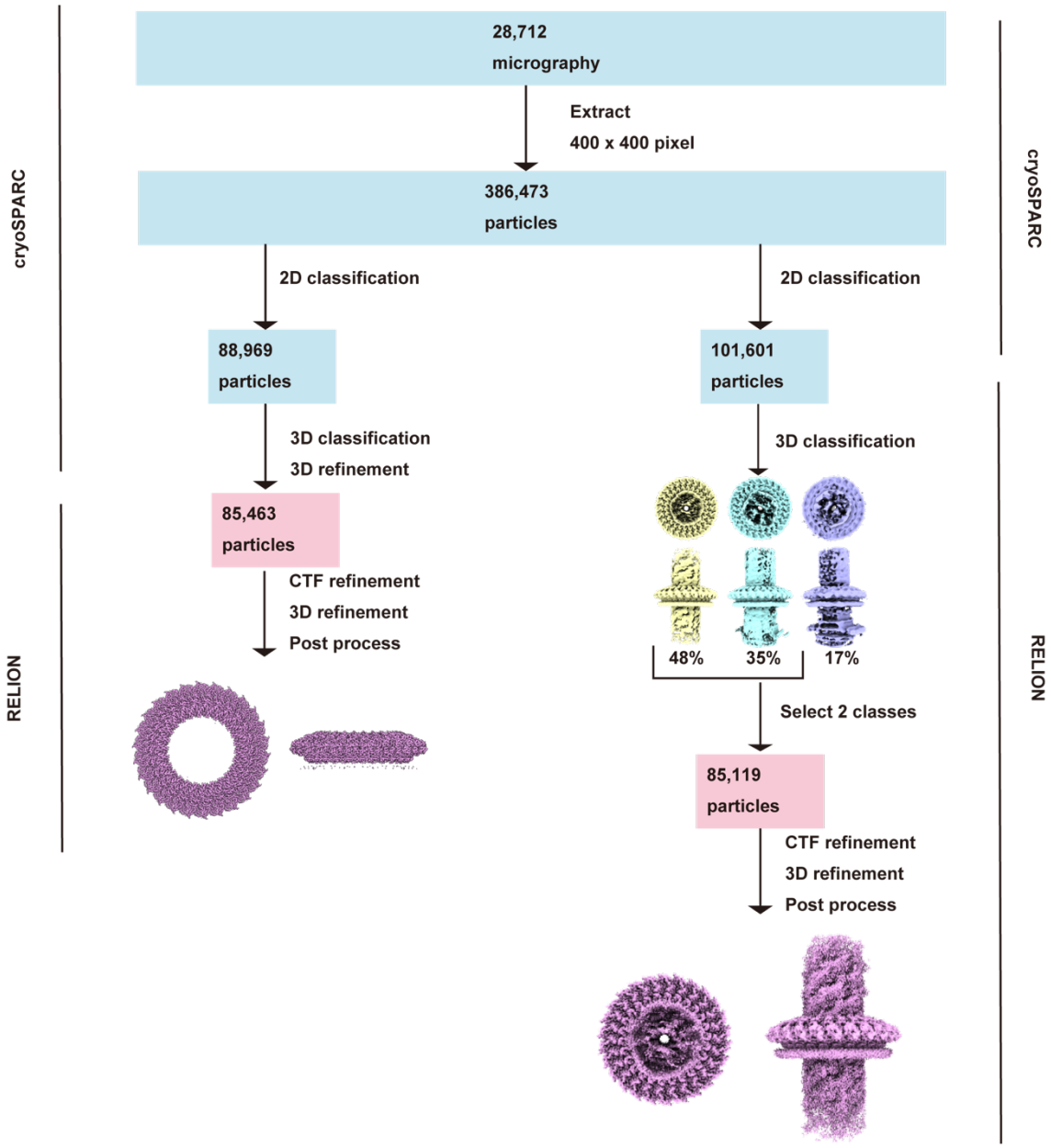

Figure 19 Work process of cryoEM 3D reconstruction of the PRP complex and P ring. a, 85,463 particles were used for final 3D classification and 3D refinement to produce a P ring density map at 2.5 Å resolution, and that of the PRP complex, in which 85,119 particles were used to produce a density map at 3.6 Å resolution. CryoSPARC and RELION programs were used for this analysis.

Table 9 Summary of cryoEM data collection and image analysis for polyrod with P rings

Data collection and processing		
	PRP	P ring
CryoTEM	CRYO ARM 300	CRYO ARM 300
Voltage (kV)	300	300
Camera	K3	K3
Magnification	50,000	50,000
Pixel size (Å / pix)	1.00	1.00
Total exposure time (sec)	6 and 2.5	6 and 2.5
No. of frames	75 and 40	75 and 40
Frame rate (sec / frame)	0.08 and 0.0625	0.08 and 0.0625
Dose rate par frames (e^- / Å)	1.0	1.0
Defocus range (μm)	0.2 – 2.0	0.2 – 2.0
No. of micrographs	28,712	28,712
No. of final particle images	85,119	85,463
Symmetry	C1	C26
Resolution (Å)	3.57	2.48
FSC threshold	0.143	0.143
Root-mean-square deviations		
Bond lengths (Å)	–	0.007
Bond angles (°)	–	1.184
Validation		
MolProbity score	–	1.20
Clash score	–	2.23
Poor rotamers (%)	–	0.78
Ramachandran plot		
Favored (%)	–	97.31
Allowed (%)	–	2.68
Disallowed (%)	–	0.01

Model building

The atomic model of FlgH and FlgI in LP ring were constructed by Coot[41], and PHENIX[45] was used for auto sharpening of the cryoEM maps and real-space refinement. The secondary structures of FlgH and FlgI were predicted by PSIPRED[83]. In order to identify the minimum units composing L ring and P ring, only the Cα atoms were placed on the cryoEM map by Coot to make the main chain model of FlgH and FlgI. For further refinement, the densities around 4 Å from the Cα atoms were extracted from the LP ring density map, and the model was automatically refined by PHENIX real-space refinement and manually fixed by Coot. The side chains were added manually by Coot based on the cryoEM map and PSIPRED prediction. In order to consider the interactions between adjacent molecules, seven FlgH and three FlgI molecules were used for further refinement, and the central models of FlgH and FlgI were extracted to be the final model. The entire LP ring model was made by UCSF Chimera[40] using the C26 symmetry. The P ring on polyrod were modified by Coot and PHENIX based on the atomic model of P ring in HBB. The surface potential was calculated by APBS[84] and PDB2PQR[85] and multiple sequence was aligned by Clustal Omega v1.2.4[43] for visualizing the conservation rate.

Results

Structure of the LP ring around the rod

The HBB was purified from the *Salmonella* HK1002 cells (see Methods of Chapter B) that do not form the flagellar filament. CryoEM images were collected and analyzed by single particle image analysis using RELION[38], and the LP ring structure in the HBB was analyzed. The HBB was used for structural analysis instead of purified LP ring itself because the isolated LP ring tend to show a preferred orientation inside the amorphous ice film of quick-frozen grid. First, a 3D image of the HBB was reconstructed at 6.9 Å resolution with C1 symmetry from 13,017 HBB particle images extracted from 12,759 cryoEM movie images (Figure 16. and 17). This density map contains the MS ring, LP ring, rod, and proximal end of the hook. In the first 2D classification, only 1,515 particles were classified as good images and the rest remained in the blurred classes. To collect more particles, another round of 2D classification was carried out for particles in the blurred classes with the "ignore first peak" option in RELION[38], which enabled the collection of additional 15,902 particles. After 3D refinement from 13,017 particles, the C26 symmetry was visible in the P ring density and was confirmed by autocorrelation along the circumference (Figure 17b; see Methods of chapter B). In order to obtain a higher resolution structure of the LP ring, the LP ring part of the HBB image was re-extracted and analyzed with the C26 symmetry, and this produced a 3.5 Å resolution map (EMD-30398). To determine the relative positioning of the rod and LP ring precisely, a 3D image of the HBB was again reconstructed with C1 symmetry from 14,370 HBB particle images extracted with a larger box size from the same data sets, with the 3.5 Å resolution map of the LP ring used as a reference for the refinement, and this produced a 6.9 Å resolution density map (EMD-30409) with a better quality than the initial HBB map. Although the global resolution of this map was the same as that of the initial one, the local resolution was improved (Figure 17a and 20a; see Methods of chapter B).

The inner and outer diameters of the LP ring are 135 Å and 260 Å, respectively, and its height is 145 Å (Figure 20a). The inner diameter of the LP ring is only slightly larger than the diameter of the distal rod (130 Å). There is an extra, rather blurred ring density beneath the P ring, which is likely part of FlgI (Figure 20b). The atomic models of FlgH and FlgI were built based on the density map (Figure 20 cd, PDB ID: 7CLR).

The position of the LP ring around the rod was determined by superimposing the 3.5 Å resolution LP ring map on the 6.9 Å resolution HBB map (Figure 21).

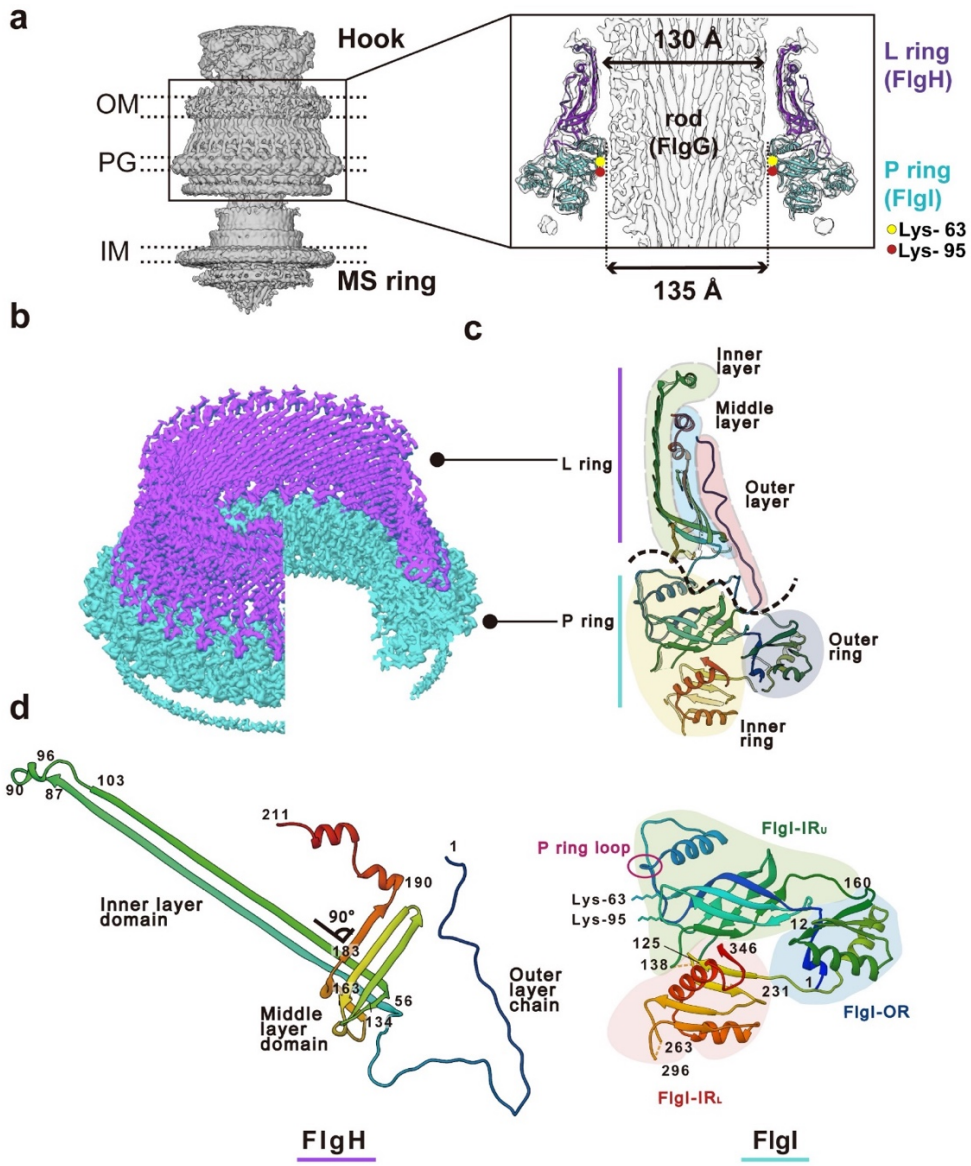

Figure 20 Density map and atomic model of the LP ring. a, Side view of the density map of the HBB complex (EMD-30409) without applying any symmetry (C1). OM, PG, IM refers to the outer membrane, PG layer and inner membrane, respectively. A vertical slice of the LP ring and rod is shown enlarged on the right. The atomic models of the L ring (purple) and the P ring (cyan) are superimposed to the density map. The yellow and red circles indicate the positions of Lys-63 and Lys-95 of FlgI. **b**, the density maps of the L ring (purple) and the P ring (cyan) after applying C26 symmetry (EMD-30398). **c**, The atomic models of FlgH and FlgI in Cα ribbon representation in a vertical slice of the LP ring. The L ring has a three-layered structure (inner layer, light green; middle layer, cyan; outer layer, pink), and the P ring has a two-layered structure (inner ring, light-yellow; outer ring, blue). **d**, The atomic models of FlgH and FlgI (PDB ID: 7CLR) in Cα ribbon representation. FlgH is constituted from three parts: the inner layer domain; the middle layer domain; and the outer layer chain. FlgI is constituted from three domains: FlgI-OR (cyan); FlgI-IR_U (light green); and FlgI-IR_L (pink). Lys-63, Lys-95 and the P ring loop are located within the FlgI-IR_U domain.

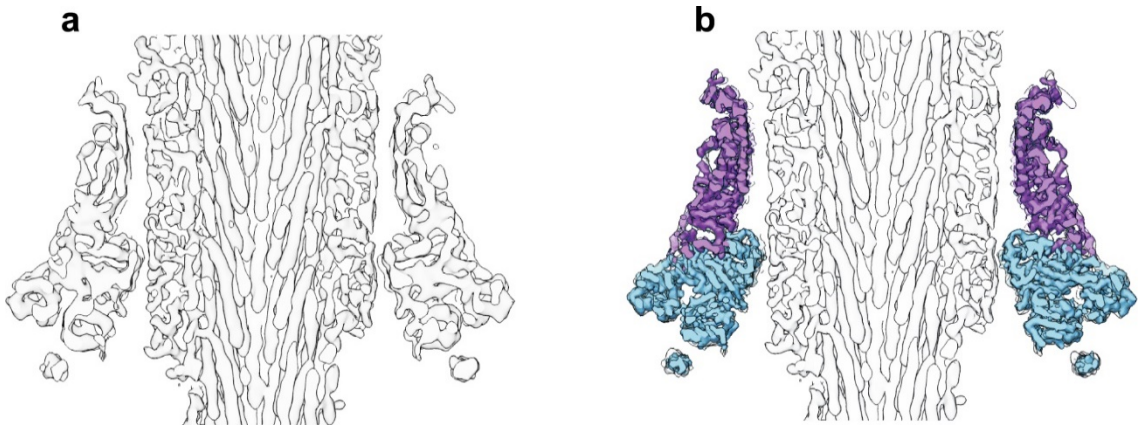

Figure 21 The LP ring position relative to the rod determined from the HBB complex density map. a, Vertical slice of the HBB complex density map (C1) including the LP ring and distal rod reconstructed at 6.9 Å resolution. **b**, The LP ring density map at 3.5 Å resolution (C26) is superimposed on the figure in **a**.

Structure of FlgH

FlgH forms the L ring and FlgI forms the P ring more or less exclusively (Figure 20abc). The atomic model of FlgH forming the L ring contains the whole 211 residues of FlgH. The L ring adopts a three-layer cylinder structure composed of two β-barrel layers and the outermost layer with an extended chain (Figure 20cd, and 22). Two very long anti-parallel β strands, a short β strand and a short α helix make the inner layer domain, four anti-parallel β strands and two short α helices make the middle layer domain, and the N-terminal extended chain (outer layer chain) covers these two layers to form the outer layer. The anti-parallel β strands of the inner and middle layer domains are crossing nearly perpendicular to each other (Figure 20d), forming a hydrophobic core with conserved residues (Figure 22ac), and 26 copies of them form two layers of cylindrical β sheets in the inner and middle layers, respectively (Figure 20c). The extended chain of FlgH in the outer layer of the L ring is predicted to be disordered (Figure 22b) and is presumably disordered in the monomeric form until it assembles into the L ring. The N-terminal Cys residue of FlgH, Csy-22, is postulated to be acylated with palmitate or other available long-chain fatty acids[69]. This is demonstrated by recent cryoEM single particle analysis[72]. However, such an electron density was not observed in my study, presumably because of the difference in sample purification (Tan *et al*. used LDAO instead of Triton X-100 as a detergent for sample purification) or I could not detect it because of the lower resolution of this residue. However, around the Cys-22, there are blurred densities that could be detergent, suggesting that those residues interact with lipids bilayers. The other research group observed additional densities around the L ring, which is a lipidated outer membrane protein, YecR, by cryoEM structural analysis and suggested that YecR regulates the remodeling of lipids around the unusual L ring structure[86]. Those density was not observed in either my study or the Tan *et al*. study, possibly suggesting that YecR may dissociate from the L ring by a high pH treatment (more than 10.5) during the sample purification.

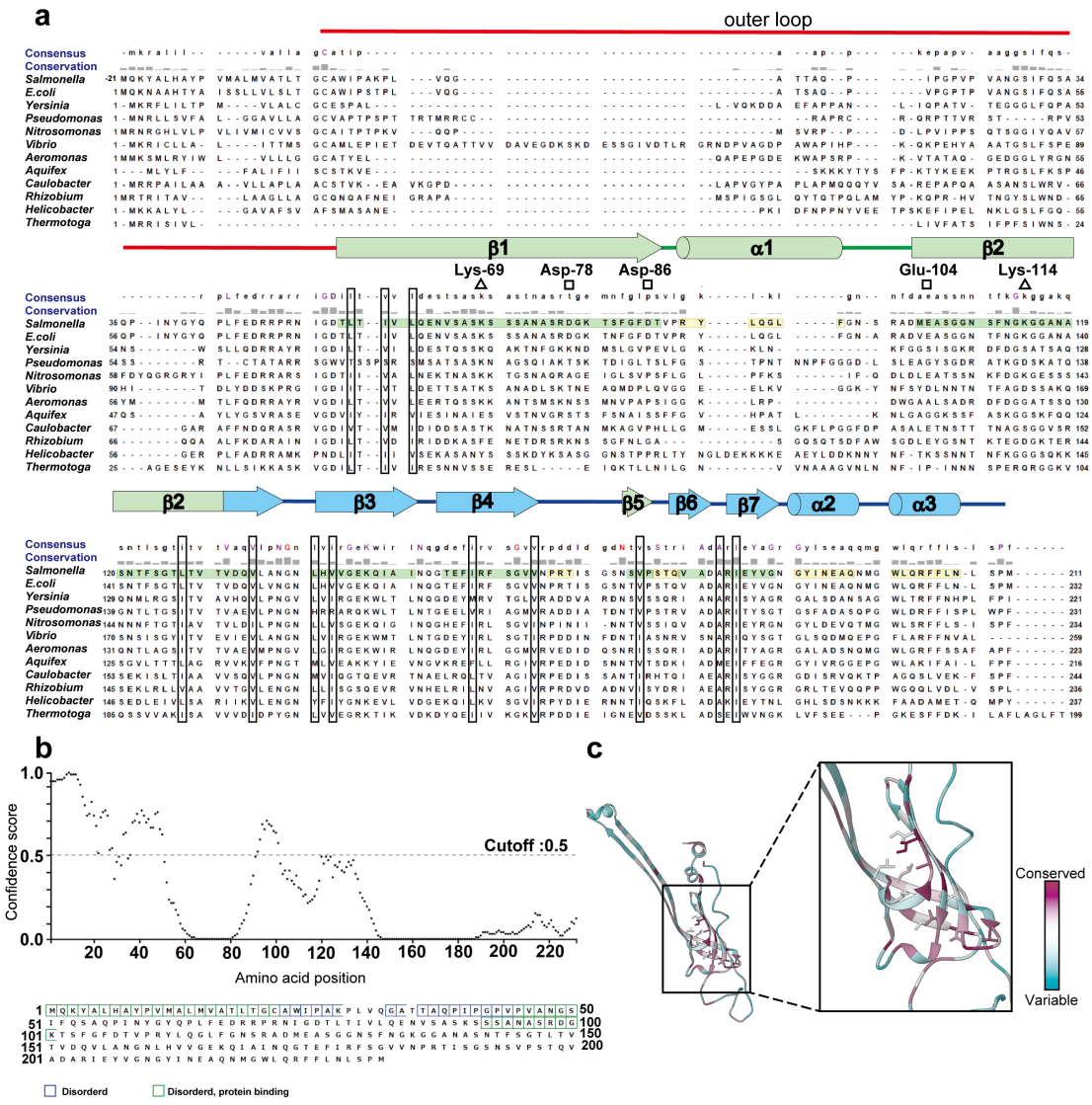

Figure 22 Multiple sequence alignment of FlgH. a, Multiple sequence alignment of FlgH carried out by Clustal Omega[43]. UniProt Accession numbers: *Salmonella* (*S. enterica* serovar Typhimurium), P0A1N8; *E. coli*, P0A6S0; *Yersinia* (*Y. pestis*), Q8ZHZ5; *Pseudomonas* (*P. putida*), Q52081; *Nitrosomonas* (*N. europaea*), Q82XG6; *Vibrio* (*V. parahaemolyticus*), Q9X9J5; *Aeromonas* (*A. hydrophila*), A0A142DZW5; *Aquifex* (*A. aeolicus*), O67609; *Caulobacter* (*C. vibrioides*), A0A0H3C9Y8; *Rhizobium* (*R. meliloti*), A0A222JND2; *Helicobacter* (*H. pylori*), E8QV65; *Thermotoga* (*T. maritima*), Q9X1M6. The five charged residues (Lys-69, Asp-78, Asp-86, Glu-104, Lys-114) and color-coded secondary structures of *Salmonella* FlgH in three domains (outer layer, red; inner layer, light green; middle layer, cyan) are shown above the sequence. **b**, Prediction of disordered regions by PSIPRED[83]. The disorder plot (upper) and predicted disordered regions (lower) agree with the outer layer chain of our atomic model. **c**, The sequence conservation of FlgH is colored from cyan to magenta (range of 0–100%), calculated and visualized by Chimera[40]. Side chains involved in intramolecular hydrophobic interactions are shown in stick representation and magnified (right), and these hydrophobic residues are also boxed in **a**.

Structure of FlgI

The atomic model of FlgI contains residues 1–125, 138–263 and 296–346, which cover 87% of the entire FlgI sequence. The atomic model of residues 126–137 and 264–295 of FlgI could not be constructed due to their poor densities in cryoEM map (Figure 20d and 23). It is composed of three domains, which were named FlgI-IR_U (upper inner ring), FlgI-IR_L (lower inner ring) and FlgI-OR (outer ring). FlgI-OR (residues 1–11 and 160–230) is composed of three α helices and four β strands and forms the outer rim of the P ring. FlgI-IR_U (residues 12–159) is composed of one α helix and 10 β strands, FlgI-IR_L (residues 231–346) is composed of two α helices and five β strands, and these two domains form the inner part of the P ring. FlgI-IR_U forms a β-barrel-like structure with highly conserved residues forming a hydrophobic core (Figure 20d and 23ab) and also contains a loop of four polar residues from Thr-33 through Thr-36 (P ring loop in Figure 20d). This loop and two highly conserved positively charged residues of FlgI-IR_U, Lys-63 and Lys-95, are in very close proximity to the rod surface (Figure 20a), suggesting their involvement in P ring assembly around the rod as well as in the function as a bushing. FlgI-IR_L is formed by the C-terminal chain of FlgI and contains a highly flexible loop (residues 264–295) that is likely to form the extra ring density beneath the P ring (Figure 20b and 23a).

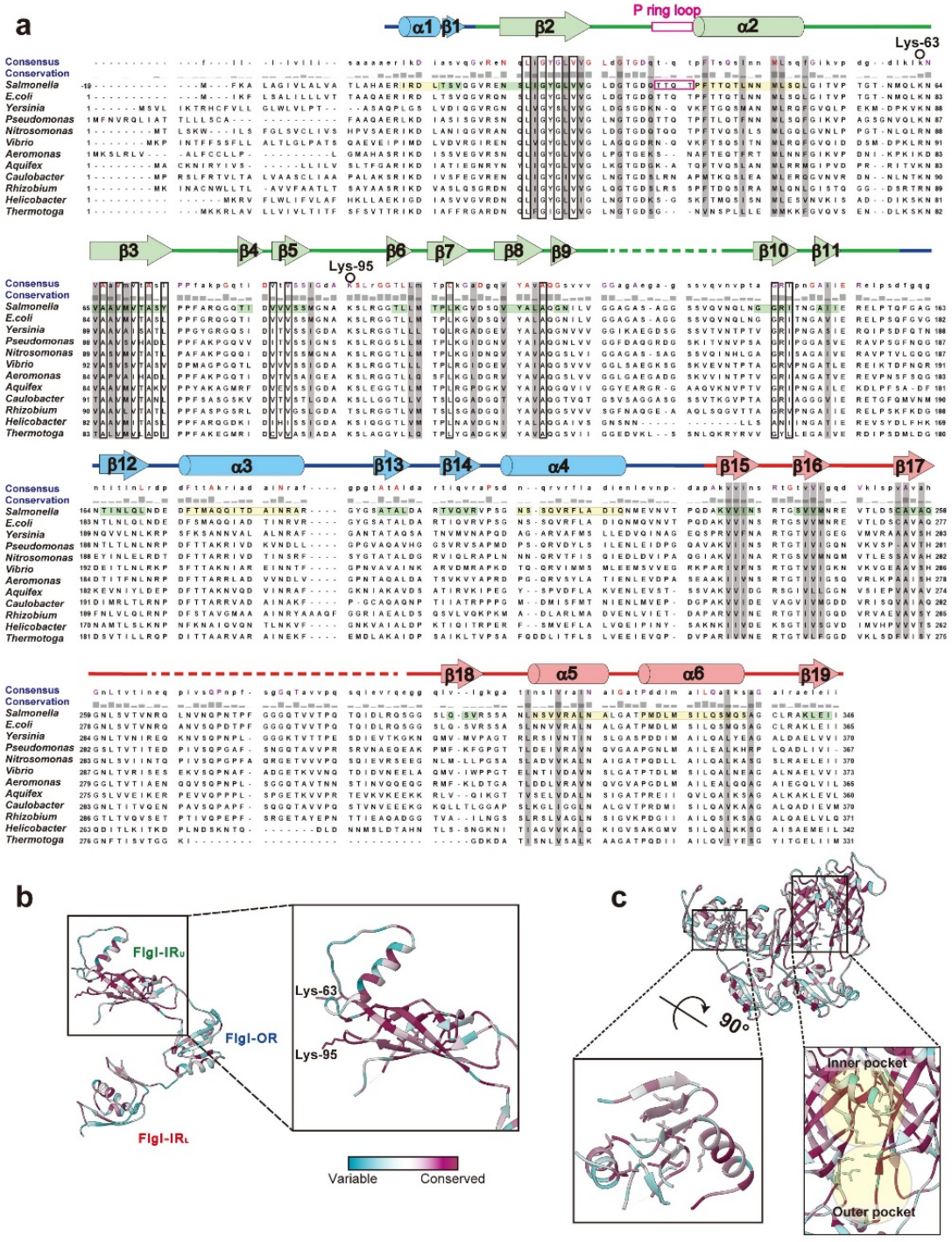
a
P ring loop
α1
β1
β2
α2
Lys-63
β3
β4
β5
Lys-95
β6
β7
β8
β9
β10
β11
β12
α3
β13
β14
α4
β15
β16
β17
β18
α5
α6
β19
Consensus
Conservation
Salmonella
E.coli
Yersinia
Pseudomonas
Nitrosomonas
Vibrio
Aeromonas
Aquifex
Caulobacter
Rhizobium
Helicobacter
Thermotoga
b
FlgI-IRU
FlgI-OR
FlgI-IRL
Lys-63
Lys-95
Variable
Conserved
c
90°
Inner pocket
Outer pocket

Figure 23 Multiple sequence alignment for FlgI. **a**, Multiple sequence alignment of FlgI carried out by Clustal Omega[43]. UniProt Accession numbers: *Salmonella* (*S. enterica* serovar Typhimurium), P15930; *E. coli*, P0A6S3; *Yersinia* (*Y. pestis*), Q8ZHZ4; *Pseudomonas* (*P. putida*), Q52082; *Nitrosomonas* (*N. europaea*), Q82XG5; *Vibrio* (*V. parahaemolyticus*), Q87JI2; *Aeromonas* (*A. hydrophila*), A0KM38; *Aquifex* (*A. aeolicus*), O67608; *Caulobacter* (*C. vibrioides*), P33979; *Rhizobium* (*R. meliloti*), Q52948; *Helicobacter* (*H. pylori*), O25028; *Thermotoga* (*T. maritima*), Q9X1M5. The two charged residues (Lys-63, Lys-95) and color-coded secondary structures of *Salmonella* FlgI with three domains (FlgI-OR, cyan; FlgI-IR_U, light green; FlgI-IR_L, red) are shown above the sequence. **b, c,** The sequence conservation of FlgI is colored from cyan to magenta (range of 0-100%), calculated and visualized by Chimera[40]. Side chains of Lys-63, Lys-95 and those involved in intra and intermolecular hydrophobic interactions are shown in stick representation and magnified in b and c, respectively, and these hydrophobic residues are also boxed and grey meshed in a, respectively.

The flagellum and injectisome are both classified as the type III secretion system, but FlgH and FlgI are not homologous to the components of injectisomes[87], such as InvG of the type III secretion system[88], as well as those of other secretion systems: GspD of the type II secretion system[89], and PilQ of the type IVa pilus[90]. However, all these proteins have similar cylindrical β barrel structures, except that the long β strands of FlgH shows different orientation (Figure 24). The structure of FlgI-OR looks similar to that of the N3 domain of GspD[89] (residues 232–267, 288–323), the N3 domain of InvG[88] (residues 176–227, 252–302), the N3 domain of PilQ[90] (residues 251–321), and the C-terminal domain of MotY[91] (residues 155–202, 210–243, 262–271), which shows an extensive similarity to the PG binding domain of OmpA family proteins interacting with the PG layer (Figure 24 and 25; analyzed by MATRAS[92]), suggesting the direct interaction of FlgI-OR with the PG layer. Because the LP ring is required for efficient transport of hook and filament proteins into the culture media, it also functions as a secretion-like pore-forming annulus in addition to that as a molecular bushing. Thus, the structural and functional similarities of these proteins are probably the result of convergent evolution from different origins.

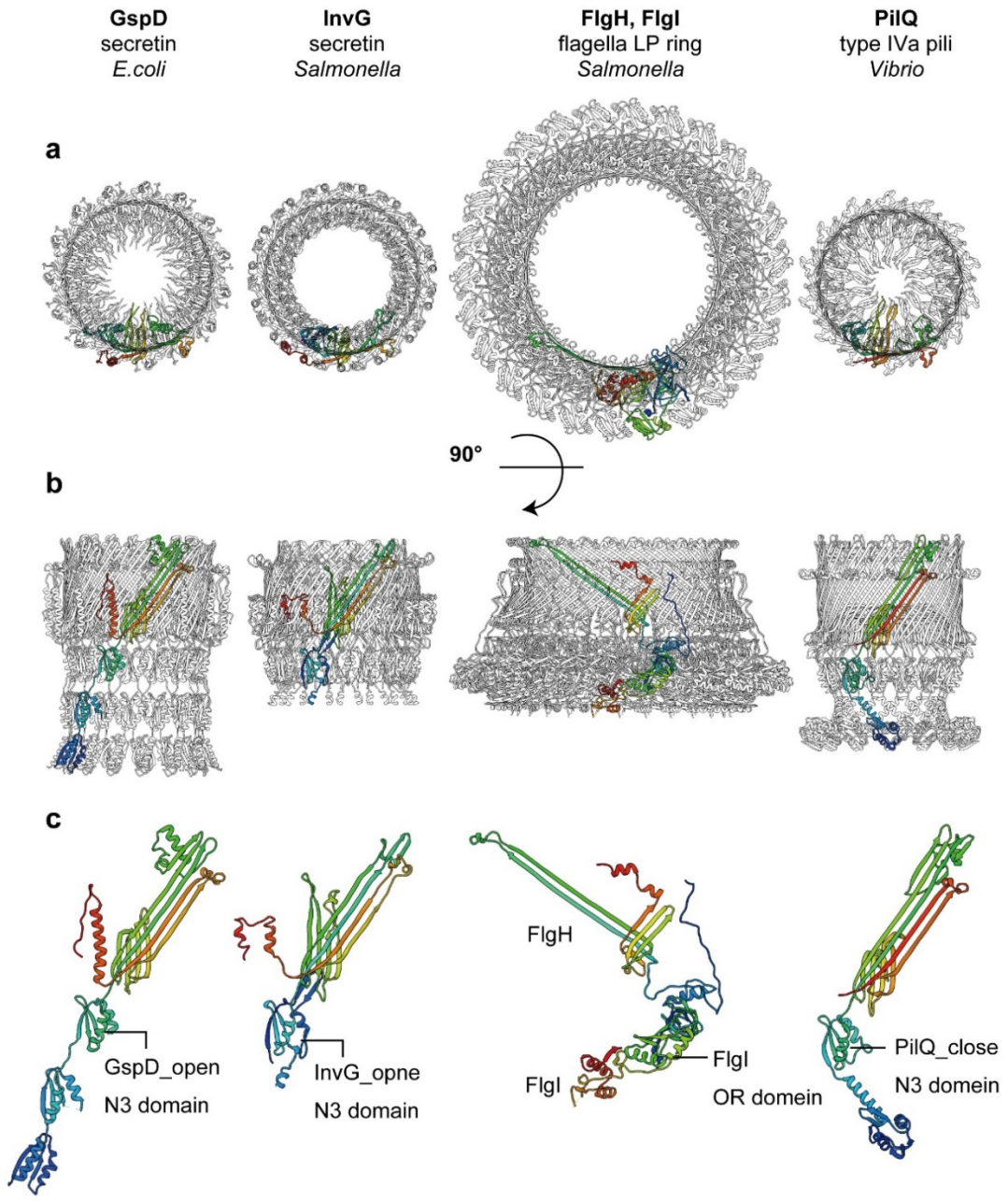

Figure 24 Structural comparison between the LP ring and rings of other secretion systems. a, **b**, Top and side views of GspD_open (residues 99–617, PDB ID: 5WQ7), InvG_open (residues 176–227, 252–557, PDB ID: 6DV6), the LP ring (PDB ID: 7CLR) and PilQ of type IVa pili (residues 160–571, PDB ID: 6W6M). **c,** Side view of each monomer were colored rainbow.

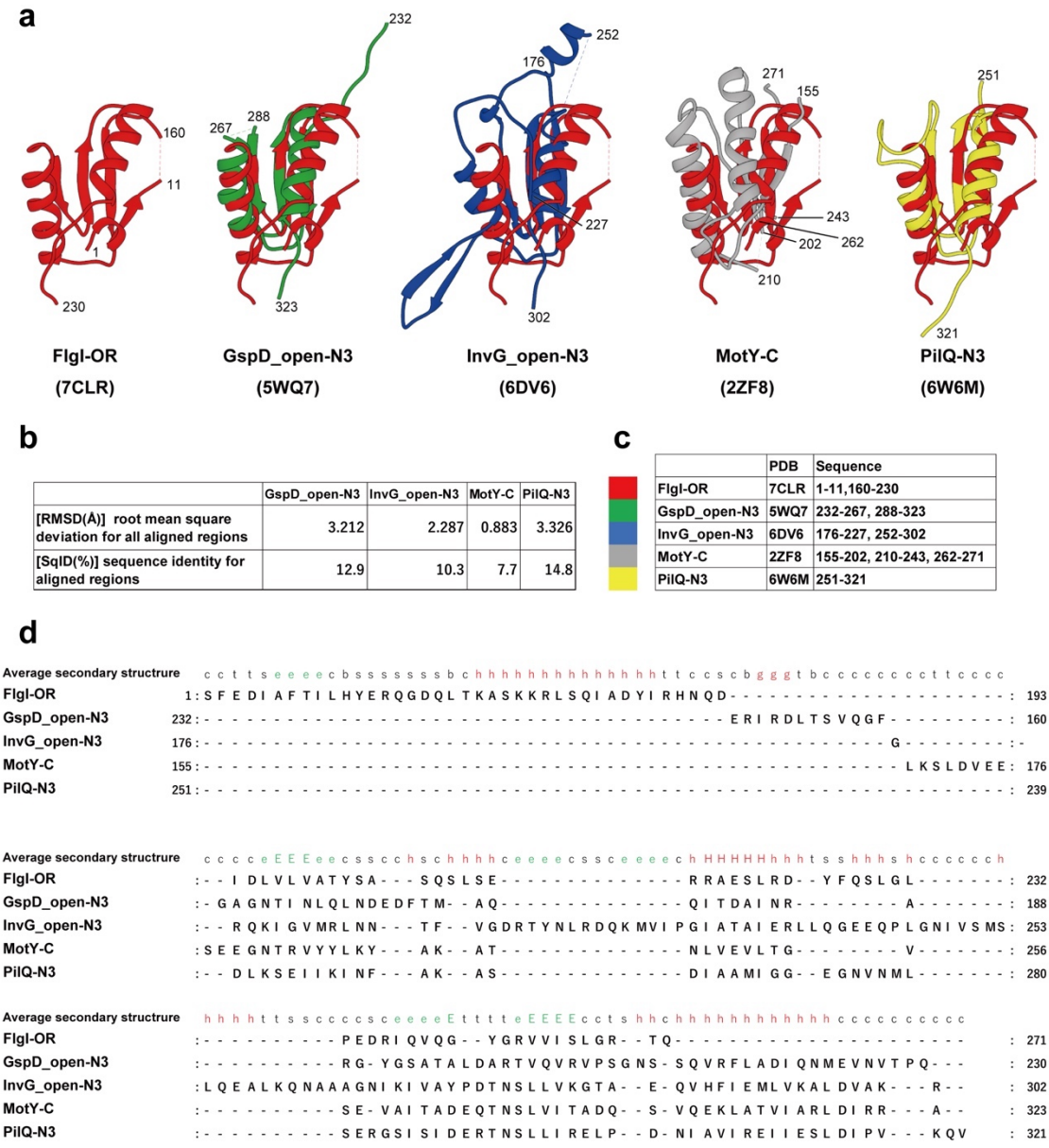

	GspD_open-N3	InvG_open-N3	MotY-C	PilQ-N3
[RMSD(Å)] root mean square deviation for all aligned regions	3.212	2.287	0.883	3.326
[SqID(%)] sequence identity for aligned regions	12.9	10.3	7.7	14.8

	PDB	Sequence
FlgI-OR	7CLR	1-11,160-230
GspD_open-N3	5WQ7	232-267, 288-323
InvG_open-N3	6DV6	176-227, 252-302
MotY-C	2ZF8	155-202, 210-243, 262-271
PilQ-N3	6W6M	251-321

Figure 25 Structural comparison between FlgI-OR and related domains of other secretion systems. a, Superposition of FlgI-OR (residues 1–11, 160–230: red) on to GspD_open-N3 (residues 232–267, 288–323: green), InvG_open-N3 (residues 176–227, 252–302: blue), MotY-C (PDB ID: 2ZF8, residue 155–202, 210–243, 262–271: gray) and PilQ-N3 (residues 251–321: yellow). **b**, Alignment score between FlgI-OR and other four domains. **c**, Color, Name, PDB ID, and sequence region of compared domains. **d**, Sequence alignment between FlgI-OR and other four domains. All the alignment and numbers in the tables were calculated by MATRAS[92].

Inter subunit interactions of FlgH and FlgI in the LP ring

In the L ring structure, each FlgH subunit (H_0) interacts with six adjacent FlgH subunits ($H_{\pm1}$, $H_{\pm2}$ and $H_{\pm3}$) (Figure 26ab), and these intricate intersubunit interactions make the LP ring mechanically stable. In the P ring, each FlgI subunit (I_0) interacts with two adjacent FlgI subunits (I_{-1} and I_{+1}) (Figure 26acd). The FlgI-IR_L domains of subunits I_0 and I_{-1} interact with each other through hydrophobic interactions and also form a short anti-parallel β sheet (Figure 26e). FlgI-IR_U forms two hydrophobic "pockets" namely inner and outer pockets (Figure 26f). The C-terminal half of the outer layer chain of a FlgH subunit (H_0) lies at the bottom of the L ring and interacts with three FlgI subunits (I_0, $I_{\pm1}$) through its interactions with the hydrophobic inner and outer pockets of the P ring (Figure 26g). Leu-44 and Phe-45 of FlgH are in the inner pocket composed of Leu-22, Ile-18, Met-46, Leu-50, Leu-103 and Met-104 of FlgI (Figure 26g left). In the outer pocket, Ile-30 of FlgH interacts with Leu-17 and Leu-156 of FlgI, and Phe-31 of FlgH interacts with Val-110, Val-114 and Leu-117 of FlgI (Figure 26g right). The residues of these hydrophobic interactions, especially those in the inner pocket, are well conserved (Figure 23c and 27).

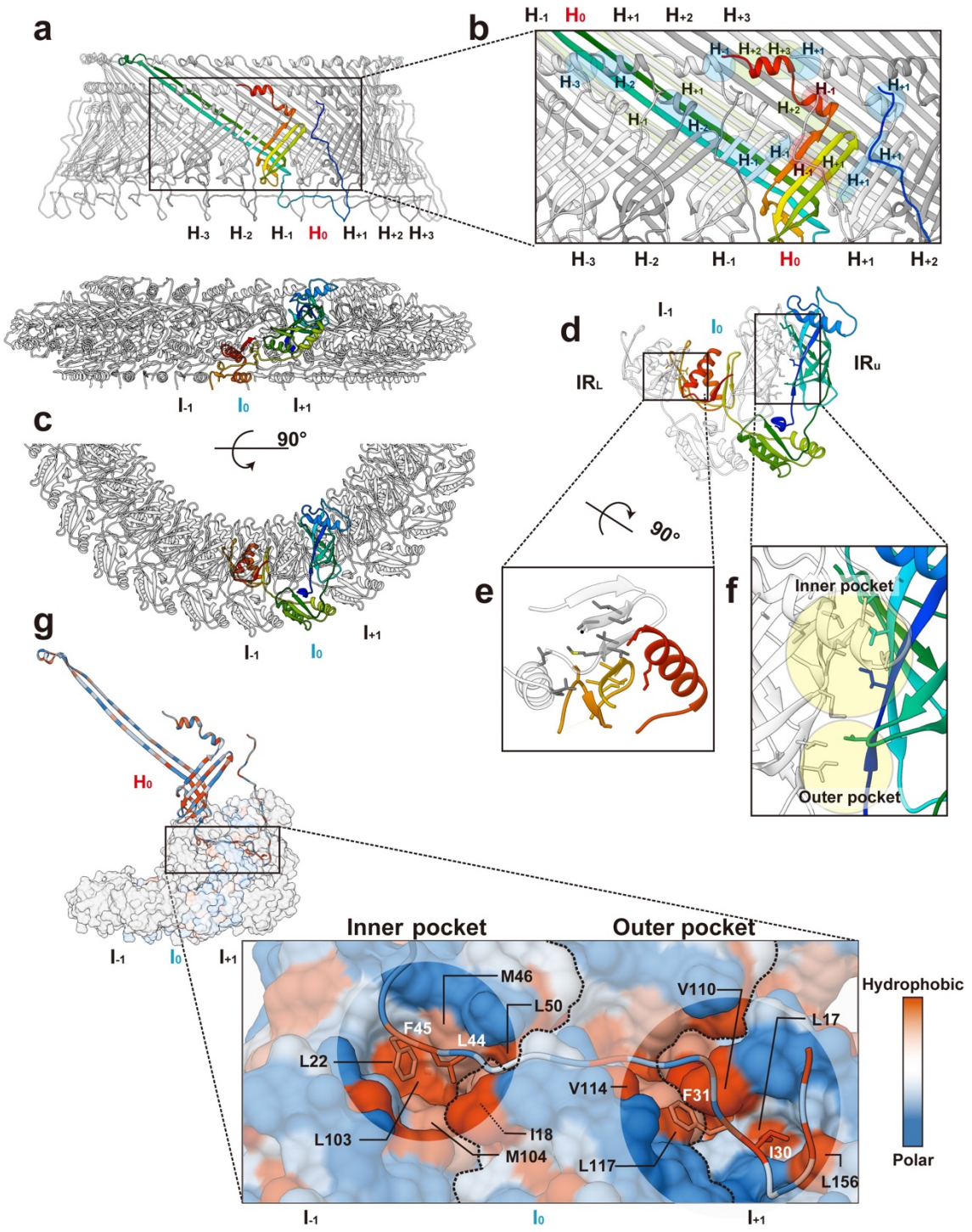
a
b
c
d
e
f
g
H-3 H-2 H-1 H0 H+1 H+2 H+3
I-1 I0 I+1
90°
IRL
IRu
Inner pocket
Outer pocket
M46
L50
F45
L44
L22
L103
I18
M104
V110
L17
V114
F31
I30
L117
L156
Hydrophobic
Polar

Figure 26 Intersubunit interactions of FlgH and FlgI in the LP ring. a, Side view of the L (upper panel) and P (lower panel) rings with one subunit colored rainbow. **b**, Intersubunit interactions between a FlgH subunit (H_0) and its neighboring six FlgH subunits ($H_{\pm1}$, $H_{\pm2}$, $H_{\pm3}$). The segments of six neighboring FlgH subunits interacting with the subunit H_0 are labelled with their subunit ID and colored as: light green, interactions with the inner layer; light blue, interactions with the middle layer; and pink, interactions with the outer layer. **c**, **d**, Top view of the P ring, showing the intersubunit interactions between FlgI (I_0) and its neighboring subunit ($I_{\pm1}$). **e**, Hydrophobic interactions and a short anti-parallel β sheet formed by two neighboring FlgI-IR_L domains. **f**, Two hydrophobic pockets (inner and outer pocket) formed by two neighboring FlgI-IR_U domains. Hydrophobic side chains are displayed in grey sticks in **e** and **f**. **g**, Interactions between FlgH (H_0) and three FlgI (I_0, $I_{\pm1}$) subunits. The extended chain of FlgH in the outer layer form hydrophobic interactions with the inner and outer pockets formed by FlgI subunits. The position of I-18 of FlgI is indicated by a thin dashed line because it is behind Val-110. The boundary lines between FlgI subunits are indicated by thick dashed lines.

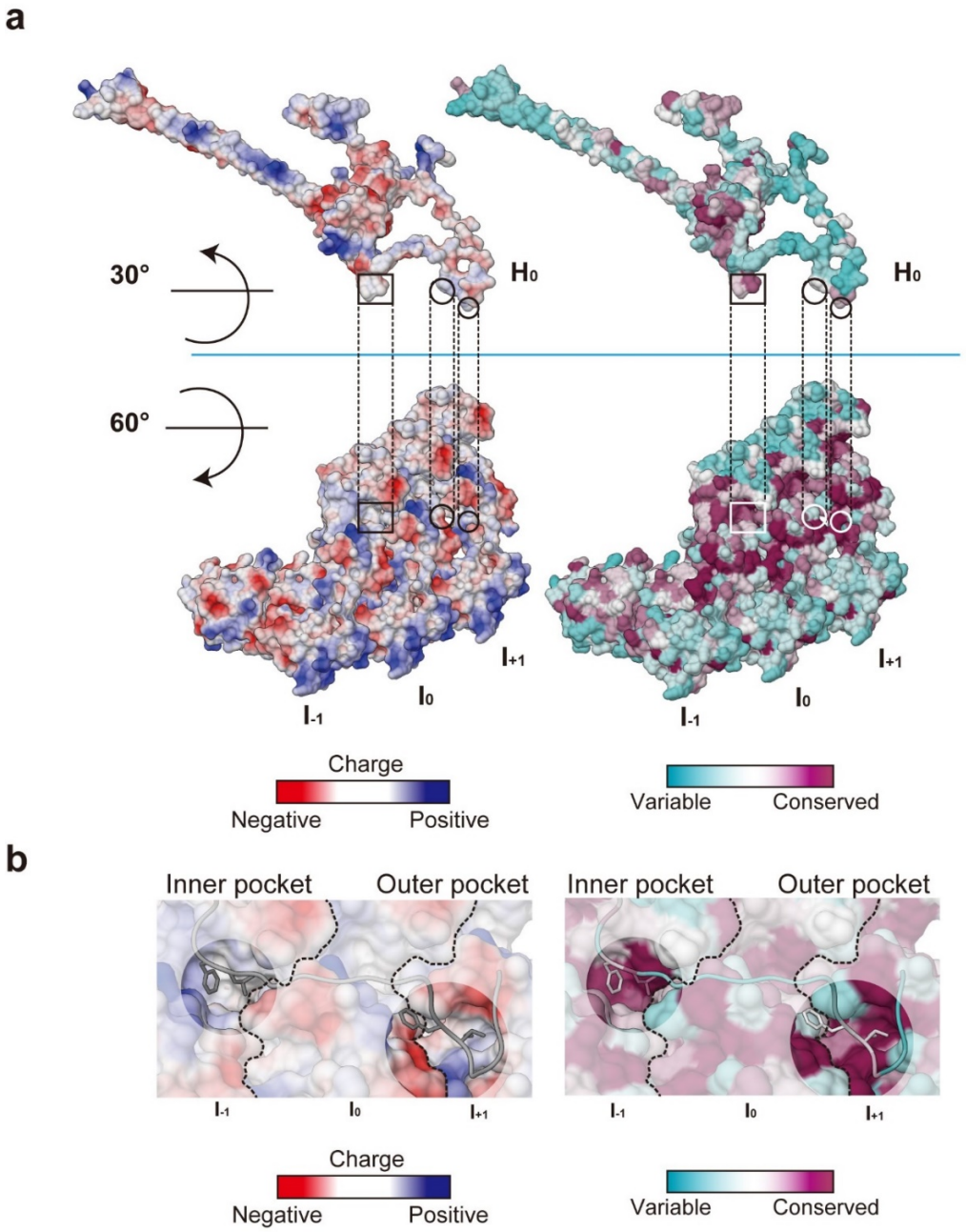

Figure 27 Sequence conservation and electrostatic surface potential of FlgH and FlgI. **a**, Interactions between one FlgH and three FlgI (I_0, $I_{\pm1}$) molecules. The interactions in the inner pocket (□) and outer pocket (○) are both hydrophobic (left), and the residues forming them are mostly highly conserved (right). **b**, Enlarged views of the interactions in the inner pocket and outer pocket. Three FlgI (I_0, $I_{\pm1}$) molecules are displayed as solid surface and FlgH as Cα ribbon. The hydrophobic side chains of FlgH are displayed in stick and are color-coded as gray in the electrostatic surface potential (left) and cyan to magenta in the conservation (right). All figures are made by Chimera[40].

Surface potential and residue conservation of the LP ring and rod

In contrast to the prediction that electrostatic repulsive force by the negative charges on the surfaces of the rod and LP ring may play an important role in the bushing function, the inner surface of the LP ring is charged both negatively and positively. Asp-78, Asp-86 and Glu-104 of FlgH form a negative charge belt, and Lys-69 and Lys-114 of FlgH form a positive charge belt, suggesting that both repulsive and attractive force keep the negatively charged rod rotating at the center of the L ring (Figure 28a). I also found that Lys-63 and Lys-95, which are relatively well conserved among FlgI homologues, form a positive belt on the inner surface of the P ring (Figure 28ab) and these residues are in very close proximity to a negative charge cluster on the rod outer surface (Figure 20a), raising a plausible hypothesis that these two lysine residues are critical for P ring assembly around the rod.

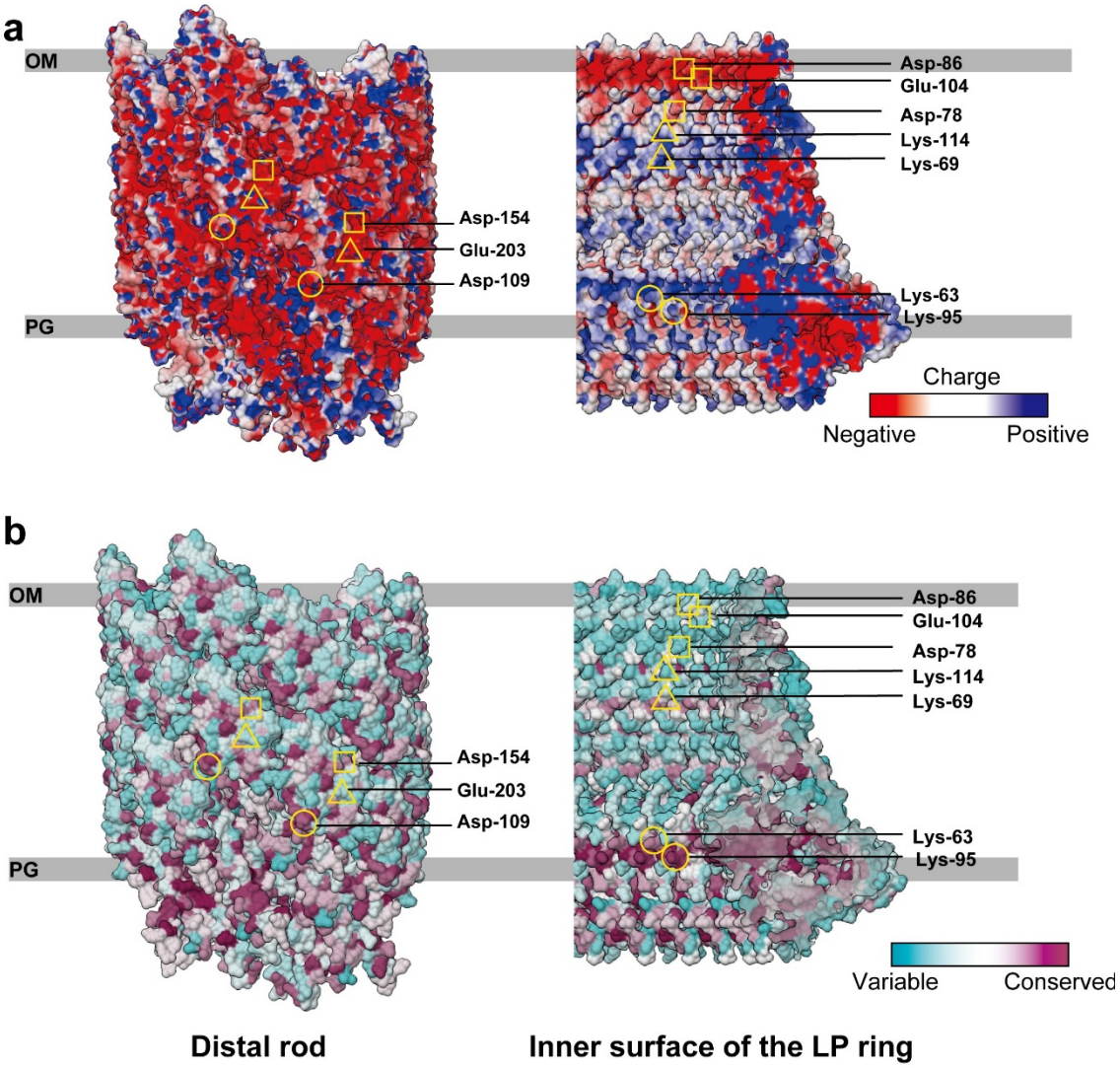

Figure 28 Electrostatic surface potential and sequence conservation of the rod and LP ring. a, Electrostatic potential of the outer surface of the distal rod and the inner surface of the LP ring. The helical arrangement of Asp-109 (○), Asp-154 (□) and Glu-203 (△) of FlgG on the surface of the rod form negatively charged patches. Asp-86, Glu-104 and Asp-78 of FlgH (□) form a negatively charged belt on the inner surface of the L ring. Lys-69 and Lys-114 (△) of FlgH and Lys-63 and Lys-95 (○) of FlgI form positively charged belts on the inner surface of the LP ring. **b,** Conservation of amino acid residues on the outer surface of the distal rod and the inner surface the LP ring. Asp-109 (○) and Aps-154 (□) of the rod and Lys-63 and Lys-95 (○) of the P ring are highly conserved. The sequence conservation is colored from cyan to magenta (range of 0–100%), calculate and visualized by Chimera[40].

To examine whether these positive charges contribute to the P ring assembly, Lys-63 and Lys-95 were replaced with alanine or oppositely charged residue (Asp), and eight *flgI* mutants were constructed; *flgI*(K63A), *flgI*(K63D), *flgI*(K95A), *flgI*(K95D), *flgI*(K63A/K95A), *flgI*(K63A/K95D), *flgI*(K63D/K95A) and *flgI*(K63D/K95D). Those motilities were then analyzed in 0.35% soft agar. A plasmid vector (pET22b, V) and a wild-type plasmid (pTY03, WT) (Table 5) were used as negative and positive controls, respectively. The *flgI*(K63A), *flgI*(K95A) and *flgI*(K95D) mutants formed motility rings although not at the wild-type level (Figure 29a, first row). The *flgI*(K63D) and *flgI*(K63A/K95A) mutants showed a very weak motility phenotype compared to the vector control (Figure 29a, second row). The *flgI*(K63A/K95D), *flgI*(K63D/K95A) and *flgI*(K63D/K95D) mutants exhibited no motility (Figure 29a, third row) but showed some motility after prolonged incubation at 30ºC (Figure 29b). The *flgI*(K63A/K95D), *flgI*(K63D/K95A) and *flgI*(K63D/K95D) mutations affected the protein stability of FlgI, but other mutations did not at all (Figure 29c). The flagellum is necessary for motility, and the disturbance of P ring assembly leads to the inhibition of flagellum formation and no motility. Since the swam size and the number of the filaments were correlated (Figure 29d), these results indicate that the positive charges of Lys-63 and Lys-95 are both critical for FlgI to form the P ring.

The LP ring is required for the secretion of export substrates, such as the hook capping protein FlgD, the hook protein FlgE and the filament protein FliC, into the culture media[93]. In the absence of the LP ring, FlgD and FlgE can cross the cytoplasmic membrane but not the outer membrane, suggesting that the LP ring is required for forming the pore in the outer membrane to expose the distal end of the rod in the cell exterior to allow hook assembly outside the cell body. To test whether these FlgI mutations affect P ring assembly, the secretion levels of FlgE and FliC were analyzed by immunoblotting with polyclonal anti-FlgE and anti-FliC antibodies (Figure 29c). The FlgE and FliC secretion by the *flgI*(K63A) and *flgI*(K95A) mutants were at the wild-type level. Because the swarm plate motility and the number of the flagellar filaments of these two mutants were significantly lower than that of the wild-type ($p < 0.001$ and $p < 0.01$, respectively), the K63A and K95A mutations probably inhibited P ring assembly by neutralizing their positive charges. The FlgE secretion by the *flgI* (K95D) mutant was significantly lower than the wild-type level ($p < 0.01$), suggesting that this mutation also affected P ring

assembly by reversal of its positive charge. The K63D, K63A/K95A, K63A/K95D, K63D/K95A and K63D/K95D mutations considerably reduced the secretion levels, suggesting that these five mutations inhibited P ring formation. Although those five mutations showed no motility after incubation for 8.5 hours (Figure 29a), they showed some motility after incubation for 24 hours (Figure 29b), which is consistent with the very small amounts of FliC and FlgE secretion (Figure 29c). From these results, I propose that electrostatic interactions of Lys-63 and Lys-95 of FlgI with a negative charge cluster on the surface of the rod are essential for efficient P ring formation around the rod.

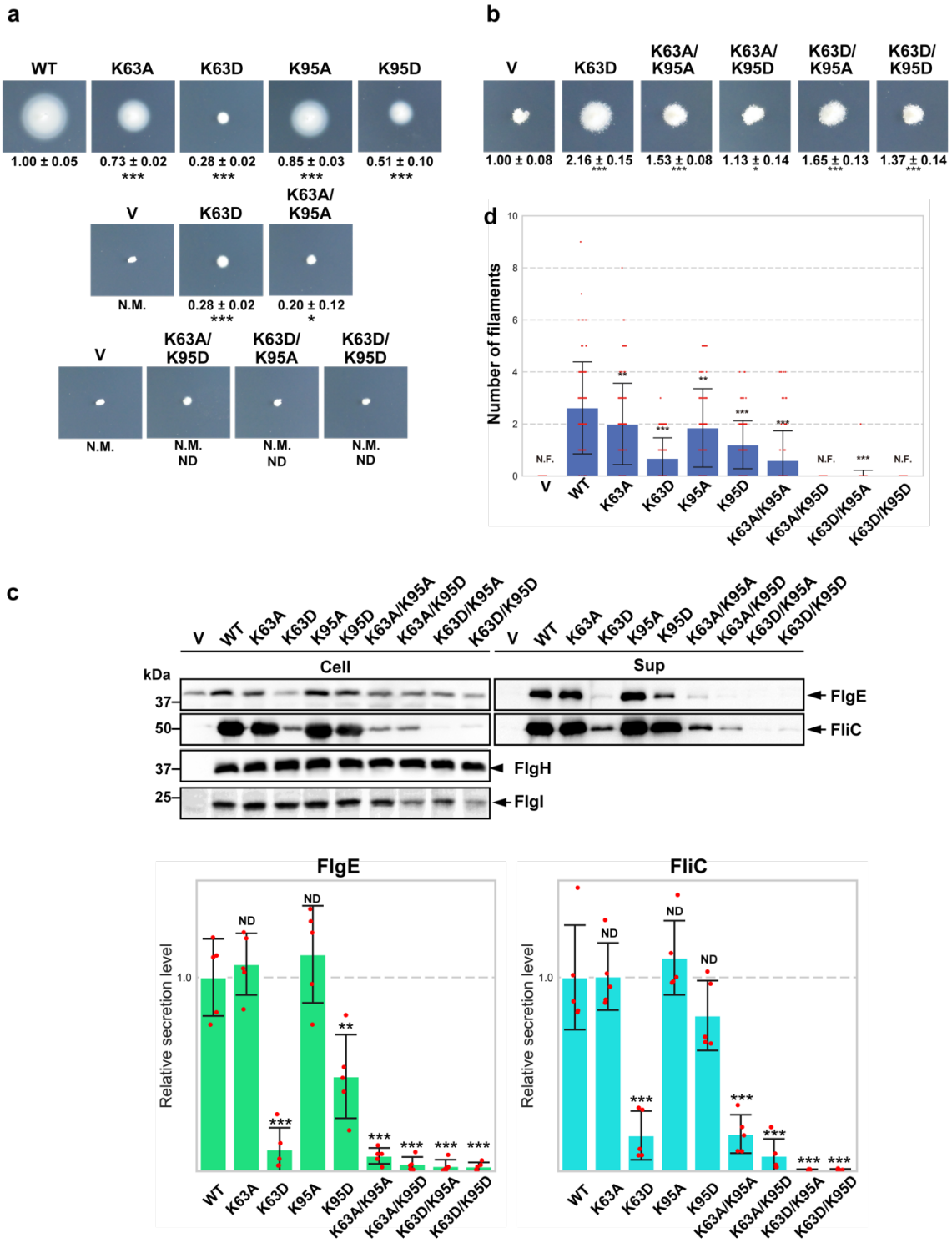
a
WT
K63A
K63D
K95A
K95D
1.00 ± 0.05
0.73 ± 0.02
***
0.28 ± 0.02
***
0.85 ± 0.03
***
0.51 ± 0.10
***
V
K63D
K63A/
K95A
N.M.
0.28 ± 0.02
***
0.20 ± 0.12
*
V
K63A/
K95D
K63D/
K95A
K63D/
K95D
N.M.
N.M.
ND
N.M.
ND
N.M.
ND
b
V
K63D
K63A/
K95A
K63A/
K95D
K63D/
K95A
K63D/
K95D
1.00 ± 0.08
2.16 ± 0.15
***
1.53 ± 0.08
***
1.13 ± 0.14
*
1.65 ± 0.13
***
1.37 ± 0.14
***
d
Number of filaments
N.F.
N.F.
***
N.F.
V
WT
K63A
K63D
K95A
K95D
K63A/K95A
K63A/K95D
K63D/K95A
K63D/K95D
c
kDa
Cell
Sup
37
50
37
25
FlgE
FliC
FlgH
FlgI
FlgE
FliC
Relative secretion level
ND
1.0
WT
K63A
K63D
K95A
K95D
K63A/K95A
K63A/K95D
K63D/K95A
K63D/K95D

Figure 29 *flgI* mutation analysis by motility and secretion assay. a, Motility assay in 0.35% soft agar plate of the *flgI(K63A)*, *flgI(K63D)*, *flgI(K95A)*, *flgI(K95D)*, *flgI(K63A/K95A)*, *flgI(K63A/K95D)*, *flgI(K63D/K95A)* and *flgI(K63D/K95D)* mutants. N.M. indicates non-motile. The diameter of the motility ring of five colonies of each strain was measured after incubating 8.5 hours under 30°C. The average diameter of the motility rings of the wild-type strain WT was set to 1.0, and then relative diameters of the motility rings of mutant cells were normalized to WT (mean ± SD, $n = 5$). The relative diameter of V was 0.16 ± 0.03. **b,** Motility assay in 0.35% soft agar plate of the *flgI(K63D)*, *flgI(K63A/K95A)*, *flgI(K63A/K95D)*, *flgI(K63D/K95A)* and *flgI(K63D/K95D)* mutants. The diameter of motility ring was measured for eight colonies of each strain after incubating 24 hours at 30°C and compared with a vector control, V. The average diameter of the motility ring of the vector strain V was set to 1.0, and then the diameters of the motility rings of mutant cells were compared with that of V (mean ± SD, $n = 5$). **c,** The cellular expression levels of FlgE, FliC, FlgH and FlgI (top left) and the secretion levels of FlgE and FliC (top right) by immunoblotting with polyclonal anti-FlgE, FliC, FlgH and FlgI antibodies. The positions of molecular mass markers (kDa) are shown on the left. The average secretion level of the wild-type strain WT was set to 1.0, and relative secretion levels of FlgE and FliC were quantified and presented in the bar diagrams in the bottom panel (mean ± SD, $n = 5$). The letter V and WT refers to the empty expression vector (pET22b) and wild type *flgI* expression vector pTY03 (Table 5) for the negative and positive controls, respectively **d**, Number of flagellar filaments per cell for the *flgI(K63A), flgI(K63D)*, *flgI(K95A), flgI(K95D), flgI(K63A/K95A)*, *flgI(K63A/K95D)*, *flgI(K63D/K95A)* and *flgI(K63D/K95D)* mutant strains. Overnight cultured cells were stained by 0.2% phosphotungstic acid (PTA) and observed by electron microscopy. The number of filaments were counted and compared with WT (mean ± SD, $n = 100$).Comparisons between datasets were performed using a two-tailed Student's *t*-test. A P value of < 0.05 was considered to be statistically significant difference. **, $P < 0.01$; ***, $P < 0.001$; ND, no statistical difference.

Structure of the P ring on the polyrod

A *flg*G (G65V) mutant shows abnormally elongated rod decorated with many P rings[66]. The attached P ring is thought to be in the intermediate state of bushing assembly around the rod. In order to identify the interactions between the rod and P ring during LP ring assembly, the structure of the P ring on the polyrod was analyzed. The polyrod-P ring complex (PRP) was purified from the *Salmonella* TH26292 cells (see Methods of Chapter B), and cryoEM images were collected for single particle image analysis using RELION[38] and cryoSPARC[81,82]. The 3D image of the P ring was reconstructed at 2.5 Å resolution with C26 symmetry from 85,463 PRP images extracted from 28,712 cryoEM movie images (Figure 18 and 19). In this analysis, a mask only covering one P ring was applied and the polyrod density was ignored. To determine the interaction between the P ring and polyrod, the PRP were analyzed from 85,119 particles from the same datasets without applying any symmetry, and the 3D image was reconstructed at 3.6 Å resolution. In order to compare the structure of the P ring within the LP ring and the one on the polyrod, the HBB and PRP were aligned with the P ring density. Surprisingly, there were no clear conformation changes observed, and both P rings had the same inner and outer diameters, 135 Å and 260 Å with a root-mean-square deviation (RMSD) of 0.67 Å between the two models (Figure 30a). The blurred ring density beneath the P ring in the LP ring structure was also observed in the P ring on the polyrod.

Structural changes of FlgI before and after the interaction with FlgH

Although the structure of FlgI in the LP ring complex and that in the P ring on the polyrod are almost identical, the inner and outer pockets of the P ring that accept FlgH loops showed some differences. In order to accept the FlgH loops, those pockets change from the “closed” state to the“open” state (Figure 30b-e). In the inner pocket, the side chains of Met-46 and Gln-49 of FlgI move to accept Leu-44 and Phe-45 of FlgH (Figure 30d). In the outer pocket, the side chains of Val-110 and Leu-156 of FlgI move to accept Ile-30 and Phe-31 of FlgH (Figure 30e).

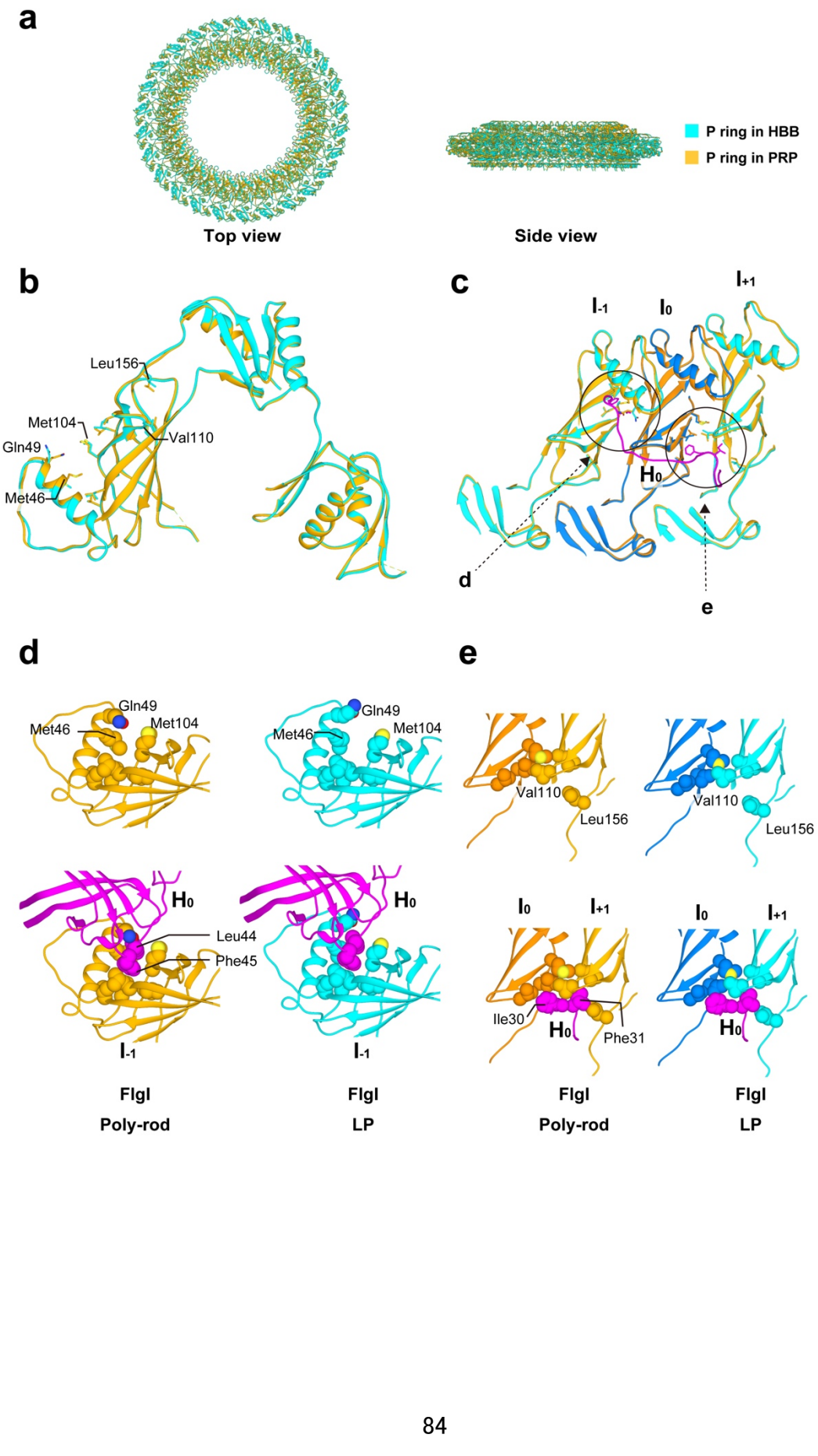
a
Top view
Side view
P ring in HBB
P ring in PRP
b
Leu156
Met104
Gln49
Val110
Met46
c
I+1
I-1
I0
H0
d
e
d
Gln49
Met46
Met104
H0
Leu44
Phe45
I-1
FlgI
Poly-rod
FlgI
LP
e
Val110
Leu156
I0
I+1
Ile30
H0
Phe31
FlgI
Poly-rod
FlgI
LP

Figure 30 The comparison between the P ring on the poly-rod and in the LP ring. **a,** Comparison between the P ring in the HBB (cyan) and PRP (orange). **b**, FlgI in a Cα ribbon representation. Side chains involved in the interactions with the FlgH loop are displayed in stick. **c,** The top view of the interactions between FlgH (H_0: magenta) and the inner and outer pockets of FlgI (I_0, $I_{\pm1}$). **d, e,** The open and closed states of FlgI pockets in the P ring on the poly-rod (left, orange) and FlgI in the LP ring (right, cyan). **d,** A magnified view of the inner pocket. The side chains of Met-46 and Gln-49 of FlgI move to accept the Leu-44 and Phe-45 of FlgH. **e,** A magnified view of the outer pocket. The side chains of Val-110 and Leu-156 of FlgI move to accept the Ile-30 and Phe-31 of FlgH.

In order to clarify how the P ring dissociates from the rod after L ring assembly, the density map of the rod in the PRP was aligned to that of the HBB, and the atomic models of the P ring and native distal rod were docked into each map (5 FlgF, 24 FlgG; Miyata *et al. in preparation*: Figure 31a) to compare the relative position of the P ring to the rod (Figure 31b). Note that 6 FlgG molecules out of 24 in this atomic model are missing their tips of L-stretch (Ala-54 to Ser-64) because their densities were not clear enough to build atomic models (Figure 31). The P ring is perpendicular to the rod in the HBB but not in the PRP: The P ring in the PRP is tilted 3.0 degrees relative to the P ring in the HBB (Figure 31b).

Based on this aligned atomic models and density maps, the interaction sites between the P ring and rod were examined in the HBB and PRP. In both structures, the P ring interacts with the distal rod in three parts: the upper, middle and lower parts (Figure 31c-e). Among these threes, the upper and middle part interactions were found in both the HBB and PRP, but the lower part interaction was found only in the PRP. For both the HBB and PRP, Lys-63 and Lys-95 (Figure 31e positive charge), Thr-34, and Gln-35 of FlgI interact with FlgG at the residues of Asp-109, Asp-154, Glu-203 (Figure 31e negative charge) and the tip of L-stretch, Gly-53 to Glu-58 in the upper part (Figure 31e top panel). The flexible residues of FlgI (126–137) and FlgG (54–64) also appear to interact with each other in the middle part in both structures (Figure 31e middle panel). On the other hand, the lower part interaction is present only in the PRP (Figure 31e lower panel), and the flexible residues of FlgI (264–295) presumably interact with the L-stretch tips of FlgG (53–58). The densities connecting the P ring and rod, which are clearly visible in Figure 31e, suggest these interactions.

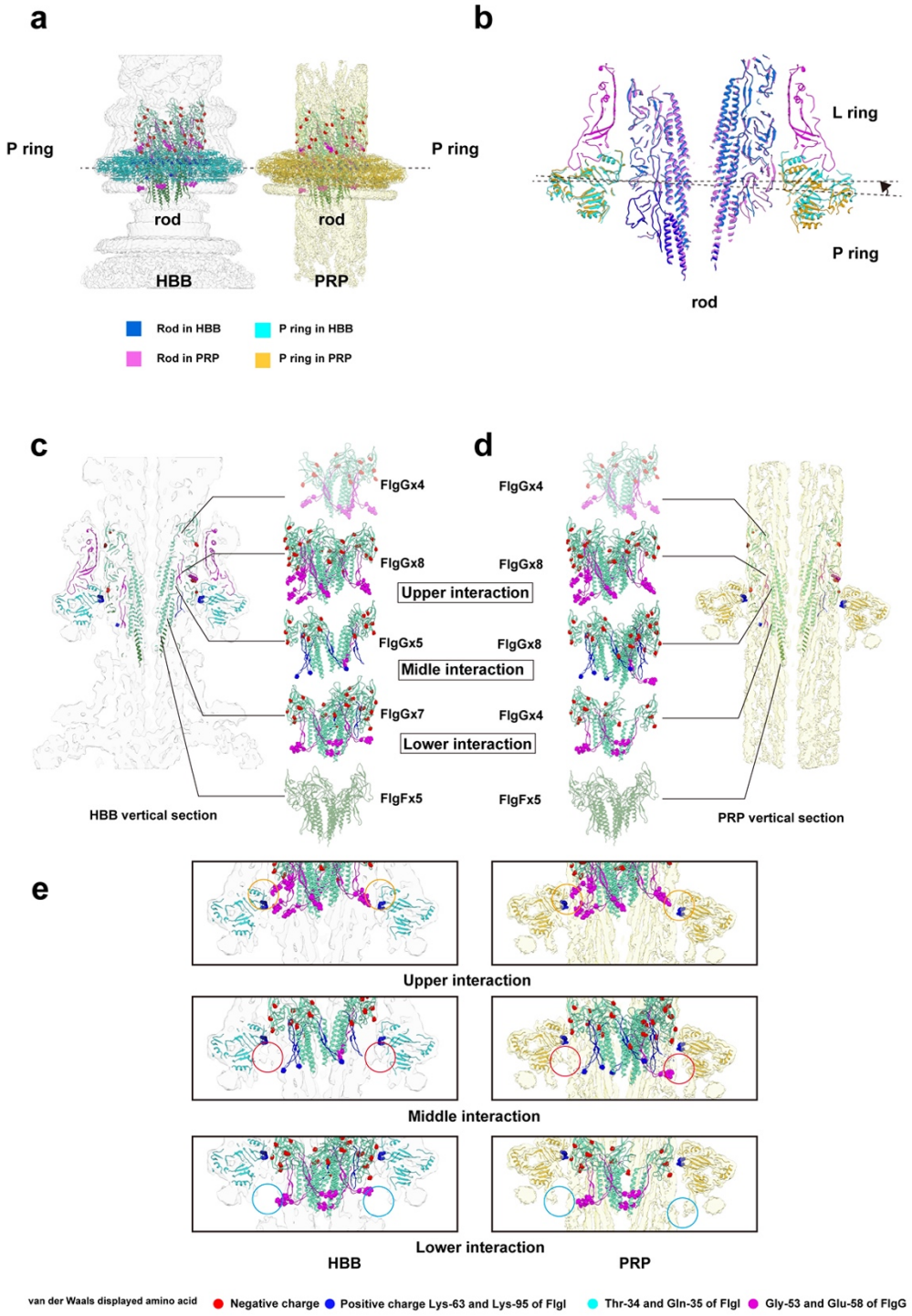
a
P ring
P ring
rod
rod
HBB
PRP
Rod in HBB
P ring in HBB
Rod in PRP
P ring in PRP
b
L ring
P ring
rod
c
d
FlgGx4
FlgGx8
Upper interaction
FlgGx5
FlgGx8
Midle interaction
FlgGx7
FlgGx4
Lower interaction
FlgFx5
FlgFx5
HBB vertical section
PRP vertical section
e
Upper interaction
Middle interaction
Lower interaction
HBB
PRP
van der Waals displayed amino acid
Negative charge
Positive charge Lys-63 and Lys-95 of FlgI
Thr-34 and Gln-35 of FlgI
Gly-53 and Glu-58 of FlgG

Figure 31 The interactions between P ring and rod during the LP ring assembly. a, Side views of the HBB and PRP. The atomic models of the P ring and rod are superimposed to the density map. **b**, Vertical sections of the L ring (purple), P ring (cyan) and the rod (blue) in the HBB are compared to the P ring (yellow) and rod (pink) in the PRP. Their positions were aligned by the density maps of the rod in the PRP and HBB. The dashed lines indicate the center lines of the P rings. **c**, **d**, Side views of the HBB and PRP, and the atomic models of rod. FlgF is colored green, FlgG in light green and the L stretch of FlgG in magenta. Six L-stretches without the tip are colored in blue. The FlgI in the HBB is colored cyan and that in the PRP in orange. **e**, Three interaction parts between the P ring and the rod. Circles indicate the interaction sites.

Discussion

Stability of the LP ring

The atomic model of the LP ring around the rod provided many insights into the mechanisms of mechanical stability, bushing function, and assembly of the LP ring. The LP ring is stable even against harsh treatments by acids and urea[50,51] and remains in the cell envelope even after the ejection of the flagellar axial structure from the bacterial cell body[52–56]. This extremely high stability can now be explained by the intricate intersubunit interactions between FlgH subunits, between FlgI subunits and between FlgH and FlgI. FlgH forms the three-layer cylinder structure of the L ring, consisting of two cylindrical β-barrels with their β-strands oriented nearly perpendicular to each other and the extended chain in the third layer lining them on the outer surface (Figure 20cd and 26ab). Each FlgH subunit interacts with six adjacent FlgH subunits, making the L ring structure even more stable. Intersubunit interactions of FlgI in the P ring are not so extensive as those of FlgH in the L ring but each of the three domains of FlgI intimately interacts with domains of the adjacent subunits, even by forming intersubunit β-sheets (Figure 26c–f). Then the extensive hydrophobic interactions between the extended chain of FlgH at the bottom surface of the L ring and the two pockets of FlgI on the upper surface of the P ring make the entire LP ring structure very stable (Figure 26g).

Stoichiometry of the LP ring and the step size of motor rotation

The outer surface of the rod and inner surface of the LP ring are both very smooth (Figure 20a), indicating that these two structures are optimally designed for free rotation of the rod inside the LP ring without much friction. The outer surface of the rod is highly negatively charged[9,10,72,74] but the inner surface of the LP ring is charged both negatively and positively, probably to balance repulsive and attractive forces to keep the rod stably positioned and rotate at the center of the LP ring (Figure 28a and 32). Nanophotometric observations of individual motor rotation have shown 26 steps per revolution[94,95], and these data have been interpreted as the steps being generated by the repeated association and dissociation of the stator protein MotA and the rotor protein FliG for torque generation because the number of FliF-FliG subunits forming the MS ring and part of the C ring was thought to be 25 to 26 at the time[70,96,97]. However, recent structural analysis

of the MS ring formed by overexpressed FliF revealed its symmetry to be 33-fold with a variation from 32 to 35 (Ref.[98]), and the analysis of the flagellar basal body showed the MS ring to have 34-fold symmetry without variation and the C ring to have a small symmetry variation around 34-fold[99]. These results indicate that the number of FliG on the C ring is mostly 34 and therefore have invalidated the previous interpretation that the 26 steps per revolution reflect the elementary process of torque generation. Because the LP ring has 26-fold symmetry, the observed steps may be caused by potential minima formed by electrostatic interactions between the rod and LP ring.

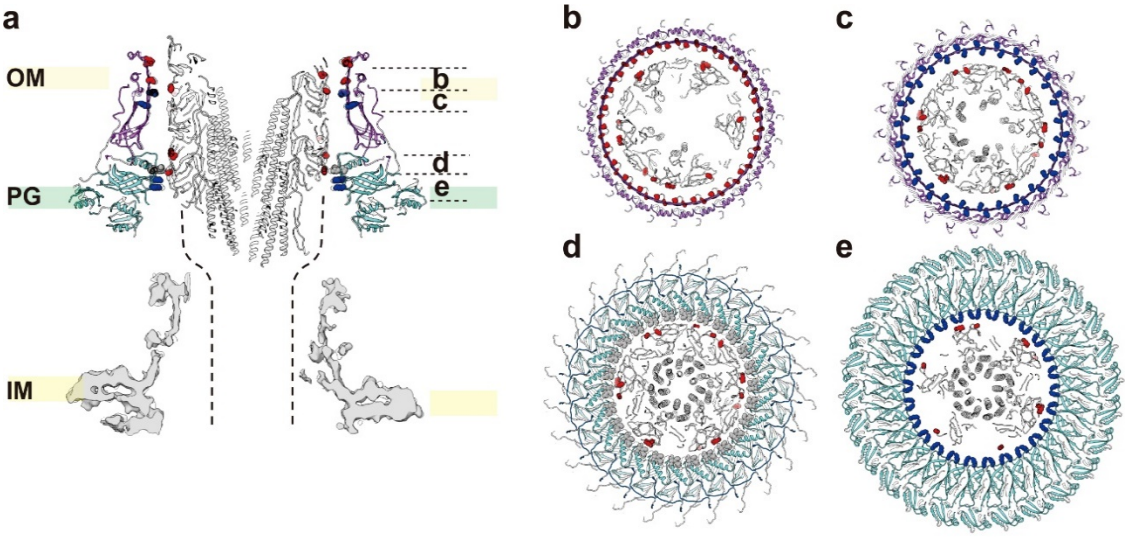

Figure 32 Interactions between the rod and LP ring and their assembly process. a, Vertical section of the atomic model of the rod (gray), L ring (purple), P ring (cyan) with the map of the MS ring at the bottom (gray). Charged amino acid residues are displayed with negative in red (Asp-109, Asp-154, Glu-203 of FlgG and Asp-78, Asp-86, Glu-104 of FlgH) and positive in blue (Lys-69, Lys-114 of FlgH and Lys-63, Lys-95 of FlgI). Four polar residues from Thr-33 to Thr-36 of FlgI in the P ring loop, which is located most closely to the rod surface, are shown in gray. The dashed lines are where the proximal rod is expected to exist. **b**, **c**, **d**, **e**, Axial view of four horizontal slices of the rod and LP ring as indicated in **a**, showing repulsive and attractive interactions between the rod and LP ring: **b**, repulsive interactions; **c**, attractive interactions; **d**, the smallest gap between the rod and LP ring with non-charged residues of FlgI in the P ring loop; **e**, attractive interactions.

Mechanism of LP ring assembly around the rod

Although the LP ring is a stable component of the HBB even after its isolation from the cell, the LP ring easily slips off the rod when the basal body is isolated without the hook[50,57,99], indicating very weak interactions between the rod and LP ring to keep the LP ring in the proper position around the rod. In the absence of FlgH, however, the basal body formation stops just after completion of P ring assembly by FlgI around the rod to form a structure called "candlestick"[57,100], indicating that the P ring is tightly attached to the rod until the L ring is assembled above it. Among the *flgG* mutants that form the polyrod, many P rings are assembled around the polyrod formed by *flgG* (G65V) and *flgG* (P52L) mutants whereas no P ring is observed by FlgG mutations of G53R, G183R or deletion of residues 54–57 (Ref.[59,66]). All these FlgG mutations are located in the L-stretch formed by *Salmonella* FlgG specific sequence not present in FlgE (Figure 33ab). In this study, the PRP structure formed by the *flgG* (G65V) mutant was analyzed by cryoEM single particle image analysis. The P ring structure in the LP ring and that on the polyrod were almost identical, but differences were observed in the inner and outer pockets of the P ring accepting FlgH loops where the pockets changed to the "open" from the "closed" form by the insertion of the FlgH loops.

In both the HBB and PRP, the P ring interacts with the L-stretch of FlgG in two parts: the upper and middle parts. The lower part interaction was observed only in the PRP. While the P ring is perpendicular to the rod in the HBB, it is tilted in the PRP by 3 degrees. In the upper part, Lys-63 and Lys-95 of FlgI are located on the inner surface of the P ring and directly face the negatively charged surface of the rod or the tips of the L-stretch of FlgG in both structures. Mutations of those lysin residues to either alanine to diminish the positive charge or aspartate to have the negative charge impair cell motility, possibly by inhibiting P ring formation (Figure 29). Hence, these two lysine residues are likely to play important roles in P ring assembly on the negatively charged surface of the rod. This is consistent with no P ring assembly by FlgG polyrod mutations G53R and G183R, which would disturb P ring assembly by repulsive force (Figure 33d), as well as deletion of restudies 54–57, which would put Glu-58 of FlgG at the tip of the L-stretch too far from Lys-63 and Lys-95 of FlgI (Figure 33e). Therefore, Lys-63 and Lys-95 of FlgI are supposed to be essential for the initial binding of FlgI to the rod surface to form the P ring. In the middle part, 126–137 of FlgI and the tip of the L-stretch in FlgG appear

to interact with each other in both HBB and PRP structures. In this interaction, the tips of the FlgG L-stretch are flexible and disordered. The residues 126–137 of FlgI, which are facing the outer surface of the rod are also flexible and are located in the FlgI-IR$_U$ domain containing the inner and outer pockets of the P ring accepting the FlgH loops. Those flexible residues are thought to be able to change the interaction partners depending on the situations and to act as a scaffold for P ring assembly. In the lower part, the extended densities observed only in the PRP seem to reflect the interaction between FlgG and FlgI, but it could also be an artificial one due to the polyrod structure. In the case of HBB, FlgI interacts with FlgG and FlgF in the lower parts but FlgI interacts only with FlgG in the PRP because the polyrod is composed of only FlgG.

Based on these results, I propose the following scenario (Figure 34). First, the negatively charged surface of FlgG attracts positively charged residues of FlgI (Lys-63 and Lys-95) so that the P ring assembles around the rod by using residues 126–137 of FlgI as a scaffold. Next, FlgH assembles on the P ring to form the L ring, induces conformational changes of FlgI to cause the dissociation of residues 126–137 of FlgI from the rod surface, making the P ring free from and perpendicular to the rod so that the rod becomes free to rotate. Once LP ring assembly is completed, the potential barriers for rod rotation inside the LP ring becomes extremely small so that the rod can rotate smoothly. A molecular dynamics simulation of rod rotation inside the LP ring is underway to clarify the dynamics and energetics of rod rotation.

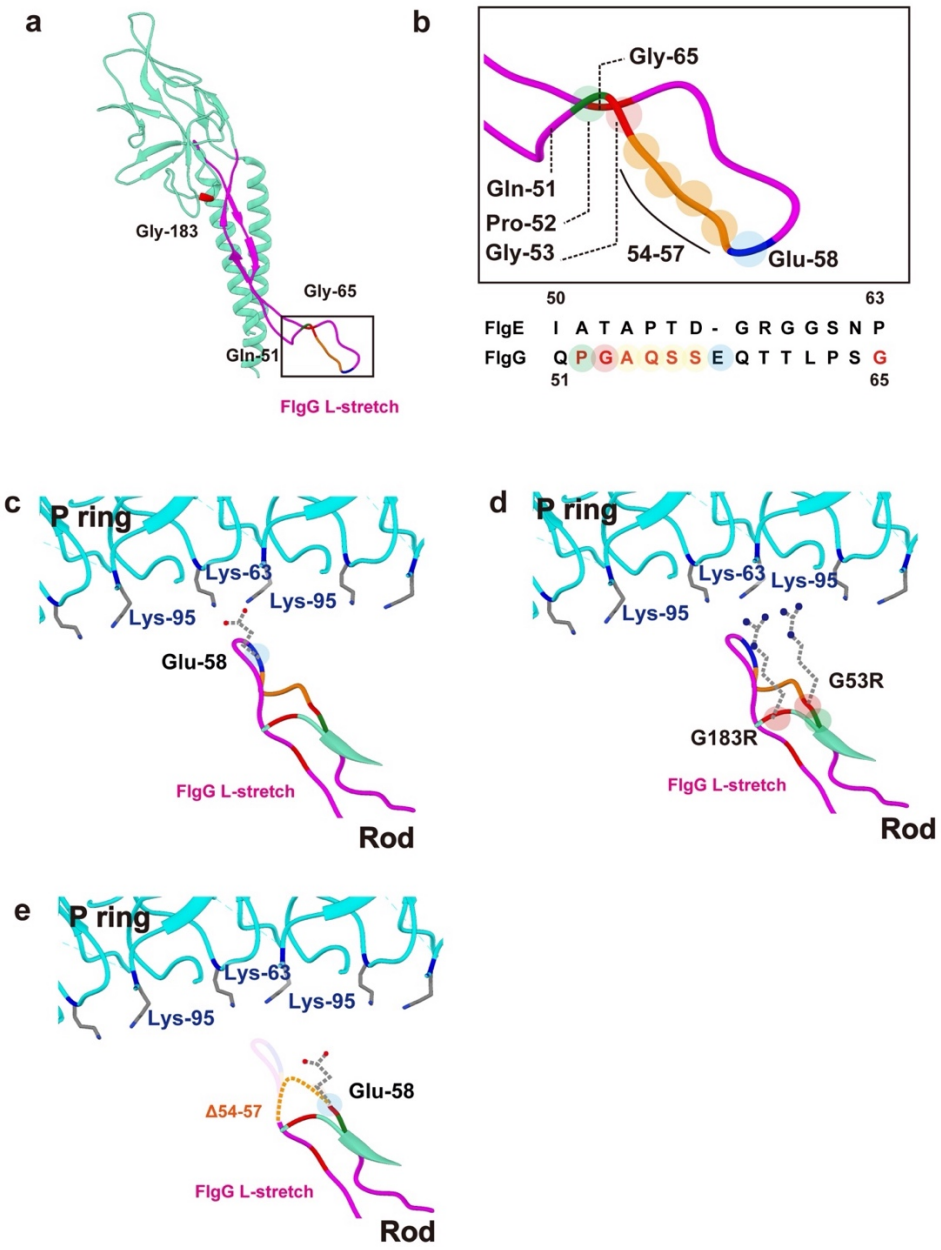

Figure 33 Interactions between FlgG in the rod and FlgI in the P ring. a, Representative FlgG structure of *Salmonella* (Miyata *et al.*, *in progress*).The L-stretch is colored in magenta. **b**, The magnified view of flexible residues (52–58) in the L-stretch. Those which predicted to interact with FlgI are displayed by different colors. **c**, Possible interactions of Lys-63 and Lys-95 of FlgI in the P ring and Glu-58. Glu-58 is expected to interact with Lys-63 and Lys-95 and helps P ring assembly. **d,** Possible interactions of Lys-63 and Lys-95 of FlgI in the P ring and Arg-183 and Gly-53 of FlgG in the rod. The G183R and G53R mutation of FlgG is expected to disturb P ring assembly by repulsive force. **e**, Expected change of the Glu-58 position in the Δ54–57 mu tant of FlgG, making the distance between Glu-58 of FlgG and Lys-63 and Lys-95 of FlgI too far for interaction.

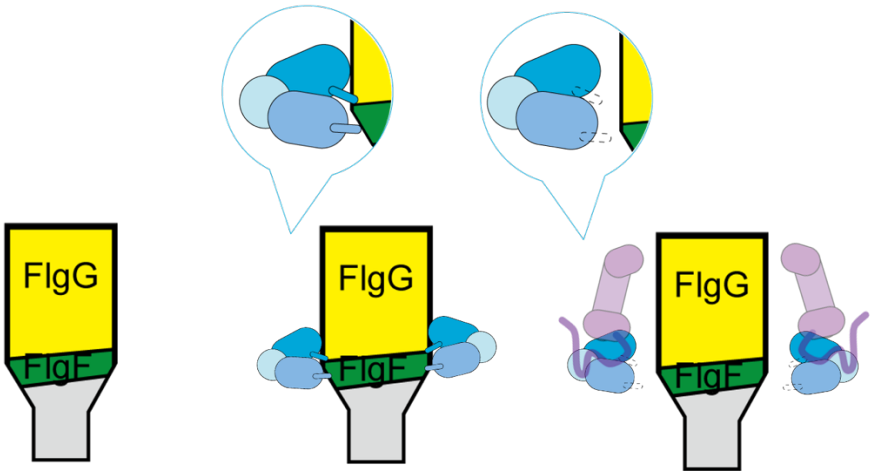

Figure 34 The schematic diagram of LP ring assembly around rod. The negatively charged surface of the FlgG rod attracts positively charged residues of FlgI (Lys-63 and Lys-95) so that FlgI subunits assemble around the rod by using flexible residues of FlgI and FlgG. The P ring is tilted in this stage possibly due to the helical nature of the rod structure (middle). When L ring assembly on the P ring is completed, the P ring dissociates from the rod so that it becomes free from and perpendicular to the rod (right).

Conclusion

In this study, it was revealed that the flagellar filament formed by FljB has an advantage over the FliC filament by allowing the cells to have better motility under highly viscos conditions. The structure of the FljB filament was clarified by electron cryomicroscopy at 3.6 Å resolution. The subunit structures and intersubunit packing interactions were well conserved between FljB and FliC except for the position and mobility of domain D3 on the surface of the filament. The advantage of the FljB filament in the swimming motility under highly viscous conditions may have an important role in infection when bacteria need go through viscous layers of mucosa on the surface of intestinal cells or keep a biofilm in good condition with the cells with FljB filaments acting as a nutrition deliverer.

I also clarified the structure of the LP ring around the rod and P ring on polyrod by electron cryomicroscopy at 3.5 Å and 2.5 Å resolution, respectively. The LP ring structure shows 26-fold rotational symmetry and intricate intersubunit interactions of each subunit with up to six partners forming a basket like structure folded at right angles that explains the structural stability. FlgI and FlgH interacts via conserved hydrophobic amino acids. The inner surface of the LP ring is charged both positively and negatively, suggesting that both attractive and repulsive force keep the rod at the center of the LP ring to minimize the frictional force between the rod and LP ring. Positively charged Lys-63 and Lys-95 and the flexible residues 126–137 of FlgI presumably play important roles in the initial assembly of the P ring around the rod.

Based on the results of structural and biochemical experiments, I was able to explain the function of the filamentous propeller, characteristics of the molecular bushing, and the LP ring self-assembly mechanisms around the rod. However, in order to clarify the relationship between the filament structure and motility behavior difference, or the relationship between the rod-LP ring interaction and rotational efficiency of the motor, further computational analyses are needed. Understanding the mechanical and dynamic properties of the LP ring as a nanoscale bushing would also be quite interesting in physics and useful in nanotechnology applications, but it requires fully atomic molecular dynamics simulations of the rod rotation within the LP ring. Although such simulations

would need to deal with hundreds of millions of atoms and therefore is not a simple task, such study is underway because it is now feasible by the development of high-speed computers, such as Fugaku.

Data availability

The cryoEM 3D density map of FljB filaments was deposited to the Electron Microscopy Data Bank (EMDB) under accession code EMD-9896, and its atomic model coordinates were deposited to the Protein Data Bank (PDB) under accession code 6JY0 (Ref.[32]).

The cryoEM 3D density map of HBB and LP ring were deposited to EMDB under EMD-30409 and EMD-30398, respectively. Atomic models of FlgH and FlgI are available in PDB with accession codes 7CLR (Ref.[78]).

Acknowledgments

I thank Drs. Shigeru Yamaguchi for his kind gift of SJW590, Yusuke Morimoto for technical help in identifying the mutation site of the *fljB* allele of SJW590, Kelly Hughes for kindly providing strain SJW203 and HK26292, and Hideyuki Matsunami for kindly providing the HK1002 strain. I would like to thank Dr. Katsumi Imada for helpful suggestion in constructing the atomic model. I gratefully acknowledge the work of past and present members of our laboratory. I thank Drs. Shoko Toma and Naoya Terahara for analyzing swimming speed of *fljB* and *fliC* mutants. I thank Drs. Miki Kinoshita and Tohru Minamino for their help in genetic, biochemical and physiological experiments. I thank Drs. Tomoko Miyata and Fumiaki Makino for cryoEM data collection of the HBB and supporting experiments related to the cryoEM analysis. I am extremely grateful to my supervisors, Drs. Keiichi Namba, Takayuki Kato and Tohru Minamino, for their invaluable advice, continuous support, and patience during my PhD study. I also thank Drs. Hajime Fukuoka, Atsushi Nakagawa and Tatsuro Fukagawa for reviews and comments on this work.

Funding

This work has been supported by JSPS KAKENHI Grant Number JP25000013 (to K.N.), JP18K06155 (to T.M. (Tomoko Miyata)), JP26293097 and JP19H03182 (to T.M. (Tohru Minamino)), and MEXT KAKENHI Grant Number JP15H01640 and JP20H05532 (to T.M. (Tohru Minamino)). This work has also been supported by Platform Project for Supporting Drug Discovery and Life Science Research (BINDS) from AMED under Grant Number JP19am0101117 to K.N., by the Cyclic Innovation for Clinical Empowerment (CiCLE) from AMED under Grant Number JP17pc0101020 to K.N. and by JEOL YOKOGUSHI Research Alliance Laboratories of Osaka University to K.N. T.Y. was supported by RIKEN as a Junior Research Associate and supported by JPSP as a JSPS Research Fellowships for Young Scientists.

References

1. Zarkani, A. A. *et al. Salmonella* heterogeneously expresses flagellin during colonization of plants. *Microorganisms* **8**, 815 (2020).
2. Haiko, J. & Westerlund-Wikström, B. The role of the bacterial flagellum in adhesion and virulence. *Biology (Basel).* **2**, 1242–1267 (2013).
3. Rossez, Y., Wolfson, E. B., Holmes, A., Gally, D. L. & Holden, N. J. Bacterial Flagella: Twist and Stick, or Dodge across the Kingdoms. *PLOS Pathog.* **11**, e1004483 (2015).
4. Berg, H. C. The rotary motor of bacterial flagella. *Annu. Rev. Biochem.* **72**, 19–54 (2003).
5. Magariyama, Y. *et al.* Very fast flagellar rotation. *Nature* **371**, 752 (1994).
6. Macnab, R. M. & Ornston, M. K. Normal-to-curly flagellar transitions and their role in bacterial tumbling. Stabilization of an alternative quaternary structure by mechanical force. *J. Mol. Biol.* **112**, 1–30 (1977).
7. DeRosier, D. J. The turn of the screw: The bacterial flagellar motor. *Cell* **93**, 17–20 (1998).
8. Minamino, T., Terahara, N., Kojima, S. & Namba, K. Autonomous control mechanism of stator assembly in the bacterial flagellar motor in response to changes in the environment. *Mol. Microbiol.* **109**, 723–734 (2018).
9. Fujii, T. *et al.* Identical folds used for distinct mechanical functions of the bacterial flagellar rod and hook. *Nat. Commun.* **8**, 14276 (2017).
10. Saijo-Hamano, Y., Matsunami, H., Namba, K. & Imada, K. Architecture of the bacterial flagellar distal rod and hook of *Salmonella*. *Biomolecules* **9**, 260 (2019).
11. Minamino, T. & Namba, K. Self-assembly and type III protein export of the bacterial flagellum. *J. Mol. Biol. Biotechnol.* **7**, 5–17 (2004).
12. Nakamura, S. & Minamino, T. Flagella-driven motility of bacteria. *Biomolecules* **9**, 279 (2019).
13. Darnton, N. C. & Berg, H. C. Force-extension measurements on bacterial flagella: Triggering polymorphic transformations. *Biophys. J.* **92**, 2230–2236 (2007).
14. Asakura, S. Polymerization of flagellin and polymorphism of flagella. *Adv. Biophys.* **1**, 99–155 (1970).
15. Stocker, B. A. D. Measurements of rate of mutation of flagellar antigenic phase in *Salmonella typhimurium*. *J. Hyg. (Lond).* **47**, 398–413 (1949).
16. Andrewes, F. W. Studies in group agglutination. II.—The absorption of agglutinin in the diphasic *salmonellas*. *J. Pathol. Bacteriol.* **28**, 345–359 (1925).
17. Silverman, M., Zieg, J., Hilmen, M. & Simon, M. Phase variation in *Salmonella*: Genetic analysis of a recombinational switch. *PNAS.* **76**, 391–395 (1979).

18. Zieg, J., Silverman, M., Hilmen, M. & Simon, M. Recombinational switch for gene expression. *Science.* **196**, 170–172 (1977).
19. Zieg, J. & Simon, M. Analysis of the nucleotide sequence of an invertible controlling element. *PNAS.* **77**, 4196–4200 (1980).
20. Bonifield, H. R. & Hughes, K. T. Flagellar phase variation in *Salmonella enterica* is mediated by a posttranscriptional control mechanism. *J. Bacteriol.* **185**, 3567–3574 (2003).
21. Aldridge, P. D. *et al.* Regulatory protein that inhibits both synthesis and use of the target protein controls flagellar phase variation in *Salmonella enterica*. *PNAS.* **103**, 11340–11345 (2006).
22. Aldridge, P., Gnerer, J., Karlinsey, J. E. & Hughes, K. T. Transcriptional and translational control of the *Salmonella fliC* gene. *J. Bacteriol.* **188**, 4487–4496 (2006).
23. Yamamoto, S. & Kutsukake, K. FljA-mediated posttranscriptional control of phase 1 flagellin expression in flagellar phase variation of *Salmonella enterica* serovar typhimurium. *J. Bacteriol.* **188**, 958–967 (2006).
24. Horstmann, J. A. *et al.* Methylation of *Salmonella* Typhimurium flagella promotes bacterial adhesion and host cell invasion. *Nat. Commun.* **11**, 2013 (2020).
25. Ikeda, J. S. *et al.* Flagellar phase variation of *Salmonella enterica* serovar typhimurium contributes to virulence in the murine typhoid infection model but does not influence *Salmonella* induced enteropathogenesis. *Infect. Immun.* **69**, 3021–3030 (2001).
26. Horstmann, J. A. *et al.* Flagellin phase-dependent swimming on epithelial cell surfaces contributes to productive *Salmonella* gut colonisation. *Cell. Microbiol.* **19**, e12739 (2017).
27. Samatey, F. A. *et al.* Structure of the bacterial flagellar protofilament and implications for a switch for supercoiling. *Nature* **410**, 331–337 (2001).
28. Yonekura, K., Maki-Yonekura, S. & Namba, K. Complete atomic model of the bacterial flagellar filament by electron cryomicroscopy. *Nature* **424**, 643–650 (2003).
29. Maki-Yonekura, S., Yonekura, K. & Namba, K. Conformational change of flagellin for polymorphic supercoiling of the flagellar filament. *Nat. Struct. Mol. Biol.* **17**, 417–422 (2010).
30. Mimori-Kiyosue, Y., Yamashita, I., Fujiyoshi, Y., Yamaguchi, S. & Namba, K. Role of the outermost subdomain of *Salmonella* flagellin in the filament structure revealed by electron cryomicroscopy. *J. Mol. Biol.* **284**, 521–530 (1998).
31. Yamaguchi, S., Fujita, H., Sugata, K., Taira, T. & Iino, T. Genetic analysis of *H2*, the structural gene for phase-2 flagellin in *Salmonella*. *J. Gen. Microbiol.* **130**, 255–265 (1984).
32. Yamaguchi, T. *et al.* Structural and functional comparison of *Salmonella* flagellar filaments composed of FljB and FliC. *Biomolecules* **10**, 246 (2020).
33. Datsenko, K. A. & Wanner, B. L. One-step inactivation of chromosomal genes in *Escherichia coli* K-12 using PCR products. *PNAS.* **97**, 6640–6645 (2000).

34. Hara, N., Namba, K. & Minamino, T. Genetic characterization of conserved charged residues in the bacterial flagellar type III export protein FlhA. *PLoS One* **6**, e22417 (2011).
35. Toma, S. Structure of the Flagellar Filament of *Salmonella* FljB and Its Difference from the FliC Filament. *Dr. thesis* (2015).
36. Dubochet, J. *et al.* Cryo-electron microscopy of vitrified specimens. *Q. Rev. Biophys.* **21**, 129–228 (1988).
37. Zhang, K. Gctf: Real-time CTF determination and correction. *J. Struct. Biol.* **193**, 1–12 (2016).
38. Zivanov, J. *et al.* New tools for automated high-resolution cryo-EM structure determination in RELION-3. *elife* **7**, e42166 (2018).
39. Webb, B. & Sali, A. Comparative protein structure modeling using MODELLER. *Curr. Protoc. Bioinforma.* **54**, 5.6.1-5.6.37. (2016).
40. Pettersen, E. F. *et al.* UCSF Chimera - A visualization system for exploratory research and analysis. *J. Comput. Chem.* **25**, 1605–1612 (2004).
41. Emsley, P., Lohkamp, B., Scott, W. G. & Cowtan, K. Features and development of *Coot*. *Acta Crystallogr. D Biol. Crystallogr.* **66**, 486–501 (2010).
42. Afonine, P. V *et al.* Real-space refinement in PHENIX for cryo-EM and crystallography. *Acta Crystallogr. Sect. D Struct. Biol.* **74**, 531–544 (2018).
43. Sievers, F. *et al.* Fast, scalable generation of high-quality protein multiple sequence alignments using Clustal Omega. *Mol. Syst. Biol.* **7**, 539 (2011).
44. Mimori, Y. *et al.* The structure of the R-type straight flagellar filament of *Salmonella* at 9 Å resolution by electron cryomicroscopy. *J. Mol. Biol.* **249**, 69–87 (1995).
45. Liebschner, D. *et al.* Macromolecular structure determination using X-rays, neutrons and electrons: Recent developments in *Phenix*. *Acta Crystallogr. Sect. D Struct. Biol.* **75**, 861–877 (2019).
46. Vonderviszt, F., Aizawa, S.-I. & Namba, K. Role of the disordered terminal regions of flagellin in filament formation and stability. *J. Mol. Biol.* **221**, 1461–1474 (1991).
47. Flemming, H. C. *et al.* Biofilms: An emergent form of bacterial life. *Nat. Rev. Microbiol.* **14**, 563–575 (2016).
48. Houry, A. *et al.* Bacterial swimmers that infiltrate and take over the biofilm matrix. *PNAS.* **109**, 13088–13093 (2012).
49. Kubori, T. *et al.* Purification and characterization of the flagellar hook-basal body complex of Bacillus subtilis. *Mol. Microbiol.* **24**, 399–410 (1997).
50. Akiba, T., Yoshimura, H. & Namba, K. Monolayer crystallization of flagellar L-P rings by sequential addition and depletion of lipid. *Science* **252**, 1544–1546 (1991).

51. Aizawa, S.-I., Dean, G. E., Jones, C. J., Macnab, R. M. & Yamaguchi, S. Purification and Characterization of the Flagellar Hook-Basal Body Complex of *Salmonella typhimurium*. *J. Bacteriol.* **161**, 836–849 (1985).

52. Kaplan, M. *et al.* In situ imaging of the bacterial flagellar motor disassembly and assembly processes. *EMBO J.* **38**, e100957 (2019).

53. Zhu, S. *et al.* In situ structures of polar and lateral flagella revealed by cryo-electron tomography. *J. Bacteriol.* **201**, e00117-19 (2019).

54. Ferreira, J. L. *et al.* γ-proteobacteria eject their polar flagella under nutrient depletion, retaining flagellar motor relic structures. *PLoS Biol.* **17**, e3000165 (2019).

55. Zhu, S. & Gao, B. Bacterial Flagella Loss under Starvation. *Trends Microbiol.* vol. 28 785–788 (2020).

56. Kaplan, M. *et al.* Bacterial flagellar motor PL-ring disassembly subcomplexes are widespread and ancient. *PNAS.* **117**, 8941–8947 (2020).

57. Kubori, T., Shimamoto, N., Yamaguchi, S., Namba, K. & Aizawa, S.-I. Morphological pathway of flagellar assembly in *Salmonella typhimurium*. *J. Mol. Biol.* **226**, 433–446 (1992).

58. Nambu, T., Minamino, T., Macnab, R. M. & Kutsukake, K. Peptidoglycan-hydrolyzing activity of the FlgJ protein, essential for flagellar rod formation in *Salmonella typhimurium*. *J. Bacteriol.* **181**, 1555–1561 (1999).

59. Cohen, E. J. & Hughes, K. T. Rod-to-hook transition for extracellular flagellum assembly is catalyzed by the L-ring-dependent rod scaffold removal. *J. Bacteriol.* **196**, 2387–2395 (2014).

60. Rapoport, T. A. Protein translocation across the eukaryotic endoplasmic reticulum and bacterial plasma membranes. *Nature* **450**, 663–669 (2007).

61. Homma, M., Komeda, Y., Iino, T. & Macnab, R. M. The *flaFIX* gene product of *Salmonella typhimurium* is a flagellar basal body component with a signal peptide for export. *J. Bacteriol.* **169**, 1493–1498 (1987).

62. Jones, C. J., Homma, M. & Macnab, R. M. L-, P-, and M-ring proteins of the flagellar basal body of *Salmonella typhimurium*: Gene sequences and deduced protein sequences. *J. Bacteriol.* **171**, 3890–3900 (1989).

63. Nambu, T. & Kutsukake, K. The *Salmonella* FlgA protein, a putative periplasmic chaperone essential for flagellar P ring formation. *Microbiology* **146**, 1171–1178 (2000).

64. Matsunami, H., Yoon, Y. H., Meshcheryakov, V. A., Namba, K. & Samatey, F. A. Structural flexibility of the periplasmic protein, FlgA, regulates flagellar P-ring assembly in *Salmonella enterica*. *Sci. Rep.* **6**, 27399 (2016).

65. Hizukuri, Y., Yakushi, T., Kawagishi, I. & Homma, M. Role of the Intramolecular Disulfide Bond in FlgI, the Flagellar P-Ring Component of *Escherichia coli*. *J. Bacteriol.* **188**, 4190–4197 (2006).

66. Chevance, F. F. V. *et al.* The mechanism of outer membrane penetration by the eubacterial flagellum and implications for spirochete evolution. *Genes Dev.* **21**, 2326–2335 (2007).
67. Hizukuri, Y., Kojima, S., Yakushi, T., Kawagishi, I. & Homma, M. Systematic Cys mutagenesis of FlgI, the flagellar P-ring component of *Escherichia coli*. *Microbiology* **154**, 810–817 (2008).
68. Okuda, S. & Tokuda, H. Lipoprotein sorting in bacteria. *Annu. Rev. Microbiol.* **65**, 239–259 (2011).
69. Schoenhals, G. J. & Macnab, R. M. Physiological and biochemical analyses of FlgH, a lipoprotein forming the outer membrane L ring of the flagellar basal body of *Salmonella typhimurium*. *J. Bacteriol.* **178**, 4200–4207 (1996).
70. Jones, C. J., Macnab, R. M., Okino, H. & Aizawa, S.-I. Stoichiometric analysis of the flagellar hook-(basal-body) complex of *Salmonella typhimurium*. *J. Mol. Biol.* **212**, 377–387 (1990).
71. Sosinsky, G. E. *et al.* Mass determination and estimation of subunit stoichiometry of the bacterial hook-basal body flagellar complex of *Salmonella typhimurium* by scanning transmission electron microscopy. *PNAS.* **89**, 4801–4805 (1992).
72. Tan, J. *et al.* Structural basis of assembly and torque transmission of the bacterial flagellar motor. *Cell* **184**, 2665-2679.e19 (2021).
73. Hiraoka, K. D. *et al.* Straight and rigid flagellar hook made by insertion of the FlgG specific sequence into FlgE. *Sci. Rep.* **7**, 46723 (2017).
74. Johnson, S. *et al.* Molecular structure of the intact bacterial flagellar basal body. *Nat. Microbiol.* **6**, 712–721 (2021).
75. Minamino, T., Kinoshita, M. & Namba, K. Fuel of the bacterial Flagellar type III protein export apparatus. *Methods Mol. Biol.* **1593**, 3–16 (2017).
76. Kawamoto, A. *et al.* Common and distinct structural features of *Salmonella* injectisome and flagellar basal body. *Sci. Rep.* **3**, 3369 (2013).
77. Karlinsey, J. E., Pease, A. J., Winkler, M. E., Bailey, J. L. & Hughes, K. T. The *flk* gene of *Salmonella typhimurium* couples flagellar P-and L-ring assembly to flagellar morphogenesis. *J. Bacteriol.* **179**, 2389–2400 (1997).
78. Yamaguchi, T. *et al.* Structure of the molecular bushing of the bacterial flagellar motor. *Nat. Commun.* **12**, 4469 (2021).
79. Redmon, J., Divvala, S., Girshick, R. & Farhadi, A. You only look once: Unified, real-time object detection. *Proc. IEEE Conf. Comput. Vis. Pattern Recognit*. 779–788 https://doi.org/10.1109/CVPR.2016.91 (2016)..
80. Mastronarde, D. N. Automated electron microscope tomography using robust prediction of specimen movements. *J. Struct. Biol.* **152**, 36–51 (2005).
81. Rubinstein, J. L. & Brubaker, M. A. Alignment of cryo-EM movies of individual particles by optimization of image translations. *J. Struct. Biol.* **192**, 188–195 (2015).

82. Punjani, A., Rubinstein, J. L., Fleet, D. J. & Brubaker, M. A. cryoSPARC: algorithms for rapid unsupervised cryo-EM structure determination. *Nat. Methods 2017 143* **14**, 290–296 (2017).
83. Jones, D. T. Protein secondary structure prediction based on position-specific scoring matrices. *J. Mol. Biol.* **292**, 195–202 (1999).
84. Baker, N. A., Sept, D., Joseph, S., Holst, M. J. & McCammon, J. A. Electrostatics of nanosystems: Application to microtubules and the ribosome. *PNAS.* **98**, 10037–10041 (2001).
85. Dolinsky, T. J., Nielsen, J. E., McCammon, J. A. & Baker, N. A. PDB2PQR: an automated pipeline for the setup of Poisson-Boltzmann electrostatics calculations. *Nucleic Acids Res.* **32**, W665-667 (2004).
86. Johnson, S. *et al.* Molecular structure of the intact bacterial flagellar basal body. *Nat. Microbiol.* **6**, 712–721 (2021).
87. Diepold, A. & Armitage, J. P. Type III secretion systems: The bacterial flagellum and the injectisome. *Philos Trans R Soc L. B Biol Sci* **370**, 20150020 (2015).
88. Hu, J. *et al.* Cryo-EM analysis of the T3S injectisome reveals the structure of the needle and open secretin. *Nat. Commun.* **9**, 3840 (2018).
89. Yan, Z., Yin, M., Xu, D., Zhu, Y. & Li, X. Structural insights into the secretin translocation channel in the type II secretion system. *Nat. Struct. Mol. Biol.* **24**, 177–183 (2017).
90. Weaver, S. J. *et al.* CryoEM structure of the type IVa pilus secretin required for natural competence in *Vibrio cholerae*. *Nat. Commun.* **11**, 5080 (2020).
91. Kojima, S. *et al.* Insights into the stator assembly of the Vibrio flagellar motor from the crystal structure of MotY. *PNAS.* **105**, 7696–7701 (2008).
92. Kawabata, T. MATRAS: A program for protein 3D structure comparison. *Nucleic Acids Res.* **31**, 3367–3369 (2003).
93. Minamino, T. & Macnab, R. M. Components of the *Salmonella* flagellar export apparatus and classification of export substrates. *J. Bacteriol.* **181**, 1388–1394 (1999).
94. Sowa, Y. *et al.* Direct observation of steps in rotation of the bacterial flagellar motor. *Nature* **437**, 916–919 (2005).
95. Nakamura, S., Kami-ike, N., Yokota, J.-I. P., Minamino, T. & Namba, K. Evidence for symmetry in the elementary process of bidirectional torque generation by the bacterial flagellar motor. *PNAS.* **107**, 17616–17620 (2010).
96. Thomas, D. R., Morgan, D. G. & DeRosier, D. J. Rotational symmetry of the C ring and a mechanism for the flagellar rotary motor. *PNAS.* **96**, 10134–10139 (1999).
97. Suzuki, H., Yonekura, K. & Namba, K. Structure of the rotor of the bacterial flagellar motor revealed by electron cryomicroscopy and single-particle image analysis. *J. Mol. Biol.* **337**, 105–113 (2004).

98. Johnson, S. *et al.* Symmetry mismatch in the MS-ring of the bacterial flagellar rotor explains the structural coordination of secretion and rotation. *Nat. Microbiol.* **5**, 966–975 (2020).
99. Kawamoto, A. *et al.* Native flagellar MS ring is formed by 34 subunits with 23-fold and 11-fold subsymmetries. *Nat. Commun.* **12**, 4223 (2021).
100. Suzuki, T., Iino, T., Horiguchi, T. & Yamaguchi, S. Incomplete flagellar structures in nonflagellate mutants of *Salmonella typhimurium*. *J. Bacteriol.* **133**, 904–915 (1978).

Publications and Prizes

Original Papers

Tomoko Yamaguchi, Shoko Toma, Naoya Terahara, Tomoko Miyata, Masamichi Ashihara, Tohru Minamino, Keiichi Namba, Takayuki Kato, Structural and functional comparison of *Salmonella* flagellar filaments composed of FljB and FliC, *Biomolecules*, **10,** 246, 2020

Tomoko Yamaguchi, Fumiaki Makino, Tomoko Miyata, Tohru Minamino, Takayuki Kato, Keiichi Namba, Structure of the molecular bushing of the bacterial flagellar motor, *Nature Communications*, **12**, 4469, 2021

Conferences

○山口智子, 當間頌子, 寺原直矢, 宮田知子, 南野徹, 難波啓一, 加藤貴之, S.Typhimurium べん毛たんぱく質 FljB のクライオ電子顕微鏡構造解析, 生物物理若手の会, 2018, Aug, 2,

○山口智子, 當間頌子, 寺原直矢, 宮田知子, 南野徹, 難波啓一, 加藤貴之, Structural comparison between *Salmonella* flagellar filaments consisting of FliC and FljB and the implication for their function, The 56th Annual Meeting of the Biophysics Society in Japan, 2018, Sep, 15

○山口智子, 當間頌子, 寺原直矢, 宮田知子, 南野徹, 難波啓一, 加藤貴之, *Salmonella* typhimurium べん毛タンパク質 FljB の構造とその特徴, 生体運動会議, 2019, Jan, 5

○山口智子, 當間頌子, 寺原直矢, 宮田知子, 南野徹, 難波啓一, 加藤貴之, The bearing of bacteria flagellar motor analyzed by cryoEM, FBS Retreat 2019, 2019, May, 24

○Tomoko Yamaguchi, Fumiaki Makino, Tomoko Miyata, Takayuki Kato, Keiichi Namba, CryoEM structural analysis of the bacterial flagellar LP ring ~a molecular bushing of the bacterial motor with almost no friction ~, The 57th Annual Meeting of the Biophysics Society in Japan, 2019, Sep, 24–26

〇Tomoko Yamaguchi, Fumiaki Makino, Tomoko Miyata, Takayuki Kato, Keiichi Namba, The bushing of bacterial flagellar motor analyzed by electron cryomicroscopy, RIKEN summer school 2019, 2019, Oct, 7–8

〇Tomoko Yamaguchi, Fumiaki Makino, Tomoko Miyata, Takayuki Kato, Keiichi Namba, べん毛モーター～摩擦を最小限にする軸受けの仕組み～, 生物物理若手の会, 2019, Aug, 26–29

〇Tomoko Yamaguchi, Fumiaki Makino, Tomoko Miyata, Takayuki Kato, Keiichi Namba, CryoEM structural analysis of the bacterial flagellar LP ring ~ a molecular bushing of the bacterial motor ~, 細胞を創る研究会 12.0, 2019, Oct, 17–18

〇Tomoko Yamaguchi, Fumiaki Makino, Tomoko Miyata, Takayuki Kato, Keiichi Namba, クライオ電子顕微鏡で解く！べん毛モーター軸受の構造と機能, 博士人材 CAREER FAIR, 2019, Nov, 7

〇Tomoko Yamaguchi, Fumiaki Makino, Tomoko Miyata, Takayuki Kato, Keiichi Namba, クライオ電子顕微鏡でべん毛モーターのエネルギー変換効率の高い軸受構造に迫る, 企業等と女子大学院生との交流会, 2019, Nov, 13

〇Tomoko Yamaguchi, Fumiaki Makino, Tomoko Miyata, Takayuki Kato, Keiichi Namba, The bushing of bacterial flagellar motor analyzed by electron cryomicroscopy, 理研大交流会, 2019, Dec, 5–6

〇Tomoko Yamaguchi, Fumiaki Makino, Tomoko Miyata, Takayuki Kato, Keiichi Namba, Structure of the bushing of the bacterial flagellar motor analyzed by cryoEM, International Symposium on Structure and Folding of Disease Related Proteins, 2020, Jan, 31

〇山口智子, 當間頌子, 寺原直矢, 宮田知子, 南野徹, 難波啓一, 加藤貴之, 二刀流のべん毛繊維で生き抜くサルモネラの謎に迫る, 第三回非線形化学オンライン研究会, 2020, Sep, 4

〇Tomoko Yamaguchi, Fumiaki Makino, Tomoko Miyata, Tohru Minamino, Takayuki Kato, Keiichi Namba, 構造から紐解くバクテリアべん毛モーターの軸-軸受相互作用, 第 67 回日本生化学会近畿支部例会, 2021, May, 29

〇Tomoko Yamaguchi, Fumiaki Makino, Tomoko Miyata, Tohru Minamino, Takayuki Kato, Keiichi Namba, 細菌の生体分子モーターは静電相互作用で滑らかに回る, 第 61 回生物物理若手の会夏の学校, 2021, Sep, 9

〇Tomoko Yamaguchi, Fumiaki Makino, Tomoko Miyata, Tohru Minamino, Takayuki Kato, Keiichi Namba, The efficient rotation of the flagellar motor by using the electrostatic force, 第 44 回日本分子生物学会年会, 2021, Dec, 1

〇Tomoko Yamaguchi, Fumiaki Makino, Tomoko Miyata, Tohru Minamino, Takayuki Kato, Keiichi Namba, Structural and functional analysis of the molecular bushing of the bacterial flagellar motor and the interactions with the rod, The 59th Annual Meeting of the Biophysics Society in Japan, 2021, Nov, 25–27

Prizes

1. 10th Anniversary Best Cover Awards , Biomolecules (2020) 2 月号 (表紙採用)
2. 2nd prize winner of questioner Award, FBS Retreat 2019, May 24, 2019
3. 生物部門賞/ベストポスターデザイン賞, RIKEN Summer School 2019, Oct 7–8, 2019
4. 優秀発表賞 第 67 回日本生化学会近畿支部例会, May 29, 2021
5. 学生発表賞 第 59 回生物物理学会, Nov, 27, 2021
6. 東洋紡長期海外留学助成金採用, December, 23, 2021